technische universität
dortmund

MAX-PLANCK-GESELLSCHAFT

Dissertation

Structural Investigation of Tc Toxin Activation

Vorgelegt von

Raphael Bader

Zur Erlangung des akademischen Grades des
Doktors der Naturwissenschaft (Dr. rer. nat.)

Vorgelegt der Fakultät
Chemie und Chemische Biologie
der Technischen Universität Dortmund

Angefertigt am
Max-Planck-Institut für Molekulare Physiologie
Dortmund
Abteilung für Strukturbiochemie

Dortmund, 16.07.2025

First Referee: Prof. Dr. Stefan Raunser

Department of Structural Biochemistry
Max-Planck Institute for Molecular Physiology, Dortmund
Faculty of Chemistry and Chemical Biology, Technical University Dortmund

Second Referee: Prof. Dr. Daniel Summerer

Faculty of Chemistry and Chemical Biology, Technical University Dortmund

Contents

1 Abbreviations

° C	Degree Celsius
CAPS	3-(Cyclohexylamino)-1-propanesulfonic acid
HEPES	4-(2-hydroxyethyl)-1-piperazineethanesulfonic acid
TcdA1	A1 pentamer from *Photorhabdus luminescens*
pKa	Acid dissociation constant
ADP	Adenosine di-phosphate
Aa	Amino acid
Å	Angstrom
YwqJ	*Bacillus subtilis* strain
EmBacY	Baculovirus strain
BacMam	Baculovirus transduction of mammalian cells
BLAST	Basic Local Alignment Search Tool
BLI	Bio-layer interferometry
BFP	Blue fluorescent protein
$CaCl_2$	Calcium chloride
C-terminus	Carboxy terminal end
Cdc42	Cell division control protein 42 homolog
CDC	Cholesterol-dependent cytolysins
CPE	Clostridium perfringens enterotoxin
CRISPR	Clustered Regularly Interspaced Short Palindromic Repeats
CTF	Contrast transfer function
CLEM	Correlative light and electron microscopy
cryo-EM	Cryo-electron microscopy
cryo-ET	Cryo-electron tomography
Cry toxins	Crystal toxins
cAMP	Cyclic adenosine monophosphate
Cys	Cysteine
ClyA	Cytolysin A
CNF1	Cytotoxic Necrotizing Factor 1
Da, kDa, MDa	Dalton, kilodalton, mega Dalton
DNA	Deoxyribonucleic acid
EF	Edema factor
EM	Electron microscopy
EMDB	Electron microscopy data bank
EDTA	Ethylenediaminetetraacetic acid
F-actin	Filamentous actin
FIB	Focused ion beam
FSC	Fourier shell correlation
G-actin	Globular (monomeric) actin
GTPases	Guanosine triphosphate phosphatases

HRTEM	High-resolution transmission electron microscopy
His	Histidine
h, min, s	Hour, minute, second
HCD	Human cytidine deaminase
HEK	Human embryonic kidney
HVR	Hyper-variable region
LF	Lethal factor
LM	Light microscopy
LED	Light-emitting diode,
LB	Luria-Broth
LAMP1	Lysosome-associated membrane glycoprotein 1
Mcf	Makes caterpillar floppy
MAC	Membrane attack complex
MACPF	Membrane Attack Complex/Perforin
µl, ml, l	Microliter, milliliter, liter
MAP	Mitogen-activated protein
MD simulations	Molecular dynamics simulations
MW	Molecular weight
MSA	Multiple Sequence Alignment
NHS	*N*-Hydroxysuccinimide
Nm	Nanometer
NLRP3	NLR family pyrin domain containing 3
mKOet	Orange fluorescent protein
PMSF	Phenylmethylsulfonyl fluoride
PBS	Phosphate Buffered Saline
PALM	Photoactivated Localization Microscopy
Pir	Photorhabdus insect-related
PTC3	*Photorhabdus luminescens* holotoxin with C3 effector
PVC	Photorhabdus virulence cassette
PIP	Plant-incorporated protectant
Tween-20	Polysorbate 20
PFT	Pore-forming toxins
PD-L1	Programmed cell death 1 ligand 1
PA	Protective antigen
PDB	Protein data bank
RhoA	Ras homolog family member A
Rab5a	Ras-related protein Rab-5A
Rab7a	Ras-related protein Rab-7A
RHS	Rearrangement hotspot
RBD	Receptor binding domain
mCherry	Red fluorescent protein
ROI	Region of interest

RNA	Ribonucleic acid
RAV	Ribosome-associated vesicles
SEM	Scanning electron cryomicroscopy
SPA	Single particle analysis
SEC	Size-exclusion chromatography
SDS-PAGE	Sodium dodecyl sulfate–polyacrylamide gel electrophoresis
*Sf*9	*Spodoptera frugiperda* insect cell line
STED	Stimulated Emission Depletion microscopy
STORM	Stochastic Optical Reconstruction Microscopy
STA	Sub-tomogram averaging
QT	TcdA1 mutant using QandT in the tip region
TAC	Thesis advisory committee
3D	Three dimensional
Tc toxin	Toxin complex toxin
TEM	Transmission electron microscopy
TRIS	Tris(hydroxymethyl)aminomethane
2D	Two dimensional
T10SS	Type 10 secretion system
VSG	Variant surface glycoprotein
WT	Wild type
YaxAB	*Y. enterocolitica AB toxin*
YenTc	*Yersinia entomophaga* Tc toxin

2 Abstract

TC toxins are a potent class of toxins found in pathogenic bacteria. Their enormous complex size (up to 2 MDa) not only enables them to shield their toxic effector properly but also makes them one of the largest known bacterial translocation machineries to integrate into host membranes. Their versatility in adapting to external influences has sparked considerable interest in utilizing them for translational research, such as biopesticides or as biological syringes. While much is known about related groups of toxins in general and the structure of Tc toxins specifically, the molecular mechanisms underlying the interaction of Tc toxins with host cells, critical for adapting the system to various applications, remain nebulous.

In this thesis, I employed a hybrid structural biology approach, combining cryo-electron microscopy (cryo-EM), light microscopy, and cryo-electron tomography (cryo-ET), to investigate the underlying molecular mechanism of Tc toxin interaction with host cells.

First, in collaboration with a molecular dynamics (MD) simulations group and utilizing our high-resolution structures of Photorhabdus luminescens Tc toxin mutants, I identified a conserved mechanism for pore formation at alkaline pH. The mechanism involves a tightly controlled molecular latch system that reacts to changes in electric potential. This equilibrium is generated by the interplay of repulsive and attractive forces, which determines the likelihood of pore formation. It can be influenced by changes in pH, conformational changes in the outer shell, or internal destabilization induced by the HVR relocating inside the toxin.

Next, I analysed a Tc toxin from *Yersinia entomophaga* (YenTc) using high-resolution cryo-EM and mass spectrometry. This investigation revealed novel conformational states that are potentially present in all split-A Tc toxins. These changes include flipping the outer shell upside down and/or eliminating it in response to environmental influences, thereby enabling a highly versatile system.

Ultimately, I developed a fluorescent reporter system that enables the visualization of endosomal maturation states in a single cell. I employed this system to correlate the measured fluorescence with the spatial information obtained in the SEM and subsequently TEM to analyse Tc toxin entry into host cells. This provides the basis for future work to correctly correlate the Tc toxins inside cells and analyse them in detail.

3 Zusammenfassung

Tc-Toxine sind eine besonders effiziente Klasse von Toxinen, die in pathogenen Bakterien vorkommen. Ihre enorme Größe (bis zu 2 MDa) ermöglicht es ihnen nicht nur ihren toxischen Effektor bestmöglich zu beschützen, sondern macht sie zu einer der größten bekannten bakteriellen Translokationsmaschinen, die sich in Wirtsmembranen integrieren können. Hieraus resultiert eine Vielfalt an Möglichkeiten auf äußere Einflüsse flexibel zu reagieren, was Tc-Toxine attraktiv für die translationale Forschung macht, z. B. als Biopestizide oder als biologische Spritzen. Während über verwandte Toxine und die Struktur von Tc-Toxinen viel bekannt ist, verbleiben die molekularen Mechanismen, welche der Interaktion von Tc-Toxinen mit Wirtszellen zugrunde liegen und essentiell für die Adaptierung des Systems für alternative Anwendungen sind, eher im Dunkeln.

In dieser Arbeit habe ich einen hybriden strukturbiologischen Ansatz verwendet, der Kryo-Elektronenmikroskopie (Kryo-EM), Lichtmikroskopie und Kryo-Elektronentomographie (Kryo-ET) kombiniert, um dem molekularen Mechanismus der Interaktion von Tc-Toxinen mit Wirtszellen auf den Grund zu gehen.

Zunächst konnte ich in Zusammenarbeit mit einer Arbeitsgruppe, die auf MD-Simulationen spezialisiert ist, und mittels hochauflösender Strukturen der Tc-Toxin-Mutanten von *Photorhabdus luminescens* einen konservierten Mechanismus für die Porenbildung bei alkalischem pH-Wert beschreiben. Dieser Mechanismus beinhaltet ein eng kontrolliertes molekulares Aktivierungssystem, das auf Änderungen des elektrischen Potenzials reagiert. Dieses Gleichgewicht, das durch das Zusammenspiel von abstoßenden und anziehenden Kräften erzeugt wird, bestimmt die Wahrscheinlichkeit der Porenbildung. Beeinflussen können dieses Equilibrium pH-Änderungen, Konformationsänderungen in der äußeren Hülle oder eine interne Destabilisierung, die durch die Verlagerung des HVR innerhalb des Toxins hervorgerufen wird.

Weiterhin habe ich ein hochspezifisches Tc-Toxin aus *Yersinia entomophaga* (YenTc) mithilfe von hochauflösenden Rekonstruktionen und Massenspektrometrie-Analysen untersucht. Diese Betrachtung ergab neue Konformationszustände, die möglicherweise in allen Split-A-Tc-Toxinen vorhanden sind. Zu diesen Veränderungen gehört, dass die äußere Hülle als Reaktion auf Umwelteinflüsse ihre Orientierung um 180 Grad ändert und/oder vollständig eliminiert wird, was ein äußerst vielseitiges System ermöglicht.

Schließlich habe ich ein fluoreszierendes Reportersystem entwickelt, mit dem die Reifungszustände von Endosomen in einer einzelnen Zelle ersichtlich werden, was eine direkte Korrelation zwischen der Tc-Toxin-Infektion und den entsprechenden Endosomen ermöglichte. Zusammen

bilden die strukturellen und mechanistischen Einblicke über die Wirkung des Tc-Toxins die Grundlage für eine *in vivo*-ähnliche Untersuchung ihres Infektionszyklus mithilfe der Kryo-ET und ebnen den Weg für die Entwicklung besserer biologischer Pestizide und Translokations-werkzeuge.

4 Introduction

„*Si vis pacem, para bellum* "-- 'If you want peace, prepare for war'. Not only has this famous proverb inspired countless politicians and leaders throughout history, but even prokaryotes appear to have followed its wisdom. The microscopic world is shaped by an evolutionary arms race, with bacteria developing a plethora of highly versatile and adjustable mechanisms to combat one another, as well as other species or organisms [1]. A good number of these tools, many of which are biological toxins and effectors, are highly conserved across numerous bacterial species and are commonly produced and deployed redundantly. Although many bacterial classes can be pretty destructive, several bacteria not only carry an impressive arsenal but can also support a symbiotic relationship if it is to their advantage.

4.1 Life cycle of Photorhabdus luminescens

One genus of bacteria that has sparked scientific interest due to its broad pathogenicity is Photorhabdus, which encompasses insect, as well as potential human-pathogenic species, and includes, for example, P. luminescens, P. asymbiotica, and *P. temperata* [2, 3]. *P. luminescens* was the first to be characterized [4]. It circulates through a complex dual life cycle that alternates between a mutualistic symbiosis with entomopathogenic nematodes of the family *Heterorhabditidae* and a pathogenic phase where insect hosts are targeted [5, 6].

The cycle begins with *P. luminescens* residing in the pharynx of *Heterorhabditis* nematodes [7]. These so-called Dauer or infective juveniles, referring to a stasis-like and non-feeding stage of the nematodes, actively seek out insect larvae in the soil. Once a suitable insect host is found, the nematodes enter the insect either through front and rear openings or by breaching the cuticle. After reaching the inside of the insect's haemolymph, the nematodes regurgitate *P. luminescens* bacteria from their gut. This environmental change, experienced by the bacteria, triggers the pathogenic phase, in which P. luminescens multiplies rapidly and releases a series of toxins, as well as secondary metabolites, that suppress the insect's immune system and kill the host, typically within 48 hours [8, 9]. The bacteria then secrete extracellular enzymes that break down the insect tissue, transforming the carcass into a nutrient-rich environment that supports the development of both bacteria and nematodes. During this phase, *P. luminescens* also produces antibiotics and other compounds to prevent colonisation by competing microbes [10]. The nematodes hatch eggs within themselves, a process termed endotokia matricida, and create several generations within the insect carcass [11]. As nutrients are depleted, new infective juveniles are

formed, which recolonize the gut of *P. luminescens*. These new generations then leave the depleted carcass and disperse into the soil to find new insect hosts, restarting the cycle (Figure 1).

P. luminescens also exhibits phenotypic heterogeneity, existing in two main forms: the primary form, which is capable of supporting nematode development, and a secondary form that is dormant and unlikely to undergo symbiosis with nematodes [12]. This phenotypic switch is thought to be a survival strategy in response to environmental stress and nutrient limitation [13].

Among the different classes of toxins produced by *P. luminescens* are Toxin complexes (Tc toxins) [14, 15], Mcf (Makes Caterpillars Floppy) toxins [9, 16], Pir (Photorhabdus insect related proteins) toxins [14], PVC (Photorhabdus Virulence Cassettes) toxins [17], as well as Xenorhabdolysins [18, 19], all of which allow for a cascade of potentially lethal reactions that render escape of the insect almost impossible [20].

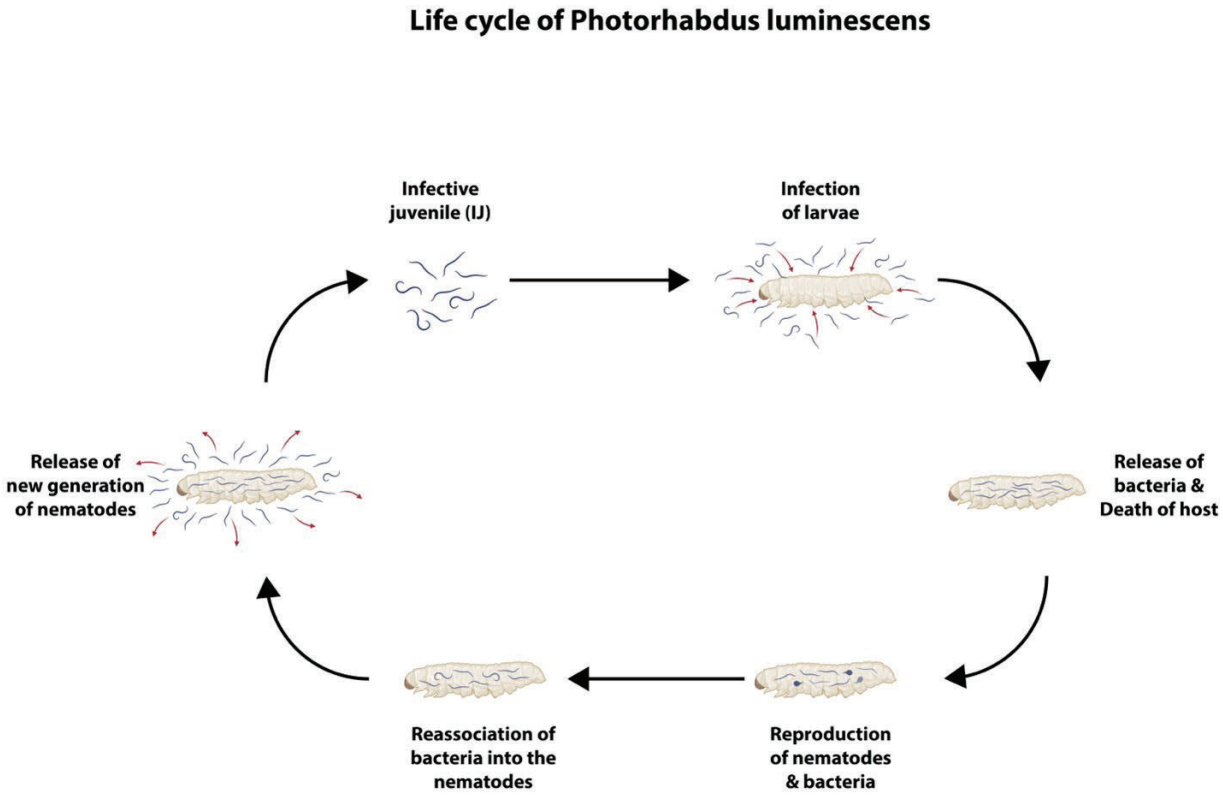

Figure 1: Overview of the life cycle of Photorhabdus luminescens
Schematic representation of *Photorhabdus luminescens* life cycle. Initially, the infective juveniles infect insect larvae through accessible entry locations. Upon entry into the insect, the symbiotic bacteria are released into the host organism, and they subsequently release toxins and effectors to kill the host organism. Using the insect cadaver as a food source allows the bacteria and nematodes to reproduce. After the cadaver is consumed, the bacteria reassociate with the nematodes that leave the dead insect to initiate a new infection cycle. Created with BioRender.com.

4.2 Life cycle of Yersinia entomophaga

In contrast to *Photorhabdus luminescens*, *Yersinia entomophaga* is an insect-pathogenic bacterium whose life cycle is independent of symbiosis with other organisms, potentially also altering the characteristics of their toxins [21]. The life cycle of *Y. entomophaga* can be summarized as follows:

After entering the insect host, typically by ingestion, *Y. entomophaga* colonizes the gut. Infected larvae often show rapid symptoms, including reduced feeding, expulsion of gut contents, and colour changes, with death usually occurring within 2 to 5 days of infection [22]. *Y. entomophaga*'s toxicity is controlled via the type 10 secretion system, where, reacting to external factors, a subpopulation of the bacterial cells termed 'soldier cells' overproduce a toxin cocktail until explosion, to allow the surviving bacteria to benefit from this cycle [23-25].

Following the death of the insect host, *Y. entomophaga* can continue to multiply within the carcass, taking advantage of the nutrient-rich environment (Figure 2). The ability of these bacteria, as well as closely related ones, to kill a wide range of insect pests is primarily attributed to the activity of one or more of their toxins, such as the YenTc toxin, highlighting the importance of bacterial effectors [26, 27].

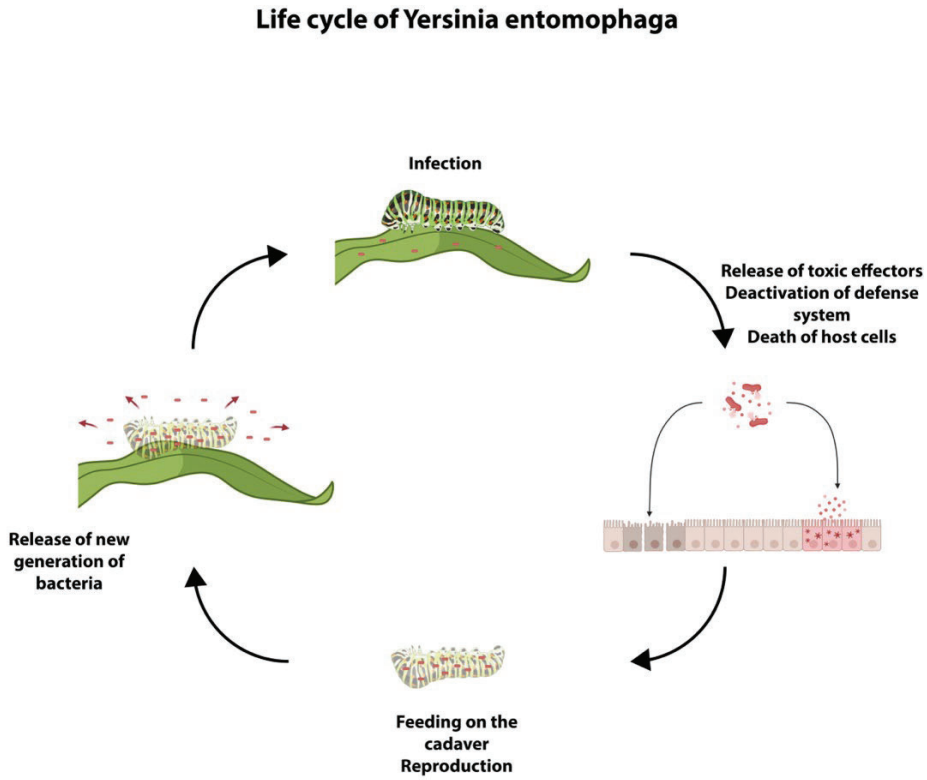

Figure 2: Overview of the life cycle of Yersinia entomophaga
Cartoon representation of *Yersinia entomophaga* life cycle. Upon uptake of the bacteria, mainly orally, the bacteria enter the insect midgut, triggering the 'soldier cells' to mass produce toxins until they burst. Hereafter, the released toxins bypass or deactivate the host organism's potential defense mechanisms, allowing them to begin killing it. Utilizing the cadaver as a food source, the remaining bacteria reproduce until the organism is depleted, and a new infection cycle is then initiated. Created with BioRender.com.

4.3 Pore-forming toxins (PFTs)

Pore-forming toxins (PFTs) are a diverse group of proteins widely distributed among both Gram-negative and Gram-positive bacteria [28]. These toxins play crucial roles in bacterial pathogenesis and inter-microbial competition, acting as virulence factors that facilitate bacterial dissemination and host colonization [29]. Many PFTs are synthesized as solvent-exposed monomers that undergo a remarkable transformation from their soluble state to become membrane-embedded structures through significant conformational changes [30, 31] (Figure 3).

These proteins follow, with some exceptions, two structural trends: α-PFTs and β-PFTs, which differ in their secondary structural elements [28]. α-PFTs, such as the *Escherichia coli* cytolysin A (ClyA), rely on α-helical bundles for membrane insertion [32]. ClyA monomers adopt a compact, stable fold in solution, but undergo conformational changes upon encountering membranes [33]. This exposes hydrophobic regions and drives oligomerisation into a 13-subunit ring with a central α-helical pore [34]. Another entirely α-helical pore-forming toxin class is Xenorhabdolyins (Xax), first described in the entomopathogenic bacterium *Xenorhabdus nematophila* [35]. These toxins play a critical role in the bacterium's ability to attack host cells by perforating their membranes [36, 37]. Structurally, Xax toxins are classified as α-pore-forming toxins (α-PFTs), forming large multimeric pore complexes—typically composed of 12 to 15 subunits—that insert into target cell membranes and create channels with molecular masses ranging from 1 to 1.3 MDa [18]. The Xax toxin consists of two proteins, XaxA and XaxB. XaxA functions as an activator and stabilizer, while XaxB undergoes significant conformational changes, including the exposure of an amphipathic helix, to drive membrane insertion and actual pore formation [36].

In contrast, β-PFTs construct transmembrane channels using β-strands. A prominent subclass, the cholesterol-dependent cytolysins (CDCs), such as *Streptococcus pneumoniae* pneumolysin, bind cholesterol via a conserved undecapeptide (11-residue) motif (ECTGLAWEWWR) in their domain 4 [38]. This interaction triggers oligomerisation into prepores, which subsequently collapse vertically to form 260-300 Å β-barrel pores composed of 30-44 subunits [39]. Smaller β-PFTs, such as *Staphylococcus aureus* α-hemolysin, assemble heptameric prepores on lipid bilayers before extruding a 14-stranded β-barrel stabilised by hydrogen bonds [40].

The mechanism of action for PFTs after secretion involves several key steps: Initially, already assembled toxin complexes or toxin protomers bind to specific receptors on the target cell membrane, which can be lipids, glycans, and/or proteins [28, 41]. This binding serves two potential

purposes besides targeting: (1) it increases the local concentration of the toxin, and (2), in the case of protomers, it promotes oligomerization [41]. Once bound, either the toxin monomers assemble into polymeric structures that form transmembrane pores, or the assembled toxins rearrange due to external influences to perforate the membrane. Perforation of the cell membrane either leads to uncontrolled efflux of ions and nutrients or allows translocation of associated effectors, ultimately causing the death of the attacked cell (Figure 3) [31]. However, even non-lytic variants can cause cell death by activation of the NLRP3 inflammasome assembly [42].

As mentioned earlier, PFTs insert themselves into the cell membrane, leading to the uncontrolled flux of ions and molecules, dissipation of cellular gradients, and ultimately, cell death [28]. However, pore-forming toxins further evolved to translocate effectors and improve killing efficiency. Therefore, in a more developed definition of pore-forming toxins, more sophisticated toxin complexes also belong to the ever-growing family. One particularly well-known group of these PFTs is the anthrax toxin, which follows the previously mentioned mode of action: The anthrax toxin is a binary A-B toxin composed of protective antigen (PA), edema factor (EF), and lethal factor (LF) [43-45]. PA functions as the binding (B) component, forming heptameric pores following receptor-mediated endocytosis[44]. EF (an adenylate cyclase) and LF (a Zn^{2+}-protease) are enzymatic (A) components that disrupt host cell signalling [46-48]. The EF-induced increase of cAMP levels has been demonstrated to result in the accumulation of fluid, a phenomenon referred to as edema [48-50]. In contrast, LF has been shown to induce the cleavage of MAP kinase kinases, leading to cell death. PA undergoes a series of structural transitions, beginning as a monomer and culminating in the formation of a prepore [44, 51, 52]. This process is followed by the final step of a membrane-spanning pore, which facilitates the translocation of EF/LF into the cytosol under acidic endosomal conditions [51-54].

Many of these intoxication pathways are, however, strictly regulated by receptor binding to guarantee cellular specificity and toxicity. *Bacillus thuringiensis* Cry toxins, another example of prominent PFTs, target insect midgut cadherins, inducing toxin oligomerisation and pore formation in a receptor-dependent manner [55-57]. Similarly, *Clostridium perfringens* enterotoxin (CPE) binds to claudins, tight junction proteins, in intestinal epithelial cells, forming a complex with claudin-3 or -4 that recruits non-claudin proteins to create a larger prepore [58, 59]. *Yersinia enterocolitica* YaxAB forms asymmetric pores with a trimeric α-helical bundle and also shares similarities with the ClyA toxin family [60].

PFTs are so efficient at killing cells that they have also found their way into the human immune system. Human perforin, produced by cytotoxic T cells, binds target cell membranes via calcium-dependent interactions and polymerizes into the Membrane Attack Complex/Perforin (MACPF) domain pores to release apoptosis-inducing granzymes [61]. The complement membrane attack complex (MAC) assembles C9 subunits into β-barrel pores on the surfaces of pathogens, guided by antibody-antigen recognition [62]. This further highlights PFTs as an example of evolutionary convergence, with analogous mechanisms emerging in bacteria, fungi, plants, and animals [63]. Their structural adaptability and receptor specificity make them valuable tools for biotechnology, such as aerolysin-based nanopore sequencing or engineered immunotoxins targeting cancer cells [64]. Therapeutic strategies aim to neutralize toxins by blocking receptor interactions (e.g., monoclonal antibodies against PA in anthrax) or inhibiting oligomerization (e.g., small molecules that stabilize CDC monomers) [65-67].

Understanding the interaction of these toxins with host receptors continues to inform vaccine design and antimicrobial therapies, underscoring their dual role as both threats and tools in molecular medicine.

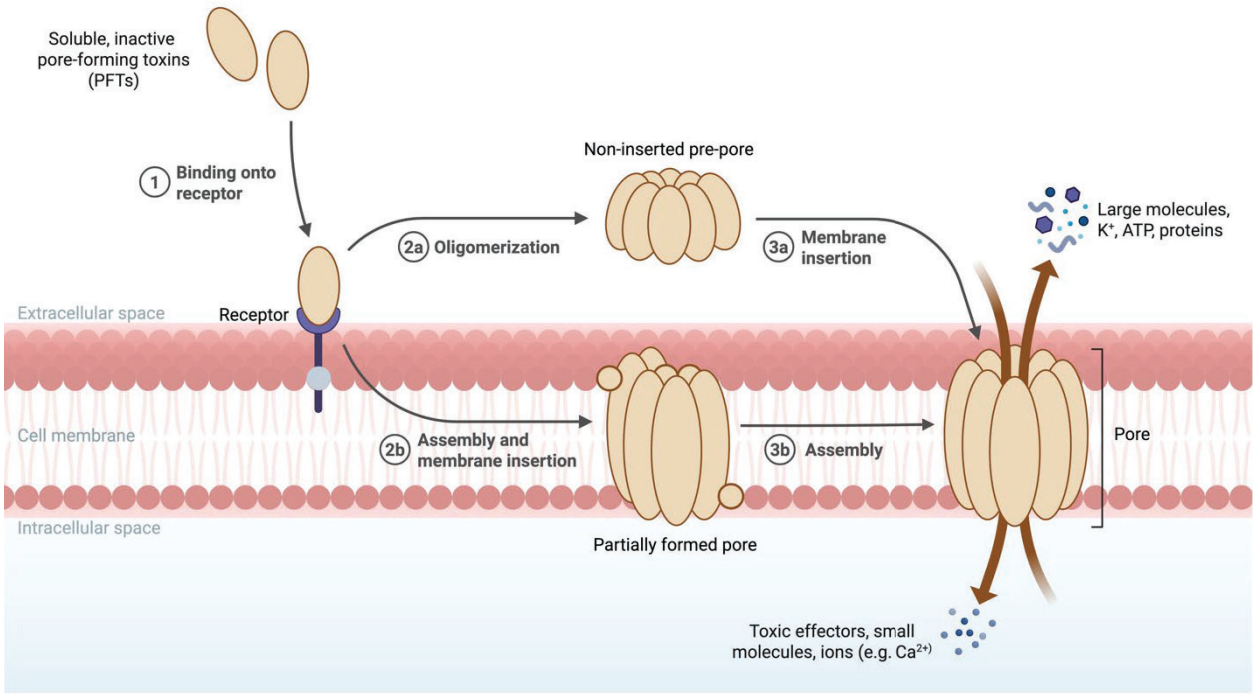

Figure 3: General mechanism of PFTs
Upon receptor recognition on potential host cells (1), the PFT is activated, leading to two possible pathways depending on the type of toxin: (2a) Indirect interaction of the toxin with the membrane via a prepore state that requires additional factors (e.g. Oligomerization) to pierce into the membrane or (2b) direct insertion of the formed pore complex into the membrane. In both cases, the toxic effect is initiated by its insertion (3a and b). Figure adapted from [28] and created with BioRender.com.

4.4 Tc toxins

A prominent example of PFTs is the tri-component toxin complexes (Tc), which are the primary focus of this thesis. They form a group of potent and highly expressed toxins that have sparked scientific interest due to the enormous size and complexity of their translocation machinery [68]. These toxins, initially identified in insect-pathogenic *Photorhabdus* strains, can also be found in human, plant, and aquatic pathogens [8, 69, 70]. A very infamous organism, known to express Tc toxins, is the causative agent of bubonic plague, *Yersinia pestis* [71, 72]. Although Tc toxins are generally released along with other bacterial toxins, it has been shown for *Y. entomophaga* that the toxicity is highly dependent on the presence of functional Tc toxins [73]. Moreover, the concept of complex formation implies a possible exchange of individual components, which is further supported by the presence of multiple copies of each constituent protein of the Tc toxin in *P. luminescens* alone [68].

Tc toxins, in general, comprise three distinct subunits: TcA (Figure 4A and Figure 5A), TcB, and TcC (Figure 6A and Figure 7A) [14, 68, 74]. The TcA subunit assembles into a pentameric, bell-shaped structure, a ~1.4 MDa complex, with a central α-helical translocation channel (Figure 4B) [75]. This domain is structured as a funnel-shaped channel about 100 Å wide at the top, narrowing to about 30 Å at its bottom tip (Figure 4B). It is composed of five α-helical bundles that undergo significant conformational changes during the transition from a closed prepore to an open, membrane-inserted pore state (Figure 4A and Figure 5A). A stretched proline-rich linker domain connects the pore-forming domain to the rest of the toxin (Figure 4C). When the toxin triggers the formation of a pore, the linker collapses into an α-helix (Figure 5C). It has been shown to provide the energy necessary to facilitate the conformational change [76, 77].

Surrounding these central domains is the outer shell, which forms a bell-shaped backbone (Figure 4B) [14, 75]. The α-helical region is further subdivided into large and small lobes, characterized by repeating helix-loop-helix motifs, which provide the structure with rigidity and stability. At the base of the shell, the five protomers form a single neuraminidase-like domain, which shields the interior parts (Figure 4B) [14].

The periphery of the TcA shell contains receptor binding domains (RBDs) (Figure 4B), which vary across TcAs, likely conferring host specificity by binding to specific targets on host cells [75].

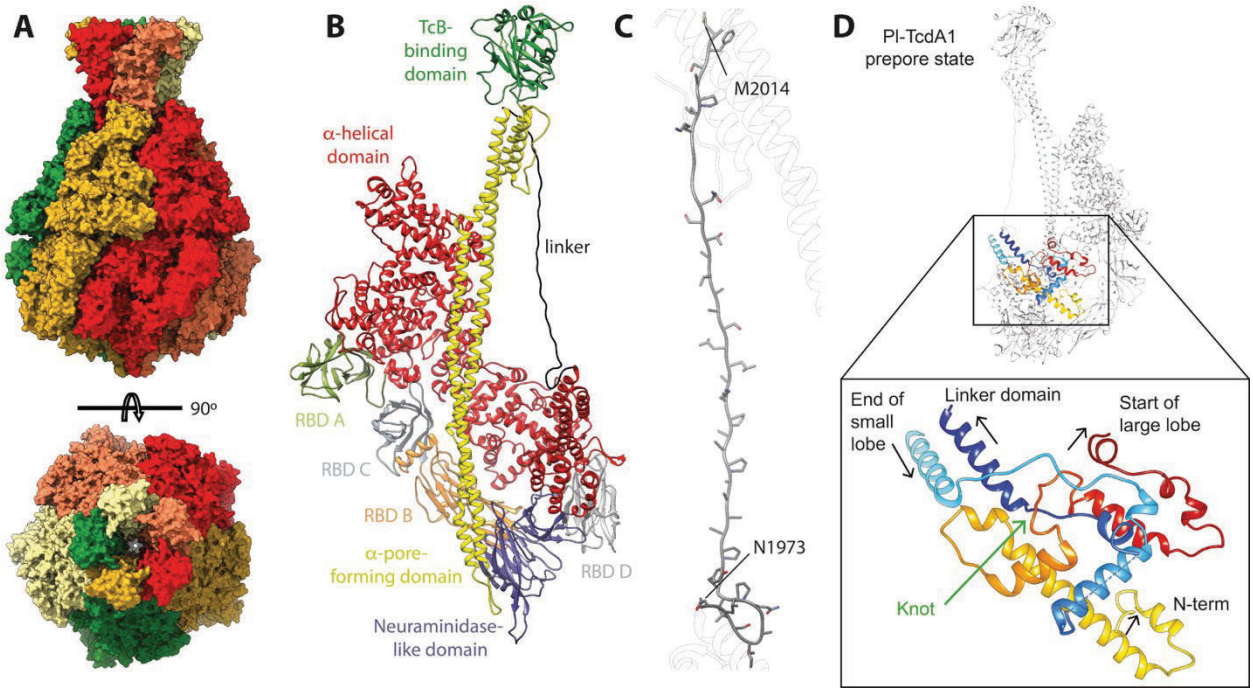

Figure 4: Architecture of pentameric A component (prepore state) and important features
(A) Atomic representation of pentameric TcA (prepore state) in side (top) and top (bottom) view, colored by protomeric chains. The domain architecture of a protomeric A component is shown as cartoon (B) highlighting the individual RBDs (gray, orange, silver and lime), the neuraminidase-like domain (violet), the channel forming domain (yellow), the outer shell (red) and the TcB binding domain (green) as well as in the linker region (black). The stretched linker (C) from start to end represents all side chains. (D) Cartoon representation of TcA in prepore state highlighting the conserved trefoil knot in its closed conformation (color in rainbow colors) directly connecting the N-terminus with the linker region. Figure adapted from [68](A-C) and [75](D).

Interestingly, some homologues, such as *Yersinia pseudotuberculosis* TcaA-TcaB, lack these RBDs altogether and have instead replaced them with a coiled-coil domain that interacts with the TcaB subunits to provide structural stability [74, 75]. Furthermore, for the Tc toxin from *Yersinia entomophaga*, YenTc, the RBDs have been replaced by chitinase domains, likely also providing host specificity and additional enzymatic functions to the toxin [27, 78, 79]. Another characteristic of YenTc is its association with a subgroup of Tc toxins, in which TcA is formed of two separate protein chains, likely due to genetic or structural adaptations. These so-called split-A toxins, however, were shown to preserve the general architecture of TcAs [79].

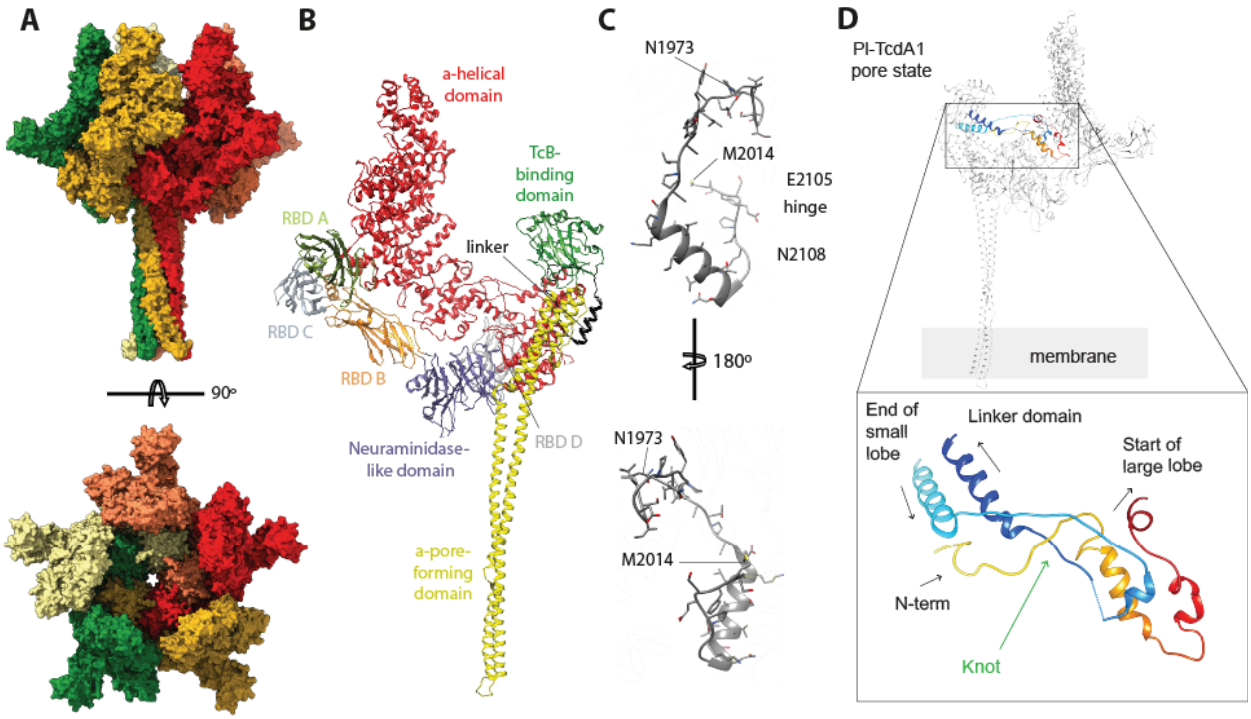

Figure 5: Architecture of pentameric A component (pore state) and important features
(A) Atomic representation of pentameric TcA (pore state) in side (top) and top (bottom) view, colored by protomeric chains. The domain architecture of a protomeric A component is shown as cartoon (B) highlighting the individual RBDs (gray, orange, silver and lime), the neuraminidase-like domain (violet), the channel forming domain (yellow), the outer shell (red) and the TcB binding domain (green) as well as in the linker region (black). The linker (C) in its condensed form, from start to end, represents all side chains. (D) Cartoon representation of TcA in pore state, highlighting the conserved trefoil knot (color in rainbow colors) in its open conformation. Figure adapted from [68](A-C) and [75](D).

Recent studies have shed more light on potential receptor recognition. All tested TcAs tended to interact with heparin sulfates, suggesting that this mediates the initial interaction [80]. For more specific interactions, TcdA1 has been observed to bind quite tightly to Lewis X antigens using its RBD-D in BLI (Biolayer Interferometry) experiments [80]. Moreover, N-glycans were found to be crucial for proper intoxication [81, 82]. Bioinformatic approaches suggest that in ~25 % of all analyses, Tc toxin genes encode versions of RBD-D; however, the others most likely facilitate their recognition via other glycans or molecules [82]. For instance, the human pathogenic *Morganella morganii* TcA retains functional RBDs, whereas the previously mentioned TcA subunit of *Yersinia pseudotuberculosis* lacks the typical RBDs [75]. Despite this lack of typical RBDs, the *Y. pseudotuberculosis* TcA still retains its capacity to act as both a human and an insect pathogen. Moreover, additional studies have also revealed a potential cell surface receptor that assists Tc toxins in recognizing specific host cells. Variant surface glycoprotein (Vsg) or Vsg-like proteins can serve as receptors for Tc toxins in, for example, *Drosophila* S2 cells [83]. Notably, Vsg-like molecules are known for their role in immune evasion by protozoan parasites, such as trypanosomes, underscoring the conserved nature of this mechanism among pathogens.

Besides their intricate substrate recognition architecture, TcAs also have several unique structural elements: One is a trefoil protein knot within the shell, a feature conserved among bacteria and most likely associated with stabilising the existing protein fold (Figure 4D) [75, 84, 85]. Since the knot is found at the base of the linker, it's presumed to stabilise the linker in the prepore state (Figure 5D).

Another known feature of TCAs is the presence of electrostatic interactions at the shell-shell interfaces, which act as latches that stabilize the arrangement; these latches can likely be triggered in response to environmental cues, such as pH changes. As previously described, there is no classic electrostatic switch that initiates pore formation directly in response to pH changes; however, the aforementioned electrostatic latches are hypothesized to be essential steps towards pore formation [75].

Overall, this blend of conserved and variable structural elements allows Tc toxins to maintain a unified mechanism of intoxication while evolving to target diverse hosts. One example of this trend is a possible alternative entry pathway into cells, apart from the endosomal pathway, where Tc toxin pore formation might already occur on the cell surface, triggered by highly alkaline pH ranges (Figure 8) [14, 86].

The majority of studies on these toxins to date have been performed on *Photorhabdus luminescens*, which also includes the structures of its prepore and pore state (Figure 7E and F) [14, 86]. Although Tc toxins vary heavily at the sequence level, the overall fold of the complex is highly conserved across bacterial species, even for split-A toxins [75, 79].

At the top of TcA is a funnel-shaped TcB-binding domain, which is critical for docking the TcB-TcC effector-containing complex (Figure 6A) [14]. This TcB-TcC complex forms a ~250-kDa cocoon that encapsulates a ~30-kDa toxic enzyme (Figure 6A), which is the C-terminal part of TcC, also known as the hypervariable region (HVR) [76]. The structural motif of the cocoon, known as the rearrangement hotspot (RHS) fold, is not unique to bacterial toxins; it also appears in viral toxins and even human neuronal receptors, such as teneurins, highlighting the ingenious design and long evolutionary conservation [87]. The HVR is autoproteolytically cleaved (Figure 6B) and maintained in a partially unfolded state within the cocoon (Figure 7A) [76]. The TcB subunit contains a six-bladed β-propeller domain (Figure 6C) that undergoes significant conformational rearrangements upon binding to TcA (Figure 6D) [88]. This structural change opens the cocoon, allowing the HVR to be released and threaded through the translocation channel formed by TcA (Figure 7H) [68].

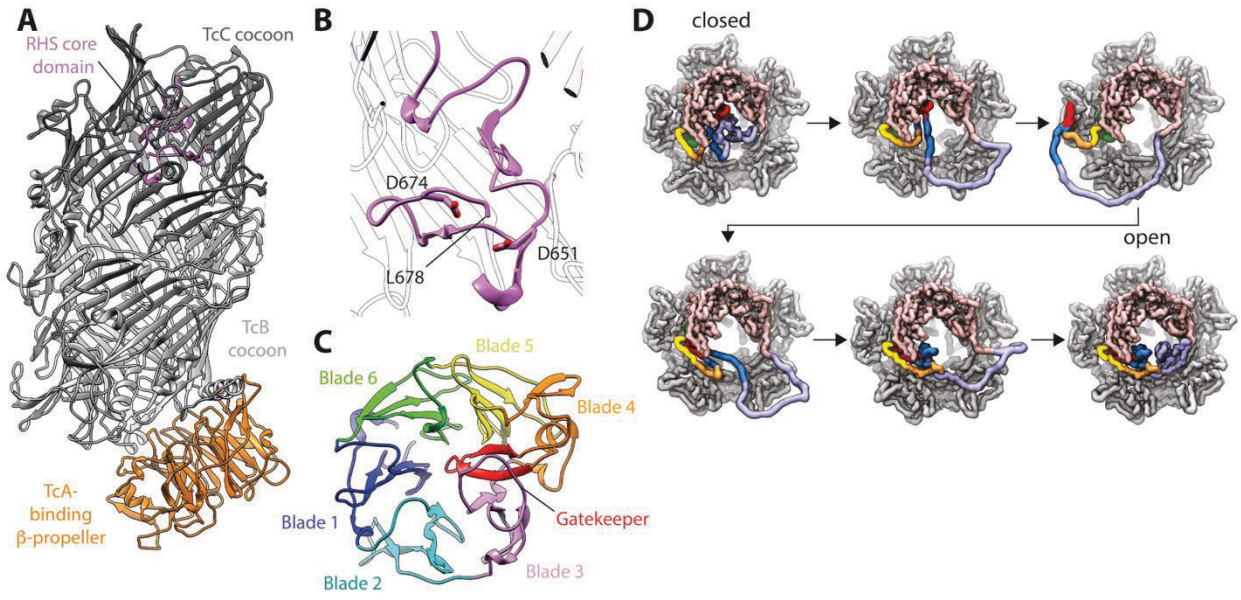

Figure 6: Architecture of BC cocoon and autoproteolytic site
(A) Cartoon representation of the assembled BC cocoon highlighting the RHS core domain (violet) and the ß-propeller interface (orange), which refolds upon interaction with the A component. Cartoon representation of the auto-proteolytic cleavage site (B) with a focus on the active aspartate D651 and the cleaved C component ending at L678. Overview of the six ß-propeller blades (C) forming the bottom with the gatekeeper (red) in its closed, unattached conformation. (D) Simulated rearrangement of the gatekeeper upon binding to TcA, allowing release of the toxic effector. Figure adapted from [68].

Attempts to alter the toxic cargo have demonstrated that usage of this toxin as a drug delivery system is feasible in principle [89]. In general, various cargos with size ranges between ~ 20 - 35 kDa and an isoelectric point (pI) close to 9 were successfully translocated by the modified toxins. This suggests a size limitation imposed by the cocoon and the necessity of an excess of positively charged residues on the effector for the successful adaptation of other cargos. Moreover, targeting Tc toxins to specific cells proved to be challenging.

The mechanism of action of Tc toxins involves several key steps [68]: First, initial interactions are mediated by the receptor-binding domains associated with the A subunit. Secondly, following external influences, such as pH shifts, a structural rearrangement in TcA is facilitated, ultimately leading to the penetration of the membrane through the release of the translocation channel, which is driven by the contraction of the linker [77].

These structural steps involve several intermediate states, beginning with the flipping out of the RBDs [90]. This movement, in turn, disrupts their interaction with the outer shell and leads to a better solvent accessibility of the N-terminus, resulting in a less stable prepore conformation. Next, the shell opens up to a point of no return, at which the stretched linker collapses, inducing pore formation and membrane insertion [77]. Sequentially, the channel opens, allowing the toxic enzyme to be translocated into the host cell cytosol (Figure 7A-I) [76].

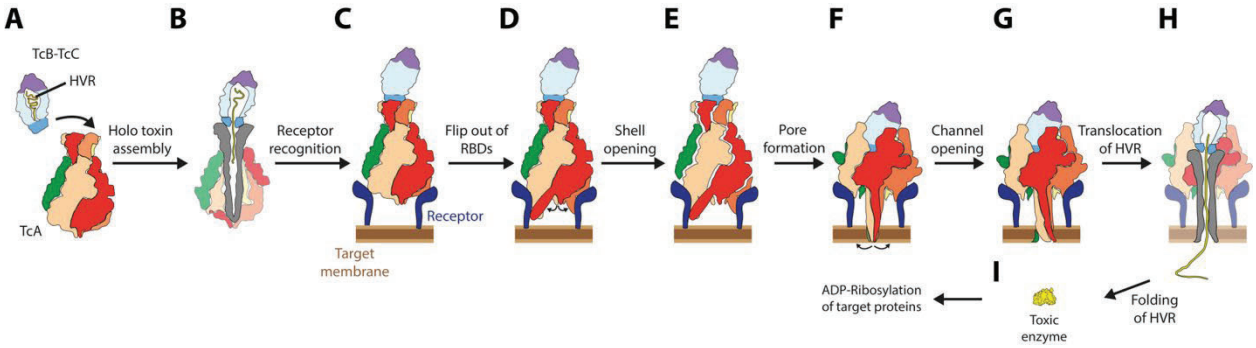

Figure 7: Mechanism of Tc toxins' action
Upon holotoxin formation and auto-proteolytic cleavage of the effector (A and B), the toxin can interact with potential host cells via receptor recognition (C). Upon contact with external factors, such as pH changes, e.g., during endosomal maturation, the RBDs flip outwards and facilitate initial shell opening and prepore destabilization (D and E). Followed by the collapse of the stretched linker, the toxin undergoes a conformational change to its pore state (F and G). Thus, allowing the effector to be released into the cytosol (H) and starting its toxic cascade (I). Figure adapted from [68].

Once inside the cell, the HVR exerts its enzymatic activity, which includes ADP-ribosylation of actin (e.g., TccC3 in *Photorhabdus luminescens*) or Rho GTPases (e.g., TccC5) [91]. Unlike most other actin-targeting toxins modifying monomeric actin (G-actin), TccC3 specifically targets filamentous actin (F-actin) [92, 93]. It was shown to facilitate the ADP-ribosylation of actin at threonine-148, a site located between two subunits within the actin filament [92, 93]. The addition of this bulky ADP-ribose group has significant consequences for the actin cytoskeleton: It blocks the binding of actin-depolymerizing factors such as cofilin, making the modified filaments resistant to disassembly, therefore inhibiting actin-associated rearrangements and transport systems [92-94]. TccC5, on the other hand, acts as an ADP-ribosyltransferase, covalently attaching an ADP-ribose group to glutamine-61 and -63 on Rho family proteins, including RhoA and Cdc42 [91]. The added ADP-ribose group sterically blocks Rho GTPases from interacting with their downstream effector proteins, effectively stopping their ability to regulate actin dynamics, cell adhesion, and motility. These processes result in cytoskeletal disruption, immune evasion, or apoptosis.

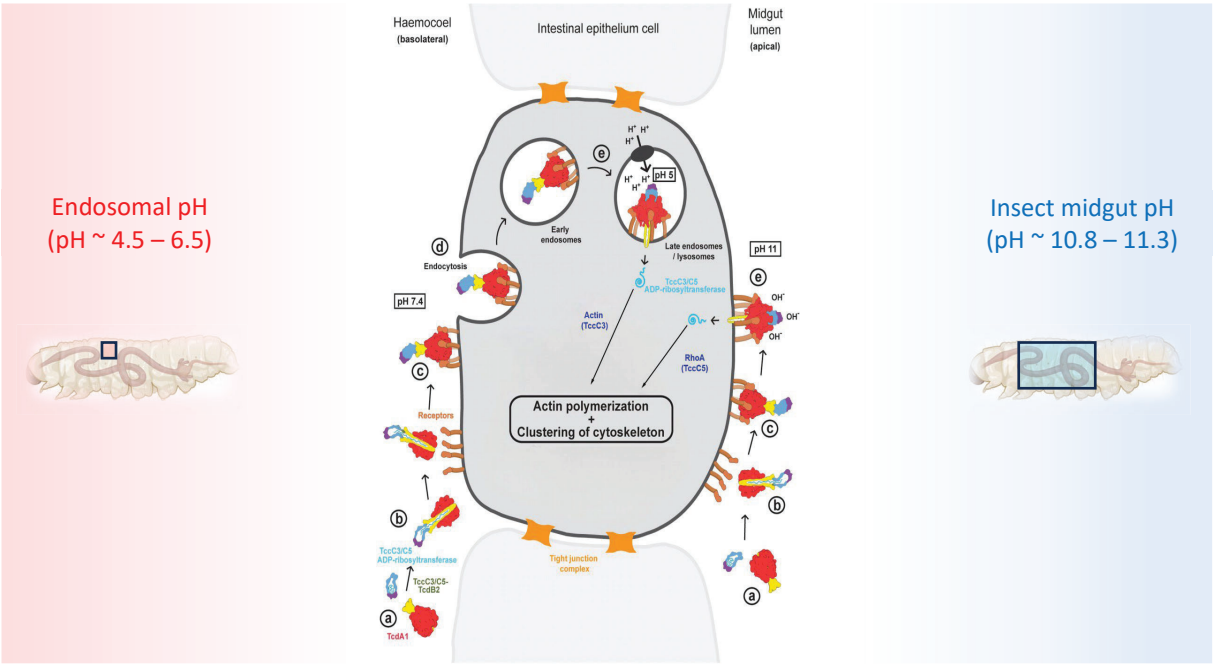

Figure 8: Overview of Tc toxin infection pathways
Proposed infection cycles depending on the infected sample. For all non-midgut attacks, toxin activation follows the endosomal pathway, hijacking the endosomal maturation as a triggering factor for toxin activation (left-hand). If toxins are released into the insect midgut, activation is mediated by the alkaline pH environment (~11) following receptor binding, allowing for direct translocation through the plasma membrane. Figure kindly provided by Dr. P. Ng'ang'a.

So far, little is known about the general production of Tc toxins and their release. However, recent studies on Tc toxins from *Yersinia entomophaga* (YenTc) revealed that the assembly and release of YenTc are highly specialized processes [24, 25]. Only a subpopulation of *Y. entomophaga* cells, termed 'soldier cells', express YenTc and other virulence factors, which in turn are primed by external factors (Figure 9). These soldier cells undergo a controlled, phage-like lysis mediated by a dedicated lysis cassette, known as the T10SS (type 10 secretion system), to release YenTc into the environment. This stepwise release mechanism is thought to minimize the number of cells sacrificed, thereby conferring a survival advantage to the bacterial population.

Overall, these intricate adaptation, recognition, and evasion features, together with the highly modular nature of Tc toxins, are of increasing interest for potential translational research.

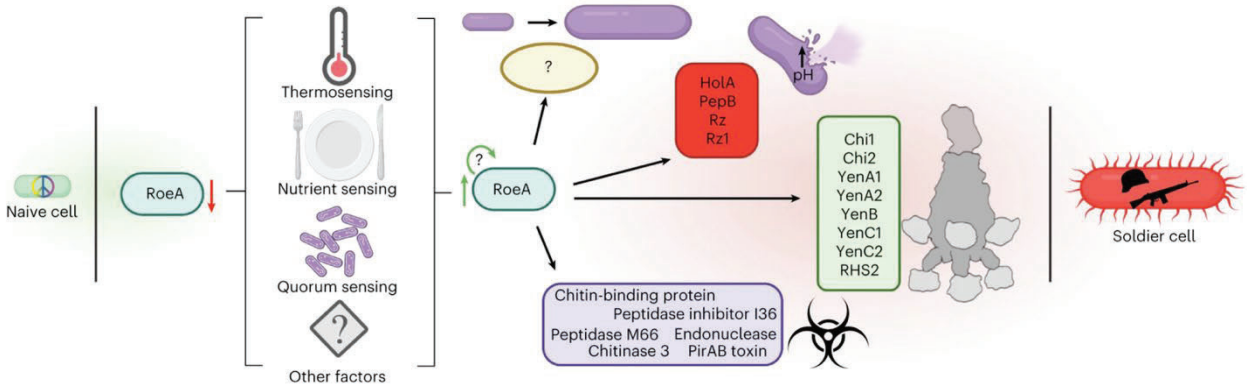

Figure 9: Production and release scheme of YenTc toxin
Schematic overview of the type 10 secretion system. In the absence of external signals, the RoeA gene is downregulated. Upon influences like specific temperatures, the availability of nutrients or high densities of bacteria in proximity, RoeA is upregulated which turns the cells into 'soldier cells' with increased toxin production, including YenTc, but also an overexpression of holins and other protein classes that ultimately lead to the explosion of cells, releasing the toxin cocktail into the surrounding. Figure taken from [95].

4.5 PFTs and translational research

PFTs and their ability to self-assemble into oligomeric complexes, inserting themselves into cellular membranes or forming transmembrane channels, are raising increasing scientific interest, also from other disciplines [28]. The versatility of PFTs has already led to their use in diverse applications. In medicine, engineered PFTs are being explored for targeted cancer therapies and as antimicrobial agents (e.g., biopesticides) [89, 96]. In biotechnology, their use for high-precision biosensing and sequencing technologies is being investigated in detail [97, 98].

Biopesticides, which are pesticides derived from natural sources such as bacteria, plants, or animals, can be categorized into three main classes [99, 100]. The first class, biochemical pesticides, consists of naturally occurring small molecules from plants and animals that control pests through non-toxic mechanisms, such as disrupting mating signals or attracting pests to traps. The second class, microbial pesticides, involves the use of whole microorganisms, such as bacteria, fungi, viruses, or nematodes, that produce toxins upon infecting insect hosts.

These microbial agents often target a broad spectrum of pests, with each toxin complex acting on specific targets. The third class, plant-incorporated protectants (PIPs), involves genetically modifying plants to express genes encoding natural toxins, such as the Cry proteins from *Bacillus thuringiensis*, enabling the plants to produce the active toxin themselves and for protection against pests without further intervention.

Compared to conventional chemical pesticides, biopesticides offer several advantages. They are generally more specific to their target pests and environmentally friendly, as they do not leave harmful residues. This specificity reduces the risk of off-target effects, including those

caused by beneficial insects, birds, and mammals. Additionally, it reduces health risks associated with food consumption and environmental contamination. However, before these toxins can be harnessed for commercial or therapeutic purposes, it is essential to characterize their structural and functional properties thoroughly to adapt their features successfully for translational concepts. To achieve this, cryo-EM and cryo-ET, in particular, are valuable techniques due to their ability to visualize multiple conformations, or, in the case of cryo-ET, various proteins or whole cells and tissues.

4.6 Structural biology (Cryo-electron microscopy)

Cryo-electron microscopy (cryo-EM) has emerged as a revolutionary technique in structural biology, enabling the visualization of macromolecular structures at near-atomic resolution without the need for crystallization [101, 102].

Cryo-EM encompasses two primary approaches: single particle analysis (SPA) and cryo-electron tomography (cryo-ET), each with distinct applications and capabilities [103-106].

Single particle cryo-EM focuses on the structural determination of purified proteins and macromolecular complexes (= single particles). Being an averaging technique, SPA requires a multitude of particle images that are reconstructed into a complete 3D volume. To achieve this, the proteins or complexes are usually purified to guarantee a homogeneous sample. This sample is plunge-frozen in a thin, vitreous ice layer on holey films, ideally in all possible orientations. Those holes are then imaged in a transmission electron microscope (TEM), resulting in thousands of particle images representing the target of interest in various orientations. The vitrification process is necessary to minimize sample damage throughout the acquisition and still avoid additional signals from ice crystals forming within the frozen layers. Advanced software then enables alignment and reconstruction of a 3D volume corresponding to an average of all particles [107-109]. SPA has revolutionized structural biology, achieving resolutions of up to 1.09 Å for some samples and enabling the study of large, dynamic protein complexes that were previously challenging to analyse using traditional methods, such as X-ray crystallography (Figure 10, left-hand) [110, 111]. Whereas crystals typically capture only one homogeneous protein state, SPA can differentiate and reconstruct multiple conformations in a single dataset, provided that the number of particles is sufficiently large and the states are homogeneous and not too flexible within themselves.

In situ Cryo-ET, on the other hand, allows for the visualization of cellular structures in their native context. Therefore, in contrast to single-particle analysis, entire cells or tissues are

plunge-frozen or high-pressure-frozen, depending on their ability to undergo vitrification [112]. Since most samples or tissues are too thick to be electron-transparent (commonly below 200 – 300 nm) when imaged directly, an intermediate thinning is required, which can be performed using focused ion beams (FIB), also known as FIB milling. Upon generating these thin, electron-transparent sections, known as lamellae, the samples are then imaged in a TEM by stepwise tilting of the stage. In doing so, the resulting tilt series can be reconstructed into 3D volumes, known as tomograms. After acquisition of sufficient tomograms and identification of the target of interest, subunits of the tomograms containing the ROI can be extracted and, in a similar fashion to single particle analysis, be used to reconstruct averaged 3D volumes, a process called sub-tomogram averaging (Figure 10, right panel) [113].

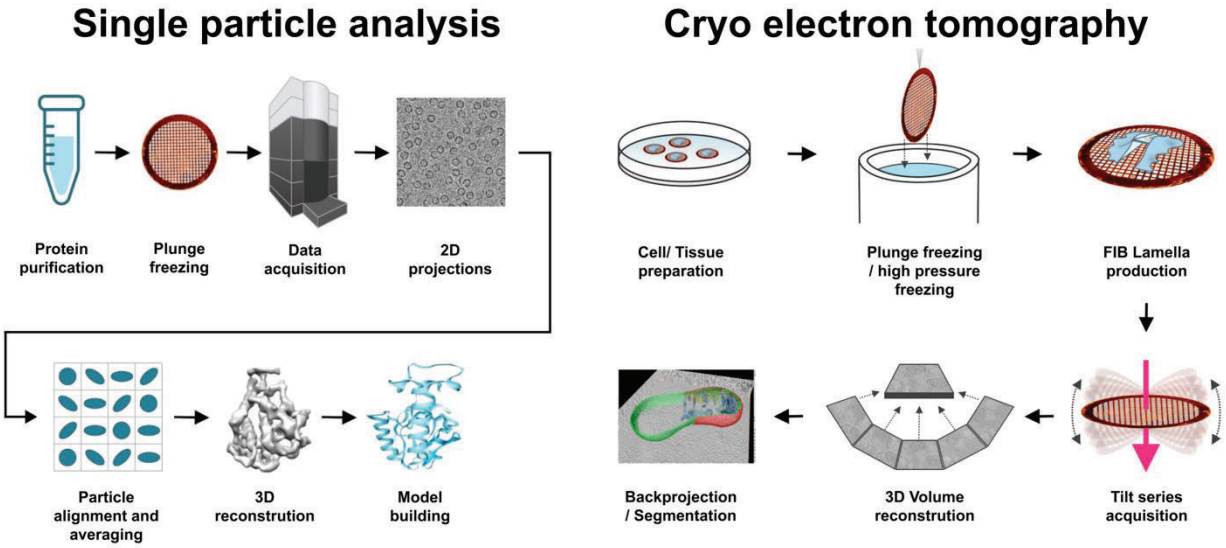

Figure 10: General concepts of SPA and cryo ET
The two most common methods in cryo-electron microscopy are single-particle analysis (SPA), in which the molecule of interest is purified and plunge-frozen onto an EM grid, allowing for imaging in a TEM. Using computational tools, the target molecules are then identified in the resulting images and, with the help of 2D projections and 3D reconstructions, refined into a 3D model (left-hand). Cryo-electron tomography focuses on whole biological samples, such as cells or tissues. Herefore, the specimen is plunge-frozen (or high-pressure-frozen if thickness levels are too high) and preprocessed using cryo-FIB milling to thin the sample for further imaging. During data acquisition, the stage is tilted, resulting in a 3D reconstruction of the imaged tilt series for further segmentation or subtomogram averaging. Figure is adapted from MyScope (https://myscope.training/CRYO_introducing_cryo_TEM).

Cryo-ET provides a unique bridge between cellular and molecular biology, offering insights into the spatial arrangements of macromolecular complexes within their cellular environment at the nanometer scale, even allowing, in exceptional cases, resolution ranges comparable to single particle analysis, like an unprecedented 4.5 Å reconstruction of filamentous actin from mouse muscle [114].

Both SPA and cryo-ET have benefited from recent technological advancements, including improved direct electron detectors, phase plates, and sophisticated image processing algorithms

[102, 103]. These developments have dramatically enhanced the resolution and applicability of cryo-EM techniques, leading to their widespread adoption in structure biology research. One significant advancement in cryo-ET is the usage of fluorescent signals (emitted by the targets of interest) during localization, hence referred to as correlative light and electron microscopy (cryo-CLEM) [115, 116].

4.7 Correlative light and electron microscopy (CLEM)

Correlative Light and Electron Microscopy (CLEM) is a powerful imaging approach that combines the strengths of light microscopy (LM) and electron microscopy (EM) to provide comprehensive insights into biological structures and processes across multiple scales [115]. This technique allows researchers to bridge the gap between cellular function and ultrastructure by integrating the molecular specificity of fluorescence microscopy with the nanoscale resolution of electron microscopy [117].

CLEM encompasses a variety of methods that enable the visualization of the same target of interest using both LM and EM modalities. The primary advantage of this approach lies in its ability to correlate dynamic cellular processes and specific molecular markers observed through fluorescence microscopy with high-resolution ultrastructural details obtained from electron microscopy (Figure 11) [118].

In the context of cryogenic CLEM, correlation is especially challenging since the vitrification process, necessary for optimal results from EM, interferes with the signal detected via LM and therefore requires countermeasures. Ice reflections or auto-fluorescent effects decrease the signal-to-noise ratio in LM. They can currently only be addressed with specialized filters or software tools that subtract the signals during post-processing [119, 120].

Recent advancements in CLEM have expanded its capabilities and applications. The development of integrated systems that allow for both LM and EM imaging within a single instrument has streamlined the correlation process and reduced the risk of sample contamination or loss [121-123]. Additionally, the incorporation of super-resolution optical techniques such as STORM, PALM, and STED has further enhanced the resolution achievable in the light microscopy component of CLEM [115].

CLEM has found applications across various fields in the life sciences, including neuroscience, cell biology, and tissue research [116, 124]. It has been particularly valuable in studying rare cellular events, complex cellular structures, and dynamic processes that require both temporal and spatial context.

As the field continues to evolve, ongoing improvements in sample preparation techniques, imaging hardware, and correlation software are expected to further enhance the resolution, speed, and accessibility of CLEM, solidifying its position as an essential tool in modern biological research [115].

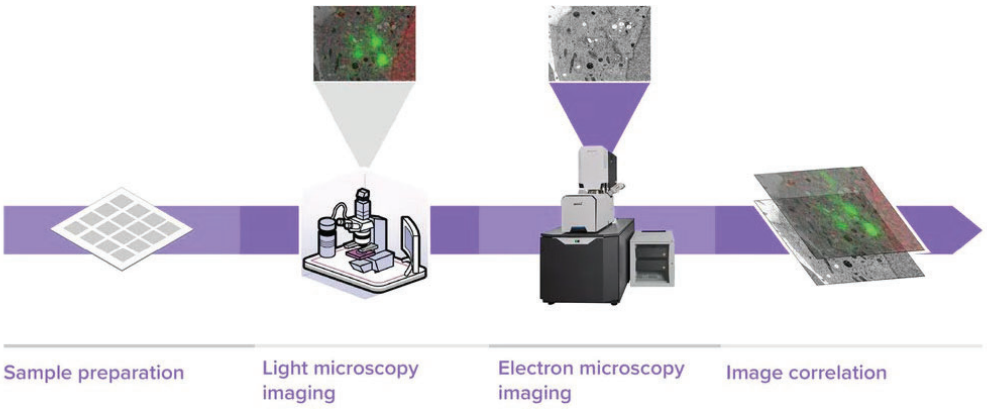

Figure 11: Cryo CLEM
Correlative light and electron microscopy requires sample preparation that enables imaging with both light microscopy approaches and electron microscopy. Using computational tools to accurately overlay features present in both imaging modes (e.g., grid bars) allows a precise correlation of the target of interest. Figure is adapted from Delmic (https://blog.delmic.com/unlocking-the-potential-of-clem-with-high-throughput-electron-microscopy).

5 Aims and Motivation

Tc toxins are not only promising tools for sustainable agriculture, offering alternatives to chemical pesticides, but they also become increasingly interesting for translational applications, for example, as molecular syringes. However, for a safe and targeted use of bacterial toxins in medical therapies, it is essential to understand all the underlying molecular mechanisms completely. In this context, one of the most critical remaining questions is how exactly the interactions between cells and external factors work together to mediate pore formation. For this purpose, one aim of my thesis was to identify a potentially general mechanism by which shell-opening and pore formation are triggered and facilitated in Tc toxins.

Previous studies already identified intermediate states between prepore and pore, most of which, however, were too short-lived to be characterised structurally. Furthermore, other studies have already suggested the importance of electrostatic switches, such as salt bridges, for the regulation of pore formation, but have not identified a general trigger factor. To further this knowledge, I aimed to acquire high-resolution structures of *Photorhabdus luminescens* TcdA1 WT in its prepore and pore states, as well as several mutants that either exhibited an increased or decreased tendency to form pores. I then analysed their structural differences to identify standard key features concerning pore formation. Together with multiple sequence alignments (MSA) of other Tc toxins, including some for which the structures have already been solved, this could provide vital insights into the conserved mechanism underlying the entire process of Tc toxin pore formation.

Another aim of my thesis was to analyze the function of a highly specialized Tc toxin, thereby understanding the underlying differences in more detail and providing a basis for rational design concepts. Previous studies had identified YenTc, a Tc toxin from *Yersinia entomophaga*, as a specialized toxin due to its unknown chitinase activity. So far, however, structural analysis has only provided medium-resolution reconstructions of this Tc toxin, preventing a more detailed investigation of the general mechanism of activation.

To this end, I planned to obtain high-resolution reconstructions of both YenTc pre- and pore states, thereby building a more complete model and deducing characteristics that could explain the activation of this toxin. By combining structural analysis with mass spectrometry, I aimed to identify time-sensitive processes and provide insights into the usage of the three C-component isoforms as toxic effectors.

The final goal was to monitor the infection pathway of Tc toxins using fluorescence microscopy, as well as cryo-electron tomography, allowing for near-native imaging of toxins throughout the cells.

Earlier studies attributed Tc toxin entry to the endosomal pathway; however, direct insertion has also been proposed for alkaline pH ranges in the insect midgut lumen. To address these distinct possibilities, my aim was to develop a fluorescence reporter system for the endosomal pathway, which, when combined with fluorescently labelled toxins, would enable the identification and localization of these toxins within cells.

Further employing cryo-CLEM could improve the tracking of Tc toxin within cells, ultimately providing novel insights into how Tc toxins interact with cells and which entry pathway(s) they utilise.

Taken together, these insights could provide the basis for optimizing Tc toxin use as molecular machines.

6 Material and Methods

6.1 Material

6.1.1 Instruments

Instrument	Manufacturer
ÄKTA pure	GE Healthcare
Analytical balance PT1200	Sartorius
Autoklav LaM-4-20-MCS-J	SANOclav
Biometra TOne	Analytikjena
C1000 Touch Thermal Cycler	Bio-Rad
Carbon evaporator Leica EM ACE600	Leica Microsystems
Centrifuge 5424	Eppendorf
Centrifuge Allegra® X-15R	Beckman Coulter
Centrifuge Avanti® J-26XP	Beckman Coulter
Centrifuge Avanti® JXN-26	Beckman Coulter
Centrifuge Rotors (JLA 8.100, JA-25.50, JA-10)	Beckman Coulter
ChemiDoc MP Imaging System	Bio-Rad
CorrSight	Thermo Fisher Scientific
Countess II FL Automated Cell Counter	Thermo Fisher Scientific
Electron microscope Talos Arctica	Thermo Fisher Scientific
Electron microscope Titan Krios	Thermo Fisher Scientific
Electron microscope Aquilos 2 Cryo-FIB	Thermo Fisher Scientific
Electron microscope Hydra Bio Plasma-FIB	Thermo Fisher Scientific
Electroporator Gene Pulser Xcell™System	Bio-Rad
EM GP2 Automatic Plunge Freezer	Leica
FEI Tecnai Spirit	Thermo Fisher Scientific
Fluorescence microscope (EVOSFL Auto)	Life Technologies
GloCube Plus	Quorum Technologies Ltd
Heat shock bath	TW2 JULABO
Incubator (37 ° C)	BINDER
LAUDA Hydro H4	LAUDA
Magnetic stirrer MR3000	Heidorph
Magnetic stirrer VMS A	VWR
Meteor	Delmic
Microfluidizer Model 110S	Microfluidics Corporation
Microwave Continent MW 800 G	IKA Labortechnick
Mini-membrane-vacuum pump Laboport®	KNF
Mini-PROTEAN® Tetra-Cell	Bio-Rad
Molecular Imager® Gel Doc™ XR System	Bio-Rad
NanoDrop Spectrophotometer ND-1000	PEQLAB
NGC Discover™ 10 Chromatography System	Bio-Rad
pH-Meter FE20 Five Easy™	Mettler Toledo
Pipettes PIPETMAN (0,2-2µl, 1-10µl, 2-20µl, 20-200µl, 100-	Eppendorf

1000µl)	
Pipetting device	Hirschmann Laborgeräte
PowerPac 300	Bio-Rad
PowerPac HV Power Supply	Bio-Rad
Shaker	INFORS HT
Shaker Excella E24	Eppendorf
Sonicator-Sonifier-Branson	VWR International
Tabletop centrifuge 5417R	Eppendorf
ThermoMixer C	Eppendorf
ThermoStat Plus	Eppendorf
Ultracentrifugation rotors (Ti70, Ti45, TLA-120.1, TLA-55)	Beckman Coulter
Ultracentrifuge Optima™ XPN-80	Beckman Coulter
Ultrasonic bath	Sonorex Digitec Bandelin
Vitrobot cryo plunger	Thermo Fisher Scientific
Vortex-Genie 2	Scientific Industries
Zeiss LSM800 microscope with Airyscan	Carl Zeiss Microscopy GmBH

6.1.2 Chemicals

Name	Supplier
Acetic acid (glacial)	Sigma-Aldrich
Agarose	Biozym Scientific GmbH
Ampicillin	Gerbu
Alexa Fluor™ 488 NHS Ester (Succinimidyl Ester)	Thermo Fisher Scientific
CAPS	Anatrace
CellLight™ Early Endosome-GFP, BacMam 2.0	Thermo Fisher Scientific
CellLight™ Late Endosome-GFP, BacMam 2.0	Thermo Fisher Scientific
CellLight™ Lysosomes-GFP, BacMam 2.0	Thermo Fisher Scientific
Collodion solution	Sigma-Aldrich
Complete, EDTA-free protease inhibitor	Roche Holding AG
Coomassie Brilliant Blue R250	SERVA Electrophoresis GmbH
Di-potassiumhydrogenphosphate	Roth
DMSO	Sigma-Aldrich
Dulbecco's Modified Eagle Medium (DMEM)	Life Technologies
Dulbecco′s Phosphate Buffered Saline	Sigma-Aldrich
Ethanol	Thermo Fisher Scientific
Ethylenediaminetetraacetic acid (EDTA)	Carl Roth
FBS (Fetal Bovine Serum)	Life Technologies
Fibronectin Bovine Plasma	Sigma-Aldrich
Freestyle 293 expression medium	Life Technologies
FuGENE® transfection reagent	Promega
Glycerol	GERBU
HEPES	VWR

Hydrochloric acid	J.T. Baker
Imidazole	Sigma-Aldrich
IPTG	Sigma-Aldrich
Isopropanol	Carl Roth
Lipofectamine® 3000 transfection reagent	Thermo Fisher Scientific
Methanol	J.T. Baker
MG-132	Sigma-Aldrich
Midori green	NIPPON Genetics
Molecular Probes™ Alexa Fluor™ 647 C_2 Maleimid	Thermo Fisher Scientific
Monomaleimido Nanogold	Nanoprobes
Mono-Sulfo-NHS-Nanogold	Nanoprobes
Nanogold – 5nm	Nanoprobes
Opti-Mem reduced serum media	Life Technologies
Penicillin-Streptomycin/A	PAN-Biotech GmbH
Phenylmethylsulfonyl fluoride (PMSF)	Sigma-Aldrich
Protino Ni-IDA Resin	Macherey-Nagel
Sf-900 III SFM	Life Technologies
Sodium chloride	Roth
Sodium cholate	VWR
Sodium dodecylsulfate (SDS)	Roth
Sodium hydroxide	Waldeck
Tris PUFFERAN	Roth
Triton X-100	Anatrace
Trypan blue	FLUKA
Tween-20	Anatrace
Uranyl formate	Polysciences Inc.

6.1.3 Media and Buffer

Name	Ingredients
SOC-Media (1 l)	20 g tryptone, 5 g yeast-extract, 0.58 g NaCl 0.19 g KCl, 2.03 g $MgCl_2 \cdot 6\ H_2O$, 2.46 g $MgSO_4 \cdot 7\ H_2O$, 50% glucose solution
LB-Media (1 l)	10 g bacterial tryptone, 5 g yeast extract, 10 g NaCl
10x PBS (500 ml)	40 g NaCl, 1 g KCl, 9.02 g Na2HPO4 · 2 H2O 1.2 g K2PO4, adjust to pH 7.4
SDS sample buffer (4x)	250 mM Tris-HCl (pH 8), 100 mM DTT, 6% SDS, 40% glycerol, 0.02% Bromophenol blue
10x SDS running buffer	250 mM Tris-HCl (pH 8), 1.9 M glycine, 2.8% SDS

Coomassie staining solution	0.15% Coomassie Brilliant Blue R250, 12% Acetic acid, 44% Ethanol
Coomassie destaining solution	10% Acetic acid
Lysis buffer (TcdA1)	300 mM NaCl, 20 mM Tris-HCL (pH 8), 1 mM DTT, 500 µM EDTA, 10% glycerol, Benzonase, 10 µM DTT, 1mg/ml lysozyme
Wash buffer (TcdA1)	500 mM NaCl, 20 mM Tris-HCl (pH 8), 0,05% Tween-20, 20 mM imidazole, 5% glycerol
Elution buffer (TcdA1)	500 mM NaCl, 20 mM Tris-HCl (pH 8), 0.05% Tween-20, 500 mM imidazole, 5% glycerol
Dialysis buffer (TcdA1)	100 mM NaCl, 50 mM Tris-HCl (pH 8), 0.05% Tween-20, 5% glycerol
Secretion buffer (YenTc)	300 mM NaCl, 20 mM Tris-HCl (pH 8), 1µl Benzonase, 1 pill of Roche cOmplete protease inhibitor, 20 mM imidazole
Elution buffer (YenTc)	300 mM NaCl, 20 mM Tris-HCl (pH 8), 500 mM Imidazole
Cholate buffer (YenTc)	20 mM Tris-HCl (pH 8), 250 mM NaCl, 1% Na cholate
Dialysis buffer (YenTc)	20 mM CAPS (pH 11.2), 250 mM NaCl
Storage buffer (YenTc)	250 mM NaCl, 20 mM Hepes (pH 7.4), 0.05% Tween-20

6.1.4 Cell lines

Organism	Name	Description
Escherichia coli	TOP10F'	F' [proAB, lacIq, lacZΔM15, Tn10(TetR)] mcrA, Δ(mrr-hsdRMS-mcrBC), φ80lacZΔM15, ΔlacX74, deoR, recA1, λ-
Escherichia coli	XL10 Gold	Tet^{r}Δ(*mcrA*)183 Δ(*mcrCB-hsdSMR-mrr*)173 *endA1 supE44 thi*-1 *recA1 gyrA96 relA1 lac* Hte [F′ *proAB lacI*^{q}ZDM15 Tn*10* (Tet^r) Amy Cam^r]
Escherichia coli	BL21(DE3) RIPL	*E. coli* B F$^–$ *ompT hsdS*(rB– mB–) dcm$^+$ Tet^r gal λ(DE3) *endA* Hte [*argU proL Camr*] [*argU ileY leuW* Strep/Spec]
Escherichia coli	BL21(DE3)	F– dcm ompT hsdS(r – m –) gal λ(DE3)
Escherichia coli	DH10EmBacY	F-mcrA Δ(mrr-hsdRMS-mcrBC) φ80lacZΔM15 ΔlacX74 recA1 endA1 araD139 Δ (ara, leu)7697 galU galK λ-rpsL nupG/ bMON14272/ pMON7124
Homo sapiens	HEK293T	Adherent human embryonic kidney cells
Spodoptera frugiperda	Sf9	Immortalized insect ovarian cell line
Homo sapiens	HeLa	Immortalized, adherent human cervical cancer cell line
Yersinia entomophaga	*Y.e.* MH96	Gram-negative, rod-shaped, non-spore-forming bacterium

6.1.5 Consumables

Material	Supplier
10 cm petri-dish, sterile	Sarstedt
6,12,24, and 96-well plates (sterile)	Sarstedt
96-well deep well plates 2,2 ml	VWR
Amicon®Ultra-4 und 15 Concentrator	Merck Millipore
Copper grids (for negative stain)	Plano
Eppendorf tubes (0,5 ml, 1,5 ml, 2 ml und 5 ml)	Sarstedt
Falcon tubes (15 ml and 50 ml)	Sarstedt
Falcon tubes (50 ml)	Greiner
Filter paper Whatman No.4	GE Healthcare
Filtropur V50 250/500ml, 0.22µm	Sarstedt
PageRuler Prestained protein ladder	Thermo Fisher Scientific
Parafilm	Pechiney Plastic Packaging
Pipette tips (10 µl, 200 µl, 1.25 ml)	Sarstedt
QIAprep Spin Miniprep Kit	QIAGEN
QIAquick Gel Extraction Kit	QIAGEN
QIAquick PCR Purification Kit	QIAGEN
QUANTIFOIL R 1.2/1.3 Au (300 mesh)	Quantifoil Micro Tools
QUANTIFOIL R 1.2/1.3 Cu (200 or 300 mesh)	Quantifoil Micro Tools
QUANTIFOIL R 2/1 Cu (300 mesh)	Quantifoil Micro Tools
QUANTIFOIL R 2/1 Cu + 2nm C Layer (200 or 300 mesh)	Quantifoil Micro Tools
QUANTIFOIL R 2/1 Au + 2nm C Layer (200 or 300 mesh)	Quantifoil Micro Tools
SDS-Gels Mini-PROTEAN TGX Stain Free Precast Gels (4-15%, 15 wells)	Bio-Rad
Serological Pipettes, sterile (5 ml, 10 ml und 25 ml)	Sarstedt
Serological Rotilabo®-Pipettes (5 ml, 10 ml und 25 ml)	Roth
Spectra HR ladder	Thermo Fisher Scientific
UltrAuFoil Holey Gold Films R 1.2/1.3 (300 mesh)	Quantifoil Micro Tools

6.2 Methods

6.2.1 Protein expression and purification (YenTc)

Y. entomophaga type strain MH96 with an arabinose-inducible Ara-YenR plasmid was grown for 16 h at 30° C in 1 L SOC medium [95]. Upon induction with 0.5% I-arabinose, the temperature was lowered to 20 °C. After 16 h incubation, the culture was centrifuged for 20 min at 5000 rpm, and the supernatant was discarded. The cell pellet was then resuspended in 50 ml of 100 mM Tris-HCl, pH 8.0, and 100 mM NaCl buffer to start the secretion. After 3 hours, the cells were once more centrifuged for 20 min. In contrast, this time the pellet was discarded, and the supernatant was used for further purification and treatment according to the purification protocol of TcdA WT described previously [88].

Pore formation (Lollipop) was induced by integration of the purified toxin into cMSPΔH5-POPC Nanodiscs in cholate buffer (20 mM Tris-HCl pH 8, 250 mM NaCl, 1% Na cholate) and subsequent dialysis in 1 L buffer (20 mM CAPS pH 11.2, 250 mM NaCl) using 20 kDa MWCO Slide-a-lyzer for 48 h. To obtain the neutral pH pore, instead of applying freeze-thaw cycles as earlier described [79], the Tween20 concentration was temporarily increased while running the solution through a PD Spintrap™ G-25 (GE Healthcare Life Sciences) column before putting it back to plunging condition (25 mM Hepes, 200 mM NaCl, 0.05% Tween20).

6.2.2 Cryo-EM grid preparation (YenTc)

4 µl of YenTc Holotoxin (2.8 mg/ml for prepore, 3.5 mg/ml for lollipop, and ~ 6 mg/ml for the neutral pore in 0.05 % Tween20) was pipetted onto glow-discharged R2/1 Au 200 mesh + 2nm carbon grids (Quantifoil) for prepore and R2/2 200 mesh UltrAUfoil grids (Quantifoil) for lollipop and neutral pore. Following an incubation period of 20 seconds for the pre-prepared sample and zero for the other samples, the surplus solution was removed by blotting, and the grids were plunged frozen in liquid ethane or a liquid ethane/propane mixture using a Vitrobot Mark IV (Thermo Fisher Scientific). The Vitrobot was operated at 12 ° C and 100% humidity, and the samples were blotted for 3 s with a blot force of −1.

6.2.3 Cryo-EM grid screening and data collection (YenTc)

Grids were initially examined using a 200 kV Talos Arctica microscope (Thermo Fisher Scientific) equipped with a Falcon III detector (Thermo Fisher Scientific). Low-magnification grid overviews (atlases) were routinely acquired with EPU software (Thermo Fisher Scientific). Grids showing the best YenTc concentration and distribution were moved from the microscope and placed in auto grid boxes (Thermo Fisher Scientific), then stored in liquid nitrogen for subsequent high-resolution data collection. All datasets were acquired on a 300 kV Titan Krios microscope (Thermo Fisher Scientific) equipped with a K3 detector (Gatan) and a post-column energy filter set to a 20 eV slit width. Videos were recorded in super-resolution mode at a pixel size of 0.44 Å, and no objective aperture was used.

All datasets were collected on the same microscope at the same magnification of 81,000x, to ensure that the resulting cryo-EM density maps could be compared directly without issues caused by pixel size discrepancies. Using EPU, 20,000 (for prepore), 11,000 (for lollipop), and 12,000 (for neutral pore) movies per dataset were collected in 60 frames at a total electron exposure of about 70–90 e-Å-2. The defocus values set in EPU ranged from −0.8 to −1.8 µm. The data quality was monitored live during acquisition using TranSPHIRE [125]. If necessary, the microscope was realigned to ensure optimal imaging conditions.

6.2.4 Cryo-EM image processing (YenTc)

For each dataset, video preprocessing was carried out in real time using TranSPHIRE [125]. The super-resolution movies were binned by a factor of two (yielding a final pixel size of 0.88 Å), gain corrected, and motion corrected with UCSF MotionCor2 [126]. Contrast transfer function (CTF) parameters were estimated using CTFFIND 4.13 [127]. YenTc toxins were automatically picked with the general model in SPHIRE_crYOLO, employing a box size of 350 pixels and ensuring less than 50 pixels of overlap [128]. The selected particles were then extracted in boxes of 640 × 640 pixels using RELION 4.0 and subsequently imported into CRYOSPARC [108, 129].

In all datasets, the particles were two-dimensionally classified using ’2D classification’ [108]. All classes were manually inspected using ‘Select 2D classes’ and those that represented light artifacts and ice contaminations were discarded [108]. The passing particles were subjected to three-dimensional refinement using first ‘ab-initio reconstruction’ to obtain an initial map and then further refined in ‘non-uniform refinement’ [108, 130].

We refined the YenTc structures with and without applying C5 symmetry. These refinements yielded YenTc reconstructions at resolutions of 2.7–4.5 Å. The particles were then converted to be compatible with Relion, again. In Relion 4.0, the particles underwent Bayesian polishing to enhance the estimation of particle motion trajectories caused by beam-induced movement [131]. Additionally, CTF refinements were performed to determine per-particle defocus values and to correct for beam tilt, trefoil (threefold) astigmatism, spherical aberration (Cs), tetrafoil (fourfold) astigmatism, and anisotropic magnification. Subsequently, we carried out three-dimensional classification without image alignment (using five classes, 25 iterations, and a tau2fudge value of 4) to exclude particles that did not contribute high-resolution information to the reconstruction.

Typically, one or two high-resolution classes containing most particles were selected, and the other low-resolution classes were discarded. Finally, after removal of duplicates, this set of particles was converted back to CRYOSPARC and subjected to a ‘local refinement’ (focused refinement) [108]. These refinements yielded cryo-EM density maps at resolutions of 2.5–4.0 Å according to the gold-standard FSC = 0.143 criterion. The final maps were sharpened with a negative B-factor. Local-resolution estimations were performed in the job ‘Local resolution’ [108].

Composite maps were generated from the focused refinements using the ‘Combine Focus Maps’ Option in Phenix [132]. To resolve the density related to Chitinase1, a masked 3D variability analysis was performed, and particles corresponding to one conformational state were

used for a ‘local refinement’ [133]. For YenC1 and YenC2, structural models were obtained by AlphaFold2 predictions, and a homology search was performed using Foldseek [134, 135].

6.2.5 Model building, refinement, and analysis (YenTc)

To build the YenTc models in the high-resolution density maps, the structures of YenTcA in its prepore state (PDB 6OGD) as well as the crystal structures of both Chitinases (PDB 4A5Q and 3OA5) and the BC-complex (PDB 4IGL) were rigid-body fitted into the map of the YenTc prepore state. Each protomer in the map was then rebuilt in Coot manually, gaps closed, and the other YenTc subunits were adjusted in ChimeraX by applying C5 symmetry to the A subunit [136, 137]. The structure was then iteratively refined using Coot (manually), ChimeraX plugin ISOLDE, and phenix real-space refine with non-crystallographic symmetry restraints but without imposing any geometry restraints [132, 136, 138, 139].

The structures of all remaining states were generated by first performing rigid-body fitting of the YenTc prepore model into the map, followed by manual refinement using Coot. Subsequent structural refinement was carried out through iterative cycles in Coot, ISOLDE, and phenix real-space refinement. Solvent molecules (water) were manually positioned in Coot at the center of a single A subunit and then replicated using C5 symmetry.

Given that the local resolution of each Yen-Tc reconstruction was highest at the center and decreased toward the edges, all water molecules were carefully inspected before the final phenix refinement; any water molecules lacking apparent cryo-EM density were omitted. All figures and movies illustrating cryo-EM density maps and protein structures were created using UCSF ChimeraX [136]. Analysis of interaction interfaces was performed using PISA [140].

6.2.6 Intoxication assay

HEK293T cells (Thermo Fisher) were intoxicated with holotoxin from YpTcAB (WT) and YpTcAB (fused linker). Cells (2 × 10) were grown adherently in 400 µl DMEM/F12 medium (Pan Biotech) overnight and, subsequently, 1 or 50 nM of holotoxin was added. Incubation was allowed to continue for 16 h at 37 ° C before imaging.

6.2.7 Negative stain imaging

For initial control with negative stain EM, the proteins were applied to glow-discharged copper grids with an 8 nm amorphous carbon layer, stained with 0.75% uranyl-formate, and imaged using a Tecnai Spirit transmission electron microscope (Thermo Fisher) operated at 120 kV and equipped with a TVIPS TemCam F416 detector. Images were recorded at a pixel size of 2.61 Å/pixel.

6.2.8 Electroporation of DH10EmBacY *E. coli* cells

A total of 100 µl of electrocompetent DH10EMBacY cells was carefully combined with 50 ng of plasmid DNA. This mixture was transferred into a 2 mm electroporation cuvette, which was then inserted into the electroporator. An electric pulse of 2.5 kV was applied for 5 milliseconds. Immediately afterward, 1 ml of pre-warmed SOC medium was added to recover the cells, and the suspension was incubated overnight at 37°C with shaking at 650 rpm.

The following morning, 100 µl of the cell suspension was plated onto agar containing 10 µg/ml tetracycline, 50 µg/ml kanamycin, 10 µg/ml gentamycin, one mM IPTG, and 100 µg/ml X-Gal. After 48 hours of incubation at 37°C, the plates were examined for single white colonies, indicating successful integration of the gene of interest (GOI) into the bacterial artificial genome.

6.2.9 Bacmid isolation from DH10EmBacY cells

A single white colony was transferred into 5 ml of LB medium supplemented with 10 µg/ml tetracycline, 50 µg/ml kanamycin, and 10 µg/ml gentamycin. The culture was incubated overnight at 37°C with shaking at 160 rpm. To extract the Bacmid DNA, the cells were harvested by centrifugation at 4000 × g at room temperature. Cell lysis was performed using the P1, P2, and N3 buffers from the Qiagen Plasmid Miniprep Kit. The lysate was centrifuged for 5 minutes at 15,000 × g at 4°C, and 720 µl of the clear supernatant was transferred to a new tube.

Subsequently, 500 µl of isopropanol was added to the supernatant to precipitate the DNA. The DNA pellet was collected by centrifugation at 16,900 × g for 10 minutes at room temperature, and the supernatant was carefully discarded. The pellet was then washed once with 200 µl of ice-cold 70% ethanol and finally resuspended in 30 µl of sterile water.

6.2.10 Transfection of *Sf*9 insect cells – baculovirus generation and amplification

For the production of virus stocks, Sf9 cells were transfected with the purified bacmid. Specifically, 100 µl of Sf-900 III SFM medium was added to 30 µl of the bacmid solution and mixed with 10 µl of FuGENE HD Transfection Reagent (Promega). This mixture was incubated at room temperature for 30 minutes. Meanwhile, 3 ml of Sf9 insect cells at a density of 0.7×10^6 cells/ml were allowed to settle in a 6-well plate at 27°C. The transfection mix containing the bacmid was then added dropwise to the cells. After incubating the cells in the dark at 27°C for four days, the P1 virus stocks were collected from the culture supernatant and supplemented with 2% (v/v) FBS for storage.

To obtain virus stocks with greater potency, further amplification was performed. P2 virus was generated by infecting 200 ml of Sf9 cells at a density of 1 × 10^6 cells/ml with 0.2% (v/v) of the P1 virus. Following 24 hours of incubation at 27°C with shaking at 100 rpm, 200 ml of fresh Sf-900 III SFM medium was added. Another 24 hours later, an additional 100 ml of fresh medium was introduced. The P2 virus was harvested from the supernatant after a total of five days. Cells were separated from the viral particles by centrifugation at 4000 × g for 10 minutes at room temperature. The resulting supernatant was filtered through a 0.22 µm filter, supplemented with 2% (v/v) FBS, and stored at 4°C.

6.2.11 Sample preparation for fluorescent reporter system

For expression of the target protein in mammalian cells, HeLa cells were grown in DMEM/F12 medium supplemented with 10% FBS and incubated at 37 ° C with 5% CO2 to a density of 1 x 10 cells/ml seeded onto R1/4 200 mesh Au grids which were coated with a 10 nm carbon layer in a 34 mm Mattek glass bottom dish. P2 virus was added up to 10% (v/v) of the initial culture volume, as well as 10 mM sodium butyrate. The container was returned to 37° C with 5% CO2 for 48h and later used for intoxication analyses. Successful transduction and expression were monitored using an EVOS Cell Imaging System or Zeiss LSM-800.

6.2.12 Intoxication of HeLa cells and cryo-preparation

The medium was removed from the glass bottom dish using an aspiration pump, washed three times with PBS, and replaced with DMEM/F12 medium supplemented with 2% FBS for 2-4h. After sufficient incubation, 10-100 nM of *Photorhabdus luminescens* Tc toxin - equal molar ratios of Nanogold labelled toxins as well as fluorescently labelled ones (Atto488-#565 + AF647-#613) – and five mM calcium chloride were added to the medium and returned to 37° C with 5% CO2 for one h.

Subsequently, the grids were taken out of the medium, dipped into PBS to remove access medium and then plunge frozen in liquid ethane or a liquid ethane/propane mixture using a Vitrobot Mark IV (Thermo Fisher Scientific) or a GP 2 Plunger (Leica). The Vitrobot was operated at 37 ° C and 100% humidity, and the samples were double-sided blotted for 10 s with a blot force of 10.

Thereafter, the plunge-frozen grids were clipped with FIB-compatible grid clips and stored in LN tanks until further usage.

6.2.13 Protein expression and purification (PlTcdA1)

Protein expression of TcdA1 (WT and mutants) was carried out by growing transformed E. coli strains in LB medium at 37 ° C until an OD600 of 0.5-0.8 followed by induction with 30 µM IPTG overnight at 20 ° C. After harvesting the cells and centrifugation for 30 min at 5000 rpm, the cells were resuspended in lysis buffer (5 g per 10 ml) and lysed using a fluidizer. Following centrifugation at 38000 rpm for 30 min to remove cell debris, the supernatant was mixed with Ni-IDA resin (0.15 g per 10 ml) and incubated overnight. Subsequently, the resin was thoroughly washed with wash buffer, and the bound protein was eluted with elution buffer.

Successful elution was monitored employing SDS-PAGE on collected samples during the process. After dialyzing the resulting protein solution overnight against 5 L dialysis buffer, the protein was further applied to size-exclusion chromatography and the corresponding sample fractions, controlled by SDS-PAGE, pooled, concentrated, and flash frozen to be stored until further usage at -80 ° C. The fusion construct TcB-TcC (WT and mutants) was expressed and purified similarly, with only slight changes.

For expression, the culture was directly induced with IPTG from the beginning, and the cells were grown at 28 °C for eight hours and then shifted to 20 °C for 16 hours. Also, the dialysis step for TcdA1 was replaced with an additional ion exchange chromatography on a MonoQ column. For this, elution was performed with a gradient from 0 to 1000 mM NaCl over 50 column volumes. To achieve holotoxin formation, A subunits and BC subunits were mixed in a molar ratio of 5:1 and incubated overnight. Subsequently, the solution was separated using size-exclusion chromatography and pooled according to SDS-PAGE and negative stain images.

All samples were flash frozen and stored until further usage at -80 °.

6.2.14 Cryo-EM grid preparation (PlTcdA1)

4 µl of TcdA1 and its mutants at sufficient concentration were pipetted onto glow-discharged R2/1 Au 200 mesh + 2nm carbon grids (Quantifoil). After incubation of 20 s, excess solution was blotted away, and the grids were plunge frozen in liquid ethane or a liquid ethane/propane mixture using a Vitrobot Mark IV (Thermo Fisher Scientific). The Vitrobot was operated at 12 ° C and 100% humidity, and the samples were blotted for 3 s with a blot force of −1.

6.2.15 Cryo-EM grid screening and data collection (PlTcdA1)

Grids were screened on a 200 kV Talos Arctica Microscope (Thermo Fisher Scientific) equipped with a Falcon III detector (Thermo Fisher Scientific). Typically, low-magnification grid overviews (atlases) were collected using EPU (Thermo Fisher Scientific). The grids that displayed optimal TcdA1 or mutant concentration and distribution were then retrieved from the microscope and stored in auto grid boxes (Thermo Fisher Scientific) in liquid nitrogen until further use for high-resolution data collection.

All datasets were collected on a 300 kV Titan Krios microscope (Thermo Fisher Scientific) equipped with a K3 detector (Gatan) and a postcolumn energy filter (slit width of 20 eV). Videos were obtained in super-resolution mode at a pixel size of 0.44 Å, with no objective aperture inserted. All datasets were collected on the same microscope at the same magnification of 81,000x, to ensure that the resulting cryo-EM density maps could be compared directly without issues caused by pixel size discrepancies.

Using EPU, on average, 20.000 movies per dataset were collected in 60 frames at a total electron exposure of about 70–90 e-Å-2. The defocus values set in EPU ranged from −0.8 to −1.8 µm. The data quality was monitored live during acquisition using TranSPHIRE [125]. If necessary, the microscope was realigned to ensure optimal imaging conditions.

6.2.16 Cryo-EM image processing (PlTcdA1)

For each dataset, video preprocessing was performed on the fly in TranSPHIRE [125]. The super-resolution movies were binned twice (resulting pixel size of 0.88 Å), gain corrected, and motion corrected using UCSF MotionCor2 [126], contrast transfer function (CTF) estimations were performed with CTFFIND 4.13 [127] and TcdA1 toxins were picked using the general model in SPHIRE_crYOLO using a box size of 350 pixels and an overlap of less than 50 pixel [128]. The resulting particles were extracted in a 560 × 560-pixel box using RELION 4.0 and loaded into CRYOSPARC [108, 129]. For each dataset, the particles were two-dimensionally classified using ’2D classification’ [108].

All classes were manually inspected using ‘Select 2D classes’ and those that represented light artifacts and ice contaminations were discarded [108]. The passing particles were subjected to three-dimensional refinement using first ‘ab-initio reconstruction’ to obtain an initial map and then further refined in ‘Non-uniform refinement’ [108, 130]. We refined the TcdA1 or mutant structures with and without applying C5 symmetry. These refinements yielded TcdA1 reconstructions at resolutions of 2.2–4.5 Å. The particles were then converted to be compatible with

Relion, again. Within Relion 4.0, the particles were subjected to Bayesian polishing for improved estimation of particle movement trajectories caused by beam-induced motion [131]; and to CTF refinements to estimate per-particle defocus values and to correct for beam tilt, threefold (trefoil) astigmatism, Cs, and fourfold (tetrafoil) astigmatism and anisotropic magnification.

We then performed three-dimensional classification without image alignment (5 classes, 25 iterations, tau2fudge 4) to remove particles that did not contribute high-resolution information to the reconstruction. Typically, one or two high-resolution classes containing most particles were selected, and the other low-resolution classes were discarded.

Finally, after removal of duplicates, this set of particles was converted back to CRYOSPARC and subjected to a 'local refinement' (focused refinement) [108]. These refinements yielded cryo-EM density maps at resolutions of 2.5–4.0 Å according to the gold-standard FSC = 0.143 criterion. The final maps were sharpened with a negative B-factor. Local-resolution estimations were performed in 'Local resolution' [108].

AlphaFold3 predictions obtained homologous structures based on the sequences used for the MSA, and a homology search was performed using Foldseek [134, 135, 141].

6.2.17 Model building, refinement, and analysis (PlTcdA1)

To build the TcdA1 models in the high-resolution density maps, the structures of TcdA1 in its prepore (PDB 6RW6) were rigid-body fitted into the map of any TcdA1 prepore reconstructions. One single protomer each in the map was then rebuilt manually in Coot, gaps closed, and the other TcdA1 subunits were adjusted in ChimeraX by applying C5 symmetry to the A subunit [136, 137]. The structure was then iteratively refined using Coot (manually), ChimeraX plugin ISOLDE, and phenix real-space refine with non-crystallographic symmetry restraints but without imposing any geometry restraints [132, 136, 138, 139]. Models of all other states were built by rigid-body fitting of the TcdA1 pore structure (PDB 6SUF) in the map, followed by manual adjustments in Coot. These structures were then refined through a similar protocol of iterative cycles in Coot, ISOLDE, and phenix real-space refine. All solvent molecules (water molecules) were placed manually in Coot in the centre of one A subunit and multiplied using C5 symmetry. In cases where reconstructions lacked specific densities present in the original structures, the corresponding residues were removed from the models.

Because the local resolution of each TcdA1 reconstruction is highest in the centre and lower at the periphery of the map, we inspected all water molecules manually before the final phenix

refinement; water molecules with poor corresponding cryo-EM density were removed. All figures and movies that depict cryo-EM density maps and protein structures were prepared in UCSF ChimeraX [136]. Analysis of interaction interfaces was performed using PISA [140].

7 Results and Discussion

The work described in this section was carried out in collaboration with Dr. P. Ng'Ang'A. Generation of mutants, their purification, pore formation analysis, and optimization of plunging conditions were, in general, performed by Dr. P. Ng'Ang'A with assistance from Dr. D. Roderer. Cloning, purification, and negative stain analysis of E1786A and E2111A, as well as all work related to data processing, model building, and analysis, were carried out by me. Dr. D. Prumbaum, Dr. O. Hofnagel, and Dr. P. Ng'Ang'A performed the SPA data acquisitions. The generation of HVR mutants, purification, and pore formation analysis were carried out together with Dr. P. Ng'Ang'a.

7.1 Structural investigation of Tc toxin shell and pore opening

To adapt Tc toxins successfully for other applications, such as biopesticides, it is essential to understand the entire mechanism of recognition, entry into cells, pore formation, and toxin release in detail. Although a number of these questions have already been answered for Tc toxins from *Photorhabdus luminescens*, especially TcdA1, one of the most critical remaining questions is how shell opening and subsequent pore formation are facilitated.

As previously mentioned, recent studies were already able to identify intermediate states between prepore and pore state of the toxin, suggesting that the system relies on multiple steps to form a pore, however the life time of most of these intermediate states was too low to allow for structural determination and prevented mechanistic insights [90].

7.1.1 Conserved molecular latches and internal forces

To identify the distinct steps, we sought to compare the shared structural features of Tc toxins across the species. The assumed generally applicable mechanism is likely conserved on a sequential level, providing starting points. To this end, we performed a BLAST search with the TcdA1 sequence to identify similar sequences outside of the *Photorhabdus* family. In total, we selected 16 sequences with sequence lengths between 2000 and 2600 amino acids and performed a multiple sequence alignment (MSA) with these 17 proteins (Figure S1).

Since high-resolution prepore structures of *Yersinia pseudotuberculosis* (PDB code: 6RWB), *Morganella morganii* (PDB code: 6RW9) and *Xenorhabdus nematophila* (PDB code: 6RW8) have already been resolved and therefore provide reliable structural information as well, they were included in the selection [75]. Overall, the sequences share only ~ 30% sequence identity;

however, this appears to be sufficient to provide a conserved architecture, as indicated by the predicted AlphaFold structures (Figure S2).

Since *in vitro* experiments suggest a pH sensitivity of the toxin concerning its conformational changes, we analysed the resulting alignment for conserved residues. Hence, especially salt bridge-forming residues (e.g., arginine, aspartic acid, glutamic acid, and lysine) were the primary focus of the MSA analyses (Figure S1).

Comparing these hits with either pre- or pore-state structures of the known models allowed us to filter the list down to those that are close enough to form potential salt bridges (<5 Å distance) and select candidates for experimental investigation (Figure 12A). Interestingly, two of the identified interactions (E158-R1873 and E1086-R1166, Figure 12A) were previously highlighted due to their effect on the stability of the prepore state [75].

To analyze these interfaces in detail, we mutated the acidic residues to alanine, which is supposed to interrupt the interfaces. One mutation (E1086A-R1166) showed an increased number of pores during negative stain analysis (Figure 13E), compared to the WT, while the other (E158A-R1873) was comparable to the WT. Expanding the focus to the other MSA-based hits, we can show that interrupting E1786-R2186 and E2111-R2187 significantly destabilizes the prepore state and leads to almost 100% pore formation without changing the pH (Figure 13E).

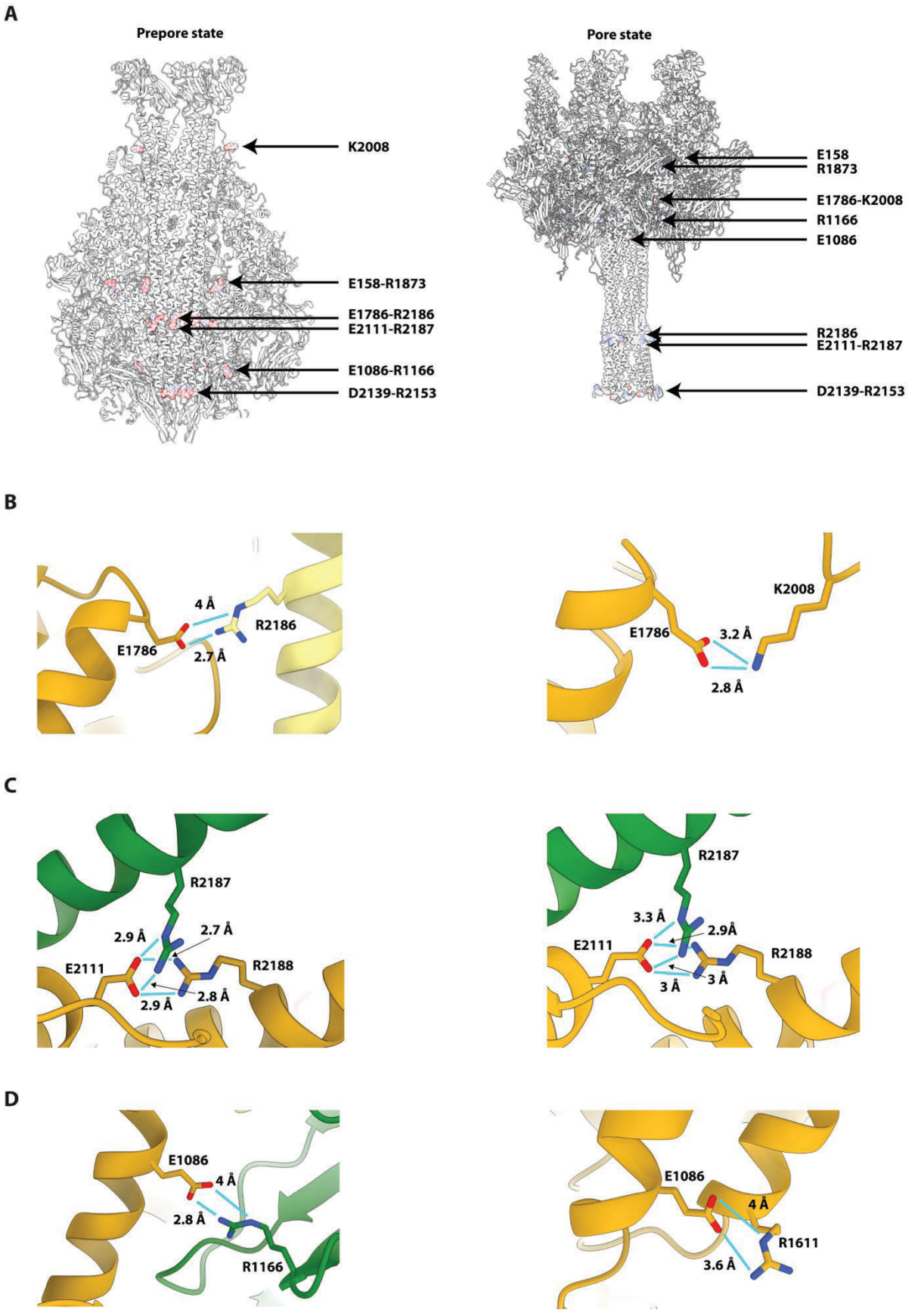

Figure 12: TcdA1 prepore and pore structure with exemplary latches as zoom-ins

(A) Cartoon representation of TcdA1 prepore (left) and pore (right) state highlighting the position of some exemplary latches identified. (B-D) Zoomed-in representations of latch interfaces in prepore (left) and pore state (right) labeled by chain color with the corresponding residue name and the interaction length. Notably, in B and D, the interface changes from inter-protomeric to intra-protomeric.

Initially, we anticipated problems during the expression and purification of these mutants, as E2111-R2187 forms inter-protein interactions between the chains that assemble the channel. Furthermore, E1786-R2186 directly links the channel to the outer shell, and more specifically to the small lobe, which connects the stretched linker to the neuraminidase domain. However, while the purification of mutant E1086A, E1786A, and E2111A seemed to indicate slight aggregation during the size-exclusion chromatography (~ 45 ml elution volume in Figure 13A and C), the actual protein peak at ~ 60 ml elution volume seemed to be stable in SDS-PAGE analysis (Figure 13B and D). It was later confirmed by the ordered toxin classes in negative stain analysis (Figure 13E). While we could observe 100 % pore formation for E1786A & E2111A (Figure 13E bottom), the results for E1086A showed a mixture of states as described previously.

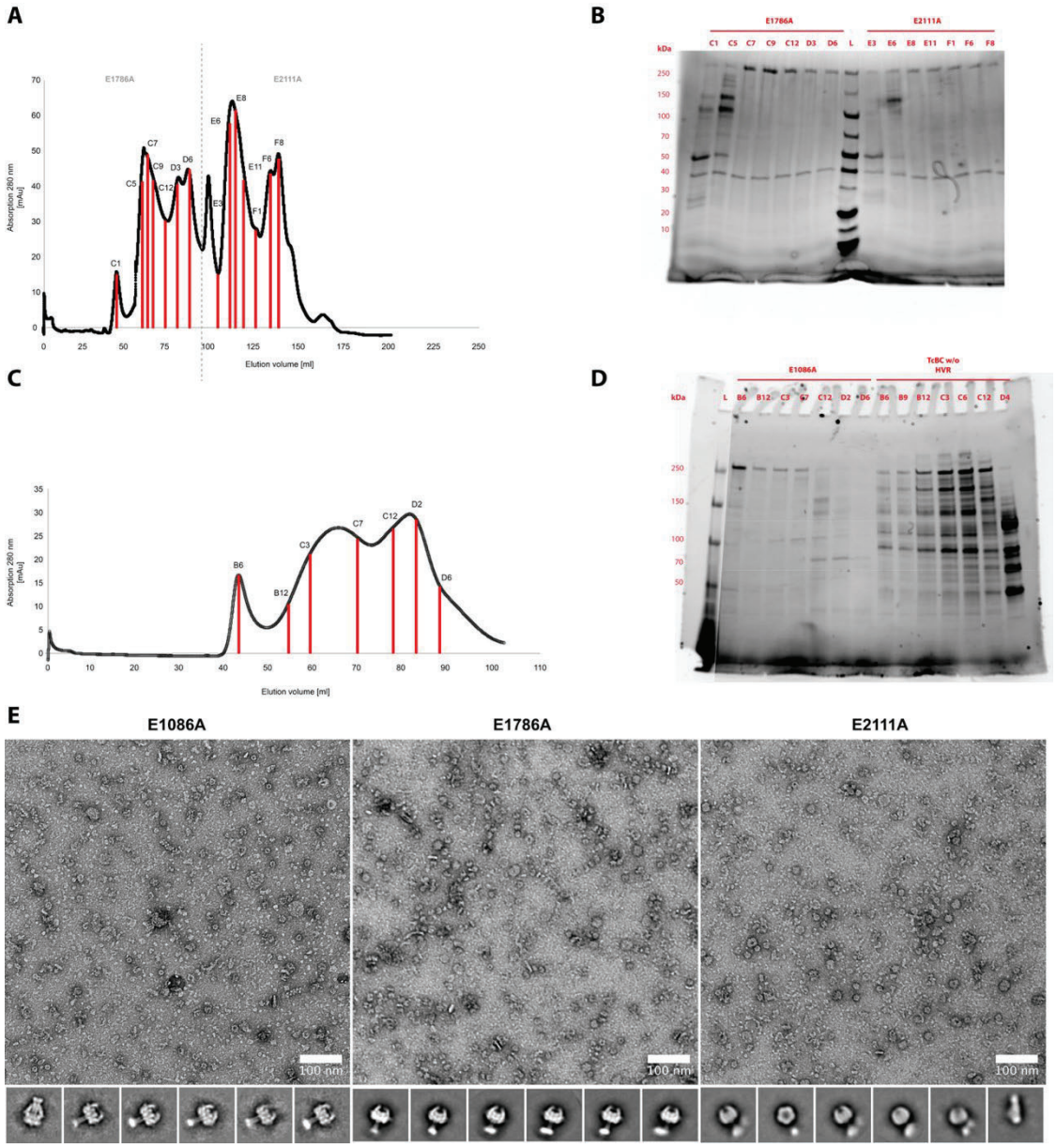

Figure 13: Overview of E1086A, E1786A and E2111A purification and the resulting negative stain images
(A) Plot of a size exclusion chromatogram for the purification of TcdA1 mutants E1786A (left half) and E2111A (right half) with red bar representing the samples chosen to be checked with SDS-PAGE in (B). (C) represents the plot for E1086A purification and was controlled in the left half of (D). In all cases, samples from the second peak (~ 60-65 ml elution volume) were pooled and analyzed by negative stain EM. Exemplary images are shown here (E).

Notably, the E1786-R2186 interaction was previously considered less crucial for pore formation, as Y. pseudotuberculosis contains an aspartate at position 2186 instead of the arginine. However, the interface at this position is still maintained for *Y. pseudotuberculosis* because a nearby residue is mutated to an arginine, which increases the impact of this interface as it also forms contact with the mutated aspartate.

Another potentially crucial interaction site is formed by D2139-R2153, which is located at the tip of the channel and, therefore, is most likely to help keep it closed. Destabilizing this salt bridge would potentially result in a flexible tip.

Lastly, we also noted that changes in interaction partners might be a crucial part of the pre-pore transition. After transition, E1786 likely forms a salt bridge with K2008 (Figure 12B, right), which is unexpected because studies by Dr. P. Ng'ang'a have shown that a K2008A mutation impedes pore formation. This is surprising, as in its prepore state, K2008 is part of the C-terminal end of the stretched linker and points into the solvent; therefore, the alanine mutant was supposed not to affect the arrangement too drastically. Knowing that K2008 serves as a potential stabiliser for E1786 alters that assumption (Figure 12B, right). Usually, salt bridges based on arginine are considered inert to physiological pH changes due to the pKa of ~ 12.

However, our collaborators were able to demonstrate, using pKa shift analysis and MD simulation, that these interactions could still be altered under physiological conditions if either the electric potential changes drastically (resulting in more ions and/or lipids) or donors and acceptors can swap their partners in a dynamic environment. This suggests that K2008 has an essential role in the pore-pore transition, as it may provide such an option for E1786 upon rearrangement and would explain why pore formation is completely abolished upon mutation to alanine. However, other factors must also be taken into consideration.

The inter-protomeric E2111-R2187 (Figure 12C left) interaction is interesting for two reasons: it involves two of the four poly-arginine (R2186-R2189) residues and forms an intra-protomeric interaction with R2188. Additionally, its location is noteworthy. As previously reported, this interaction is directly positioned around the hinge region of the channel, which is responsible for mediating the channel's opening. Most likely, the extreme phenotype we observe with the E2111A mutant is a response to the removal of attractive forces (salt bridges and hydrogen bonds are energetically favourable) and results in stronger repulsive forces between the arginine head groups.

Seemingly, these interactions are strong enough to induce pore formation, which further supports the concept of a system that is driven by an equilibrium of attractive and repulsive forces.

The primary function of E1086-R1166 (Figure 12D, left) appears to be cross-connecting the outer shell between different protomers, thereby helping to maintain the prepore state. During the transition, the interaction shifts to an intra-protomeric interface between E1086 and R1611 (Figure 12D, right), arguably favouring the equilibrium towards pore formation. E158-R1873 follows not only the pattern of E1086-R1166 in connecting neighbouring chains and transitioning into an intra-protomeric chain, as seen in E158-K982, but also directly anchors the linker

domain of the trefoil knot to the outer shell, thereby helping to stabilize the prepore arrangement.

Since most of the identified interactions seem to be based on conserved arginine-mediated interactions, the postulated idea of electrostatic latches appears to hold [75]. This was further supported by an observation first noted in MD simulations on the HVR. These analyses suggested that upon pH changes, the HVR within the toxin tends to shift position while still in the prepore state.

We hypothesize that due to the overall positive charge of the HVR, it would translocate into the channel towards a more favourable environment. This would also be in line with the observation published for HVR modification, which indicates that only cargoes with a pI close to 9 are properly translocated [89]. Furthermore, this could be a potential reason for how the internal latches might be initiated to change their interaction partners. The translocation of the HVR from the cocoon to the channel could not only cause conformational changes due to steric reasons but also alter the electric potential around the latches, resulting in changes within the system. To study this hypothesis in vitro, we generated mutant versions of the HVR in which we, starting from the C-terminus, replaced positively charged residues with neutral ones. After expression and purification, we first analyzed their pore formation ratio in comparison to WT holotoxins and observed a decreased pore formation capability in the mutants (Figure 14A).

After confirming the general functionality of the mutated toxic enzymes with Dr. P. Ng'ang'a, we collected a high-resolution dataset of mutant2 (H2415A, K2432A, K2435A, H2437A, K2438A, R2439A) attached to WT TcdA1. The resulting structures of the holotoxin were determined to be ~ 2.4 Å for the prepore and ~ 3 Å for the pore state. This, in turn, allowed us to compare the low-resolution reconstructions that would correspond to the HVR with WT holotoxin as described in [76]. Following in line with our initial assumption, indeed, the density corresponding to mut2 HVR in the preprotein state seems to be restrained to the cocoon compared to the WT, where the density also protrudes into the channel area (Figure 14B).

This is even more striking when comparing the two pore state reconstructions. Although there is no density left for WT HVR because the toxic enzyme has already been ejected (Figure 14C), the mut2 HVR still appears to reside mainly in the cocoon area. Together with the functionality assay, these results indeed suggest that the overall charge of the HVR is crucial for its translocation into the channel and connect this translocation with pore formation. Whereas there is still a small fraction of formed pores in the mut2 dataset (Figure 14A), the amount has decreased by five- to six-fold compared to WT.

This would indeed be one of the few (if not only) known toxins in which the internal cargo and its associated forces have direct effects on the overall function, and once more highlight the high degree of complexity behind the Tc toxins.

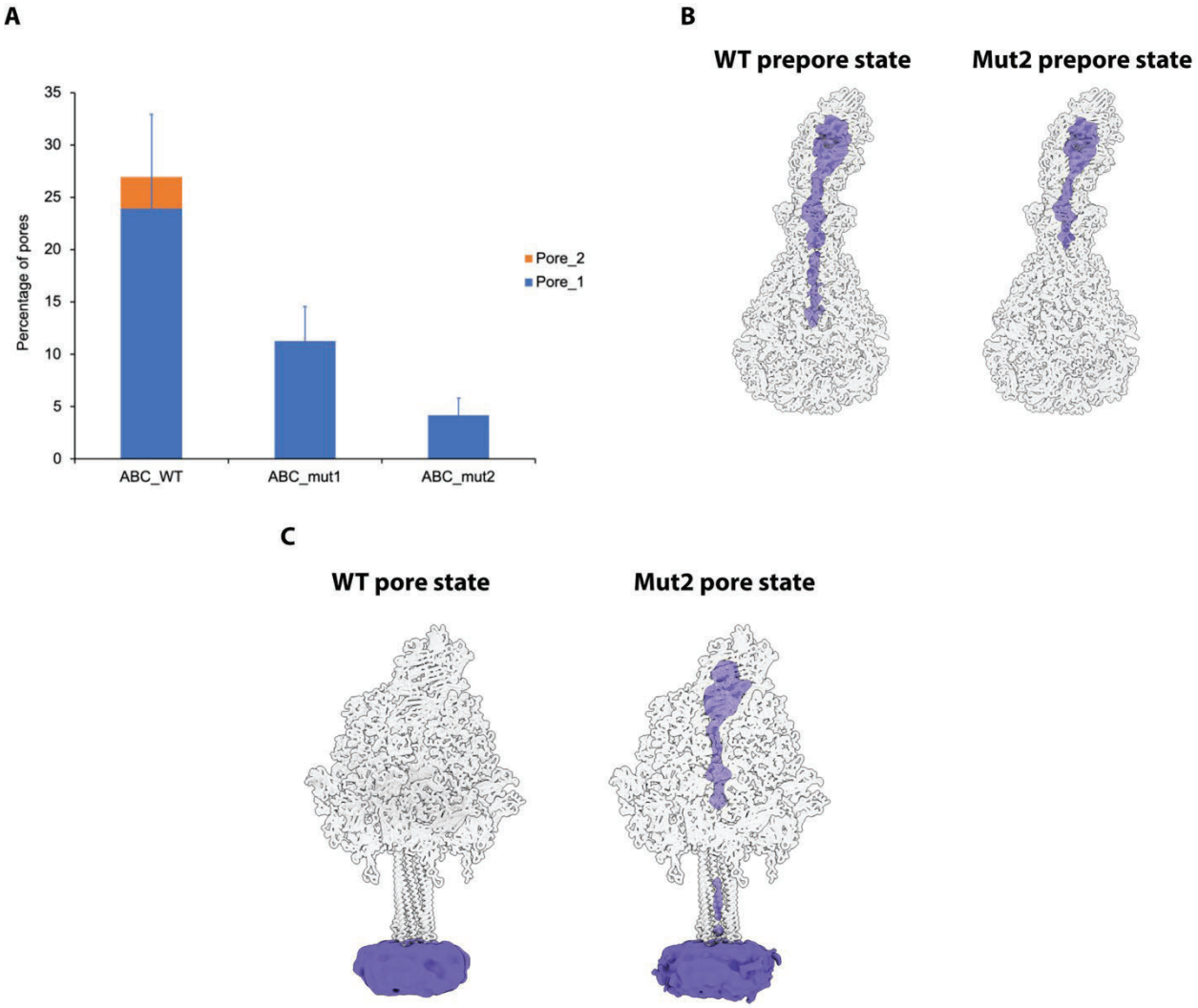

Figure 14: Overall charges on HVR influence translocation and pore formation
(A) Plot of pore formation behaviors of WT holotoxin and HVR mutants 1 and 2 based on negative stain EM analysis. Pore2 refers to inverted pores (B-C). Cartoon representations of prepore (B) and pore (C) structures highlight the corresponding densities for the HVR reconstructions in blue for WT holotoxin and HVR mutant 2.

7.1.2 Attraction-repulsion forces mediate pore formation

To better understand the concept of internal forces in the channel area and identify further key sites, we also turned to established Tc toxin mutants. Since the lower part of the actual channel displays a hydrophobic interface (later on used to insert into the membranes), the idea arose that swapping the hydrophobic part of the channel to a more hydrophilic one might induce flexibility in the system and subsequently cause the channel and the tip to open up. This potentially would allow for easier pore formation with little to no external factors being necessary, and hence enable the trapping of intermediate steps.

These steps, as previously described, include the flip-out of the RBDs and the opening of the neuraminidase domain (Figure 15). To follow up on this idea, multiple Tc toxin mutants were generated (by Dr. P. Ng'Ang'A and Dr. D. Roderer) to investigate this in detail. Two of the most promising constructs, QT (D1193C, L2133Q, I2157T, V2164T, V2171T, L2140Q, V2141T, I2144T) and QT-K1179W (D1193C, K1179W, L2133Q, I2157T, V2164T, V2171T, L2140Q, V2141T, I2144T) displayed opposing behaviours where the first showed an increased pore formation (even at acidic pH levels) and the latter abolished pore formation.

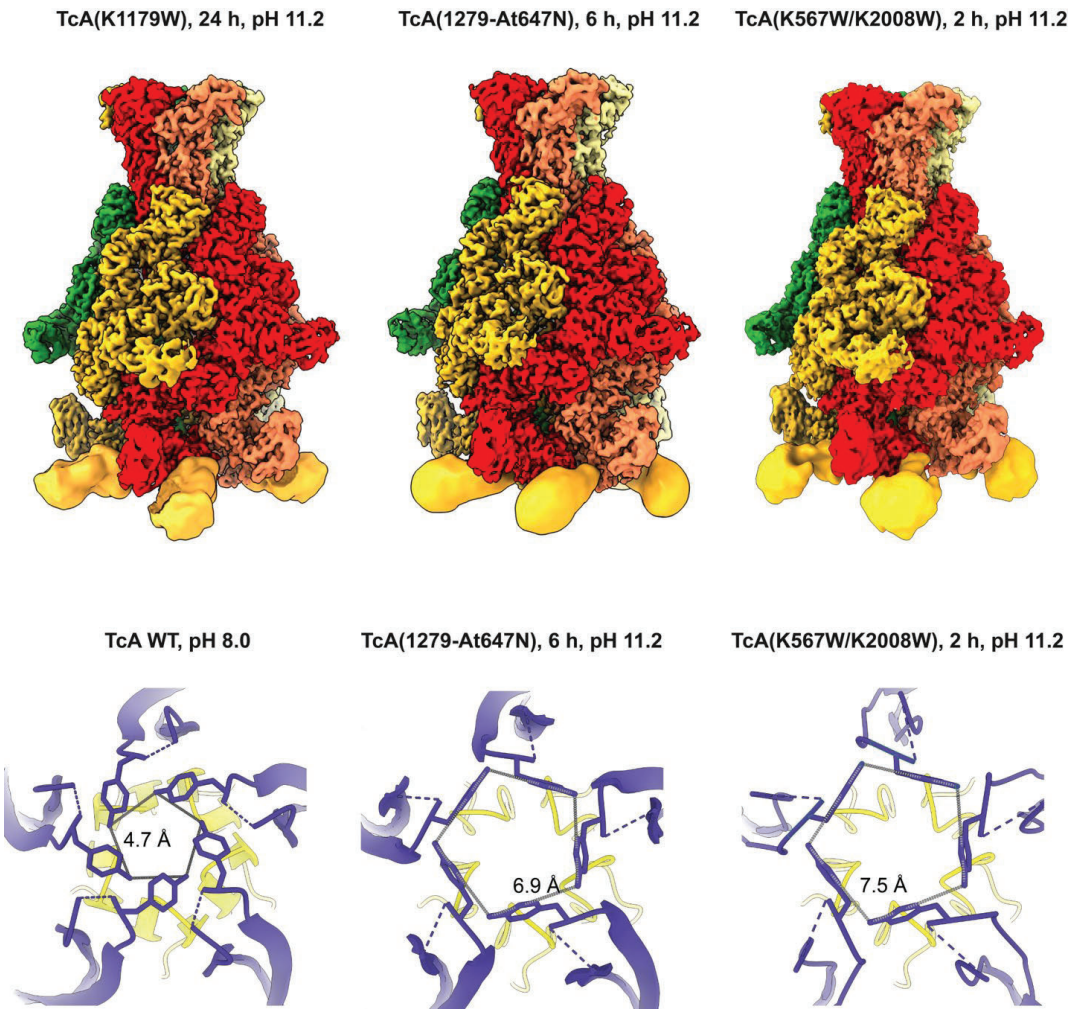

Figure 15: Structural rearrangements during prepore-pore transition at different pH and incubation times
(Top panel) From left to right: High-resolution cryo-EM maps for TcA stable intermediate mutants K1179W,1279-At647N, as well as K567W/K2008W incubated at pH 11.2 for 24,6 and 2 h, respectively. The low-resolution reconstructions of flipped-out RBDs at the bottom of the A component were attached and are colored yellow. (Bottom panel) From left to right: Zoom-ins on the bottom perspective of the neuraminidase domain for TcA WT and mutants 1279-At647N, as well as K567W/K2008W, highlighting the spatial size increase between WT and the mutants, indicating a slow opening of the neuraminidase domain in the process. Figure adapted from [90].

To fully comprehend the differences between the mutants and their implications in the pore-forming mechanism, we determined the prepore structures of TcdA1 WT to 2.31 Å, TcdA1 QT to 2.18 Å, and TcdA1 QT-K1179W to 2.35 Å and 2.4 Å. The latter one displayed two distinct classes, which we could separate using extensive 3D classifications. Overall, all four structures resembled the classical architecture of the prehistoric state as described in 4.4.

The most notable differences were identified at the bottom part of the toxin (Figure 16). Whereas the outer shell of the WT toxin forms a neuraminidase-like domain at the bottom to lock the channel in place, for the QT construct, the region of aa 2126-2167 could not be modelled due to a lack of density. Furthermore, the QT model also lacked density for the bottom of the channel (aa 1176-1193), indicating a high degree of structural flexibility in this area, which also could not be resolved by local resolution 3D reconstruction or 3D flexibility analysis.

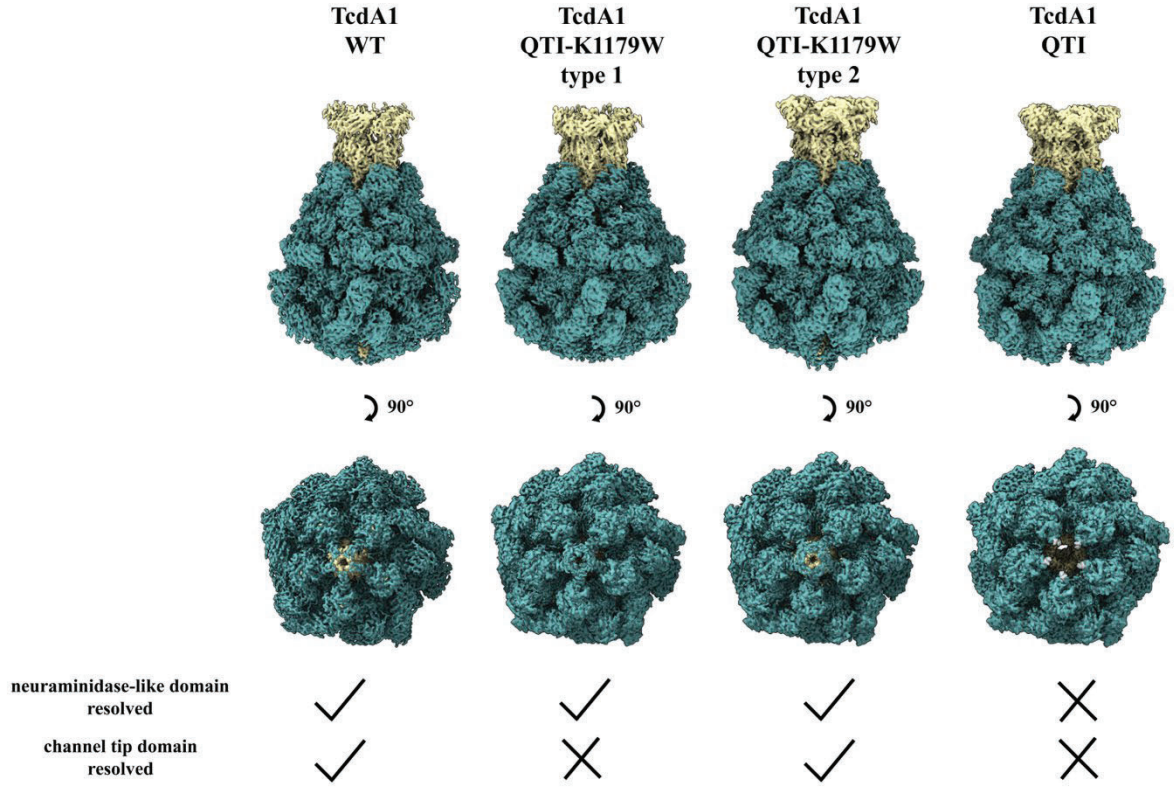

Figure 16: Comparison of prepore states of TcdA1 WT, QT-K1179W (type 1), QT-K1179W (type 2), and QT
Side (top panel) and bottom (lower panel) view of the cryo-EM reconstructions of TcdA1 WT, QT-K1179W (type 1), QT-K1179W (type 2), and QT coloured in green (outer shell) and yellow (channel region). Presence (ticks) or absence (crosses) of the neuraminidase domain or the channel tip domain are indicated accordingly.

Surprisingly, the QT-K1179W mutant reconstructed into two distinct types: one (~ 70 % of particles) displayed density for the neuraminidase-like domain but not the inner channel, while the other (~ 30 % of particles) showed apparent density for both. This was unexpected to us since we would have expected a more stable pre-existing structure, and could only be explained by comparison. Whereas the WT neuraminidase domain closes the outer shell in a flower bud-like arrangement, the K1179W mutation (which we assume to be the cause for it since we cannot observe this behaviour for the QT mutant) seems to tilt the tip into a more iris-like arrangement increasing the intra-protomer interactions and therefore stabilizing the entire arrangement.

One reason we cannot resolve these areas might be due to the flexibility induced by the change from a hydrophobic interface to a hydrophilic one, which subsequently causes the channel and the tip to open, resulting in blurred reconstructions. However, in the case of QT-K1179W, the additional mutation provides the outer shell with enough ‘strength’ to stay in its closed conformation. However, the flexibility induced within is still substantial enough to prevent proper resolution of the channel tip for most particles.

Using flexibility analysis [133], we could also observe that a probable repulsive force between the channel tip and the interior of the neuraminidase-like domain at the bottom leads to flexibility of the entire channel, forcing it to shift upwards. This data suggests that the Tc toxin outer shell directly controls pore formation by the likelihood of opening the neuraminidase-like domain. Indeed, this is in line with the recently published intermediate structures of pore formation, which showed flipped-out RBDs and a slightly opened neuraminidase-like domain (Figure 15). These structures suggest that increased flexibility at the bottom of the shell, in part due to the flexibility of the flipped-out RBDs, might constitute the first step(s) towards pore formation. Together with the previously discussed internal forces, these factors might determine the pore formation.

7.1.3 Concluding discussion

In contrast to the so far assumed passivity of the effector release being mainly driven by diffusion into the cytosol or by pulling of recruited chaperones, our results indicate a third option in which, like a torpedo, the lethal cargo is released by an internal pressure induced as a response to pH changes. This concept would not just put the effector into a more active role concerning translocation but also allow it to mediate pore formation itself. Although it is unlikely to function independently, it adds an additional layer of regulation to this complex system.

Notably, our MD simulations suggest that an increased force is created in both alkaline and acidic environments. This indicates a similar behaviour concerning pore formation, which, however, we are unable to induce at acidic pH *in vitro*. This is especially surprising since Tc toxins, which are not being secreted into the insecticidal midgut, are very unlikely to encounter alkaline pH ranges but are supposedly exposed to acidic pH during endosomal maturation.

One potential explanation for this behaviour might be related to the electric potential associated with it. While our *in vitro* acidic pH setup does not allow for changes in ionic composition, the process of endosomal maturation is accompanied by a significant variation in the ionic composition due to different ions being pumped into and out of the endosomal vesicles.

In contrast, the alkaline pH buffer setup is based on the zwitterionic buffer molecule CAPS, which may alter the local electric potential and thereby facilitate pore formation. Our initial attempts to mimic an endosomal-like system in terms of ionic composition have been unsuccessful so far, which may be related to the non-physiological setup. Alternatively, an additional component may be necessary to achieve pore formation at acidic pH, e.g., protease-dependent activation, as is commonly used in other infection pathways. Previous studies suggest that cleavage of the solvent accessible N-terminus of TcdA1 favours pore formation by weakening the trefoil knot architecture [81]. However, in our hands the usage of high concentrations of commonly used protease inhibitor cocktails (cOmplete, PMSF) did not affect Tc toxicity on HEK cells (Figure 17), suggesting that either protease activation is not necessary for its toxicity or that an uncommon protease is responsible which is not affected by the inhibitor cocktails. The supplier reported successful usage for other endocytosis control experiments.

In line with previous publications, the proposed transitional mechanisms rely on salt bridge-mediated interactions; however, in contrast to just one or two crucial ones, our data suggest a highly conserved network that follows the proposed concept of latches. This high number of molecular switches also ensures that pore transition is not merely induced by slight changes in pH, electric potential, or chance, but only when all the right conditions are met.

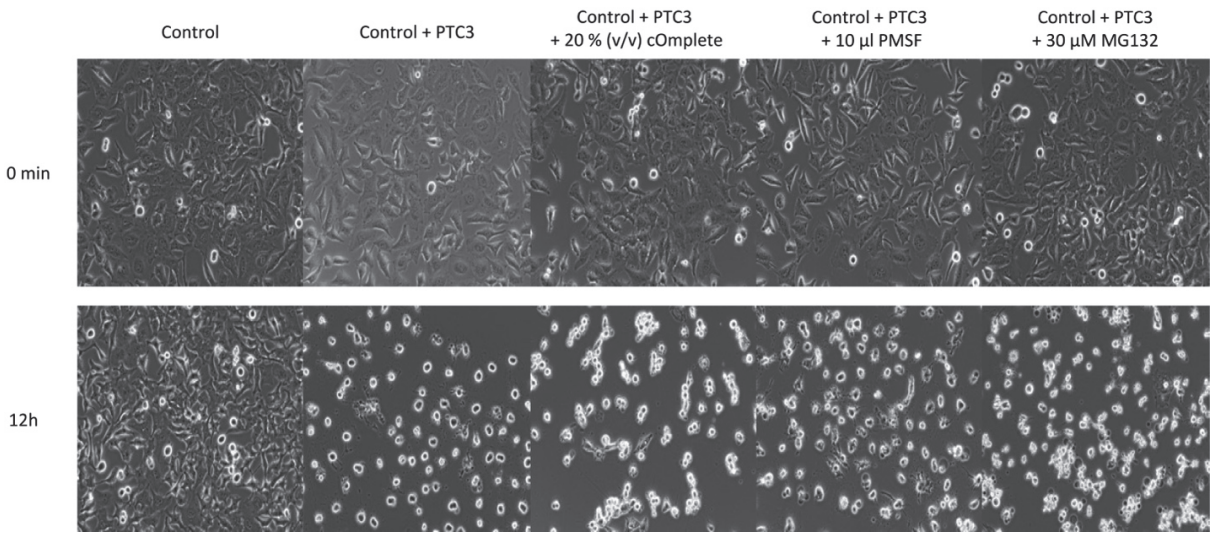

Figure 17: Toxicity assay for PTC3 in the presence or absence of protease inhibitors
(From left to right) HeLa cells were incubated for 0 min (top) and 12h (bottom) in either the absence(left) or the presence of 1 nM PTC3 (second from left), together with cOmplete protease cocktail (middle), PMSF (second from right), and MG132(right).

This serves as an ingenious fail-safe mechanism and is very likely true for all toxins analysed in this study. Although some species occasionally diverge from the general trend, such as *Yersinia pseudotuberculosis*'s Tc toxin, the general interaction interface is maintained by point mutations nearby, as previously explained. The high conservation level, on the one hand, underscores its importance, and on the other, also highlights that biological complexes are more diverse than biophysical studies of single amino acid interactions in solution might suggest, indicating an almost enzymatic arrangement.

This study lays the foundation for several follow-up studies: One of them is to experimentally analyse whether the identified molecular latches must be opened in a precise order, e.g. from bottom to top, or whether just a random number of switches need to be turned to facilitate it, potentially also in respect to interactions with the HVR. This could also provide novel insights for a potential translational usage of Tc toxins.

Furthermore, capturing high-resolution intermediate states of Tc toxins as they transition towards pore states could help evaluate the concepts of pore formation in both alkaline and acidic pH environments. Lastly, the effects of different pentamers combined with HVRs can be tested and analysed to broaden the understanding of their versatility.

All in all, our results suggest a general, applicable mechanism for alkaline pH ranges, in which a layered arrangement of molecular switches must be activated to facilitate the Tc toxin transi-

tion. The interplay of an inward-outward force caused by the HVR, changes in electric potential, primarily due to variations in ion concentrations, as well as the switching of molecular latches, mainly salt bridges, enables a precisely regulated and still versatile transition mechanism.

We therefore expect this knowledge to not only fuel new research concerning Tc toxins but also pave the way for translational research that employs the entire arsenal of Tc toxins.

7.2 Split-shell Tc toxins operate via several novel conformational states

The work described in this section was carried out in collaboration with Dr. O. Sitsel. Gene editing of *Yersinia entomophaga* and *Yersinia pseudotuberculosis* strains was performed by Dr. O. Sitsel with help from D. Obergfäll, Dr. P. Günther, L. Kerkmann and L. Kroczek. The optimization of the purification protocol and plunging conditions was performed together with Dr. O. Sitsel. The SPA data acquisitions were performed by Dr. D. Prumbaum, Dr. O. Hofnagel, myself, and Dr. O. Sitsel. I carried out all work related to data processing, model building and analysis.

Initially, the Tc toxin produced by *Yersinia entomophaga* raised scientific interest because although being a functional toxin [73] it could not be used to kill standard cell culture cell lines (Figure S 2) suggesting a high degree of specificity in respect to the target recognition, like the grass grub larvae of *Costelytra zealandica*. Earlier attempts to understand this specificity on a mechanistic level failed due to insufficient structural information and suboptimal purification methods, which employed ammonium sulfate precipitation [79]. This procedure can lead to a change in pH or make proteins insoluble, affecting the protein and subsequently the reconstruction quality.

Due to the identification of a novel secretion pathway [24] and genetic modification of the native organism (performed by O. Sitsel), we were able to overcome these challenges and optimize the purification protocol to avoid the previous limitations. We purified the A component and the B and C2 component separately to ensure a homogeneous complex consisting of identical subunits, allowing for high-resolution reconstructions. Hereafter, we generated holotoxins *in vitro* and prepared vitrified samples, which paved the way for a detailed analysis by cryo-EM.

7.2.1 YenTc split-A architecture resembles the conserved Tc toxin fold

To uncover the general fold of the YenTc prepore, we generated holotoxins in the prepore state as described in chapter 6.2. This sample preparation protocol enabled us to determine a preformed structure at a resolution of 2.6 Å (Figure 18, top panel and Figure S4) and to analyze the Tc toxin fold in molecular detail.

The structure reveals a conserved bell-shaped pentamer formed by YenA1, which forms the outer shell, and YenA2, which creates the inner part, including the channel. As previously mentioned, the RBDs from *Photorhabdus luminescens* are replaced by chitinases that are associated

with YenA1 in the case of Chi2 and YenA2 for Chi1. The B and C components form the conserved cocoon-like arrangement on top of the pentamer (Figure 18A).

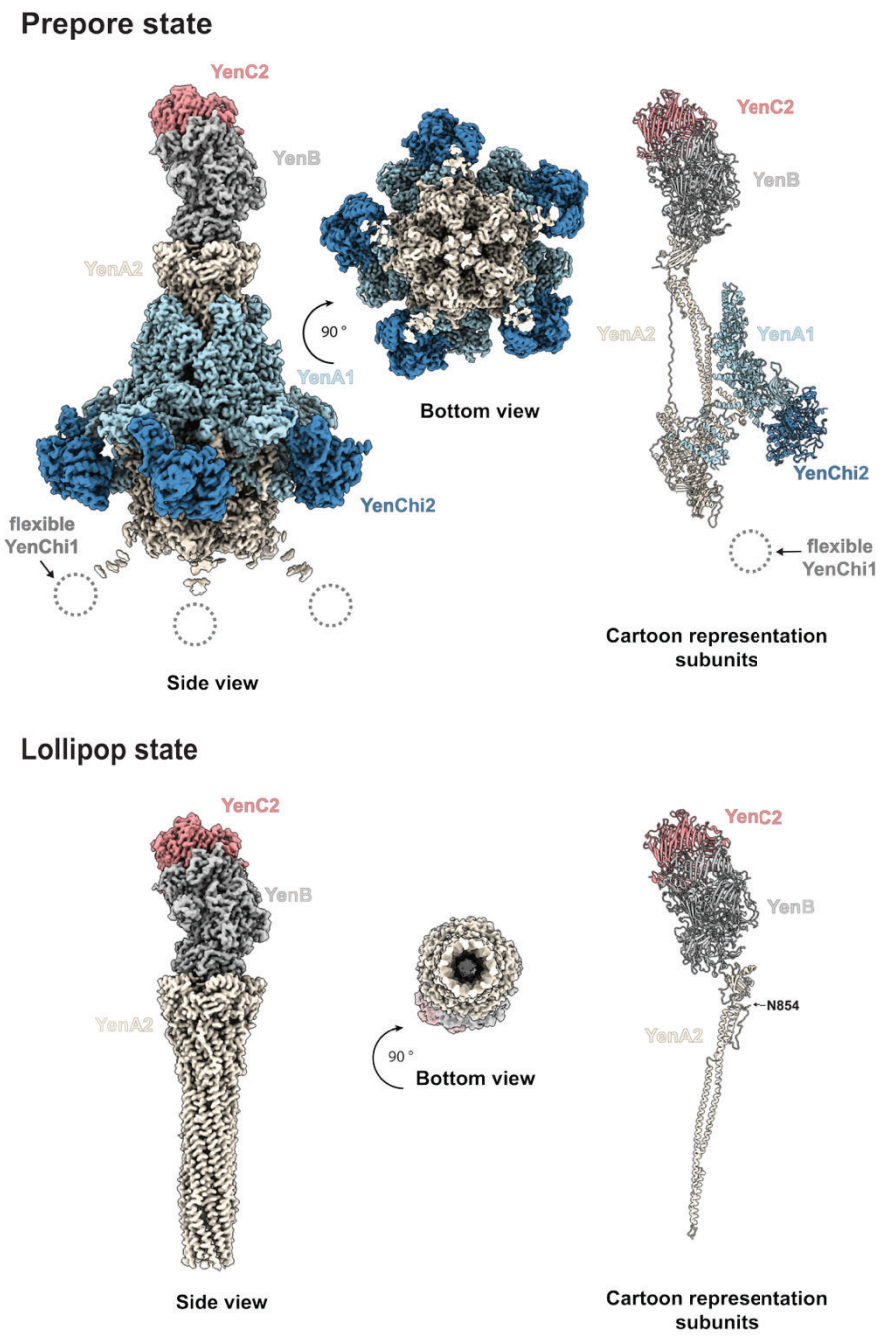

Figure 18: General architecture of YenTc prepore and lollipop state
Composite cryo-EM maps (bottom and side view) and architectural model of YenTc prepore (top), Lollipop state (bottom), Neutral pore (C) as well as alternate pore state (D) colored according to the corresponding subunits (YenA1 in light blue, YenA2 in beige, YenChi2 in dark blue, YenB in gray and YenC2 in red). Note: The additional subunit Chi1 could not be resolved in a regular cryo-EM reconstruction but would be attached to the protrusions of YenA2 visible in the top panel (exemplified as dashed circles). The outer shell (mainly YenA1 and YenChi2) of YenTc lollipop is dissociated, subsequently inducing a high degree of flexibility for the YenA2 N-terminus, preventing any model building before amino acid number 854.

The high-resolution structure and resulting model not only allowed us to trace the protein chains more accurately compared to Piper, S. et. al. (2019), but also to fill in essential gaps (Figure

19) [79]. So far, the prepore model consisted of homology models docked into the density, which did not allow for modelling of the actual interface of Chitinases 2 (Chi2) with the A component (YenA1 and YenA2) (Figure 19A). With the new high-resolution reconstruction in hand, we were able to identify a previously unknown handshake-like motif formed by YenA1 with the N-terminus of Chi2, keeping it attached to the outer shell of the toxin (Figure 19 B and C). This motif is formed by aa 1-25 of Chi2 and aa 380-420 from YenA1, resulting in extended loop regions that intertwine in a handshake-like fashion and are locked into place by the intercalation of the loop tips with the countering structure. Furthermore, Chi2 forms an interface with the N-terminal part of YenA1, keeping it—and the trefoil knot formed from it—from being solvent-exposed.

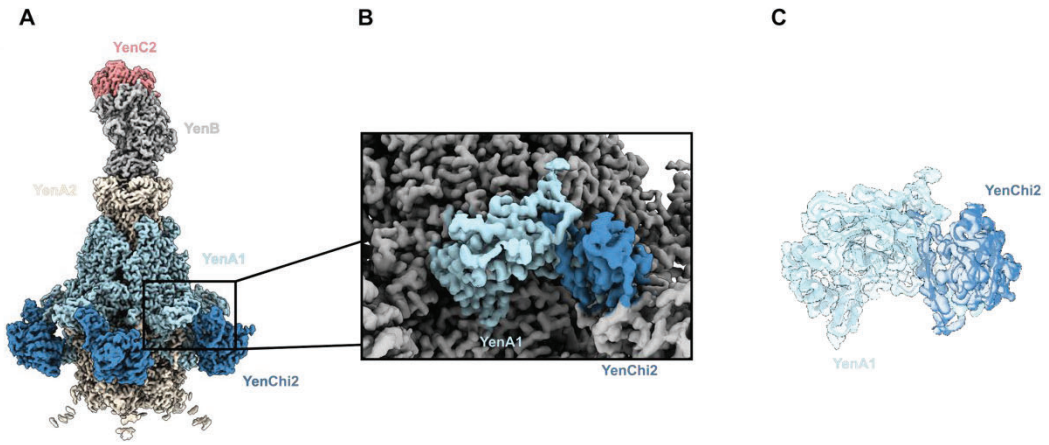

Figure 19: YenA1 and YenChi2 form handshake like interaction
(A) Cryo-EM map of the YenTc prepore state colored according to the individual components. (B) Zoomed-in representation of the connection between YenA1 and YenChi2, which could not be modeled in previous attempts. (C) Local density representation of the handshake-like arrangement of YenA1 and YenChi2 with its structure model.

The other chitinase, Chi1, always proved to be challenging to model due to a high degree of inherent flexibility [79]. Additionally, in our hands, the initial reconstructions did not allow for modelling (Figure 18A, dotted spheres); however, after extensive 3D Variability and 3D Flex analysis [130, 138], we were able to obtain a reconstruction that enabled docking of AlphaFold2 predictions [142] (Figure 20). Thus, also allowing us to understand the so far undescribed architecture of the bottom region of the holotoxin.

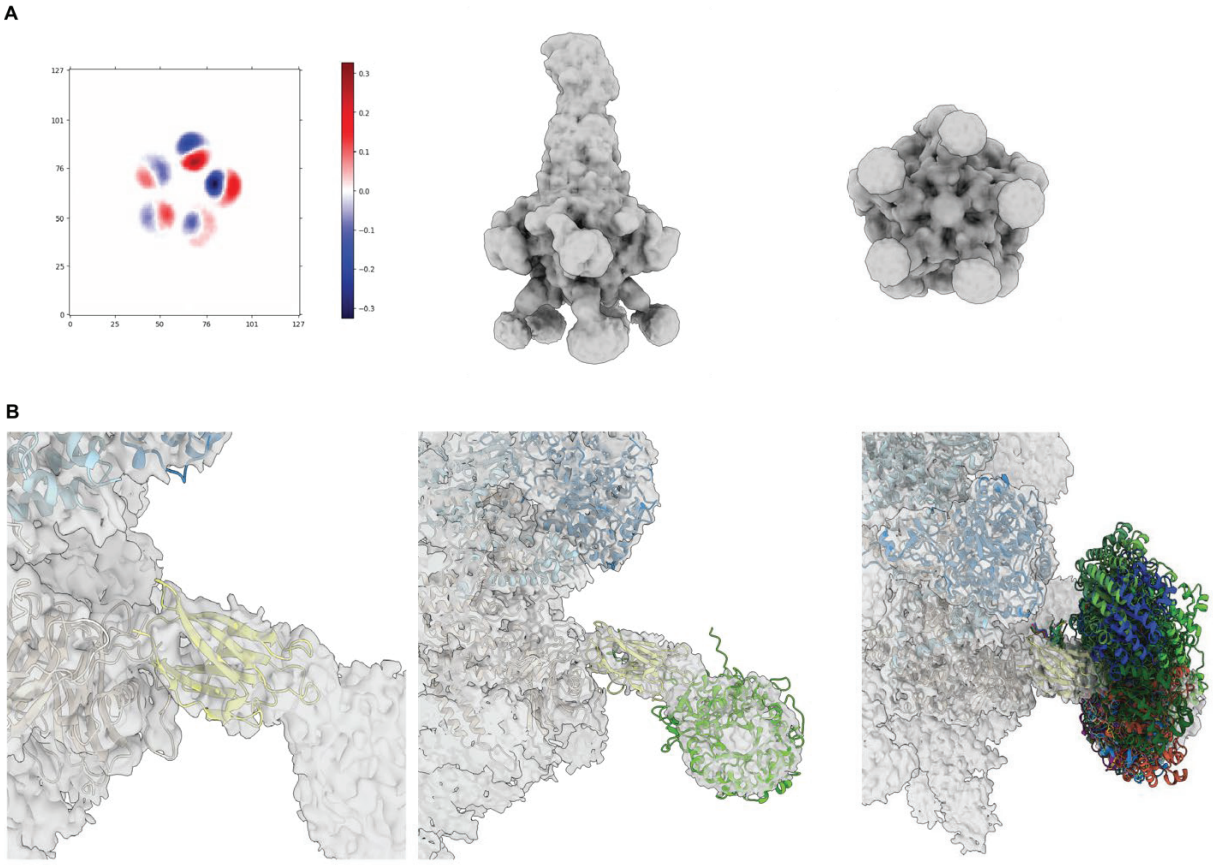

Figure 20: Flexibility is key for Chi1
(**A**) PCA representation of Chi1 localization in YenTc prepore state (left panel; red areas indicate an underrepresentation and blue one an overrepresentation of Chi1 in the colored region) underlining Chi1's flexibility. Side (middle panel) and bottom (right panel) perspectives of corresponding cryo-EM reconstructions depicting a smeared-out density for YenChi1.
(**B**) Local refinement representation of YenTc prepore focused on the bridging region towards Chi1 with a docked AlphaFold2 prediction in yellow (left panel). The central panel represents the highest-ranked AlphaFold2 multimer prediction (green) interacting with the connection part (yellow). All AlphaFold2 multimer predictions docked into the density in the right panel, notably further highlighting the degree of flexibility.

Additionally, we were able to build the entire BC component, except the proteolytically cleaved C-terminus of C (Figure 18A), which provided us with new insights into the overall arrangement of YenTc. The interface strength of YenA2 and B is severely decreased due to the smaller interaction interface of the BC cocoon with the funnel region of YenA2 (Figure 21), which explains the previously observed affinity measurements. This interface reduction is caused by an increased diameter of the A component funnel, which prevents some interactions from being formed that are present in the TcdA1 holotoxin (Figure 21B, Table 2)

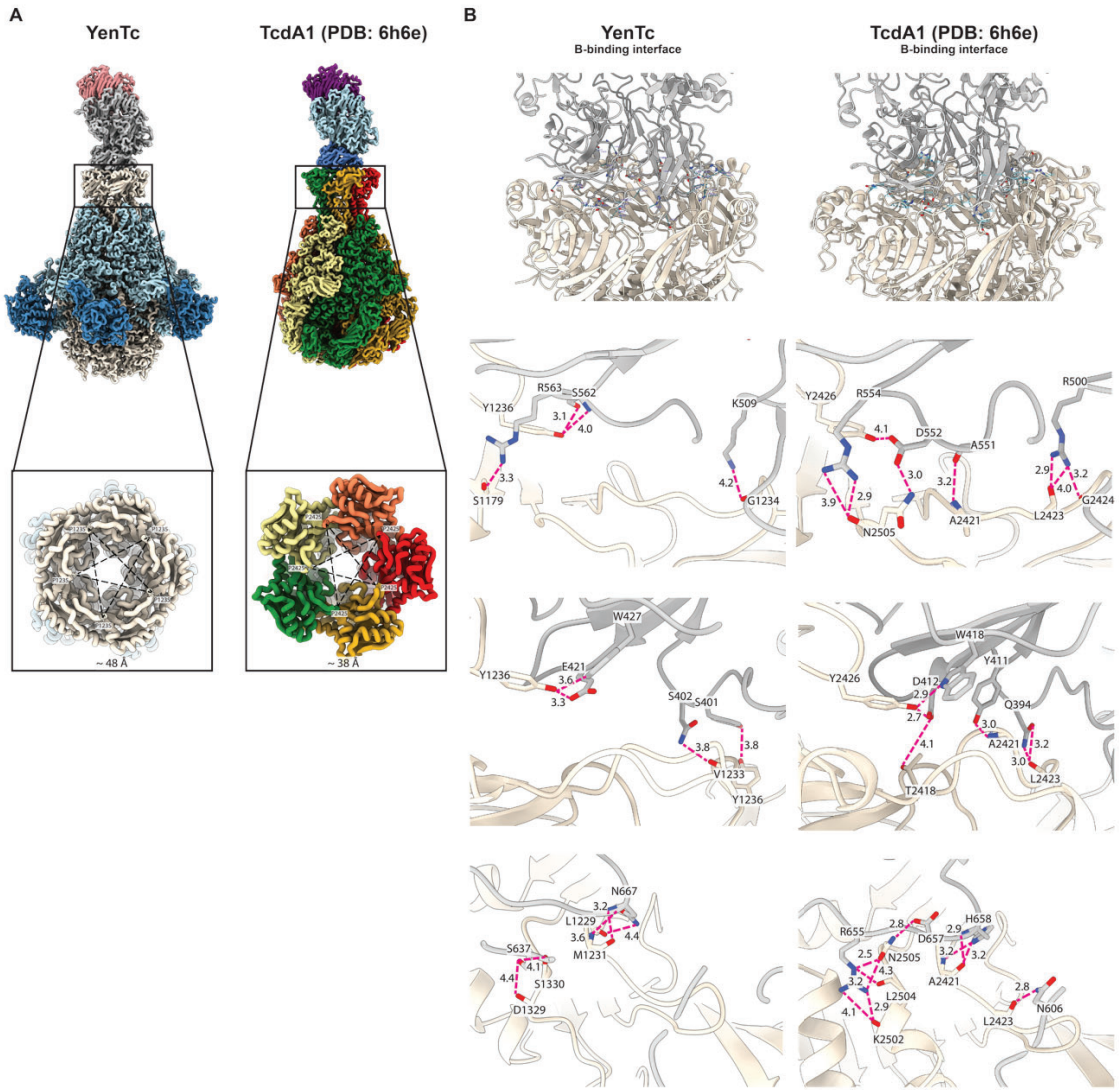

Figure 21: Diminished A-B bindings interface for YenTc causes lower affinity
(A, top) Cartoon representation of YenTc (left) and TcdA1 (right, PDB:6h6e) holotoxin colored according to their subunits. (A, bottom) Zoom in snapshots of the clipped view of their B binding domain. Distance measurement of a conserved proline reveals a ~ 10 Å broader B-binding domain for YenTc compared to TcdA1. (B) Structural comparison of the interaction interfaces of YenTc (left panels) and *Photorhabdus luminescens* (PDB code: 6H6E, right panels), A component with its corresponding B subunits. (Top panel) Overview image of B-binding interface with formed interactions depicted as sticks and a dotted line to indicate the interaction (blue). (lower three panels) Zoomed in perspective of three exemplary interaction sites with residues involved being represented as sticks and the interactions colored with pink dotted lines (lower three panels). A detailed list of interactions identified for both interfaces is presented in Table 2.

7.2.2 Pore structures underline structural versatility

To understand how pore formation is facilitated in YenTc, we also sought to determine the structure of the pore state. Based on the 11 Å reconstruction published previously, we expected a pore state structure largely resembling the pore state of PlTcdA1 [79, 86], where the outer shell is translocated to the top of the toxin, henceforth referred to as ‘canonical pore state’.

To our surprise, the pore model we obtained after applying the standard protocol used for pore formation in PlTcdA1 – toxin in lipid nanodiscs dialyzed against an alkaline pH (see chapter

6.2 for more details) – presented us reproducibly with a pore state in which the outer shell seemed to have dissociated (Figure 18 bottom panel, Figure S 7). The reconstructed 3 Å map allowed us to model the BC cocoon as well as the channel forming C-terminal part of YenA2 (from aa 854 forward) (Figure 18 bottom panel), however, YenA1 as well as both chitinases and the N-terminus of YenA2 could not be resolved. This left a reconstruction with a cone-like appearance, henceforth referred to as 'lollipop state'.

Since the 2D classes of both cryo and negative stain images showed additional features around the top of the channel (Figure 22A), we assumed that at least the N-terminus of YenA2 is still present but not resolved in the cryo-EM structure due to high flexibility. To confirm this, we send the purified sample to mass spectrometry analysis (performed by Dr. P. Janning, Table 3).

Interestingly, the data supported our hypothesis that YenA2 is complete but partially disordered; however, it also indicated that Chi1 remains attached to YenA2 (Figure 22C). YenA1 and its associated Chi2, on the other hand, were indeed missing, suggesting that both parts dissociated during the pore formation process. These results also explained why the N-terminus of YenA2 was disordered since both YenA2 and YenA1 together form the trefoil knot, which functions as a stabilization factor of the entire arrangement. To confirm whether split-A toxins require the components to be split for pore formation, Tc toxins from *Yersinia pseudotuberculosis* with fused A components were generated, clearly demonstrating that fused A components lose their toxicity despite the holotoxin being properly folded (Figure 22B, performed by Dr. P. Günther).

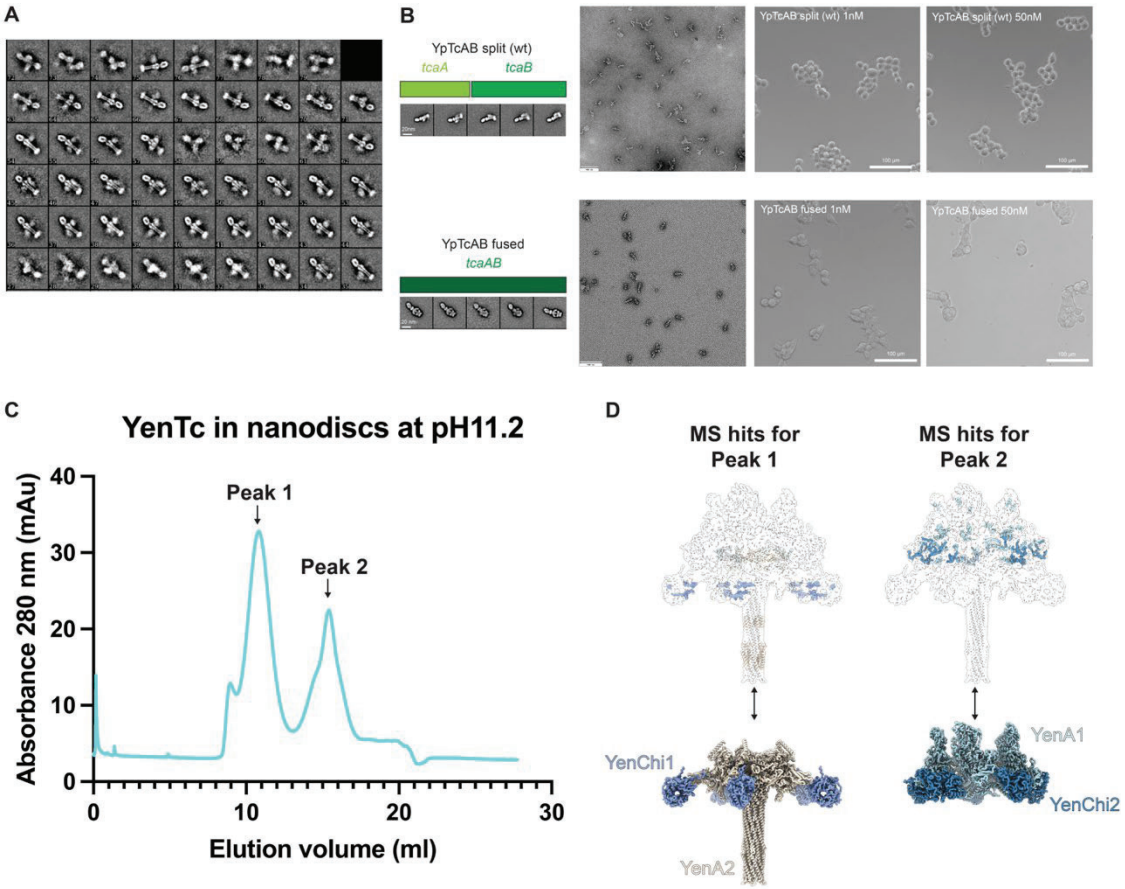

Figure 22: YenTc pore formation initiates shell release
(A) 2D classes of negative stain EM of YenTc holotoxin after pore formation in lipid nanodiscs. Next to the channel center, additional signals can be identified corresponding to the flexible N-terminal parts of YenA2. (B) Construct overview and exemplary 2D classes (left) of *Yersinia pseudotuberculosis* holotoxin using split-A (WT, top panel) or fused-A components (mutant, lower panel) and their toxicity towards HEK cells at 0, 1, and 50 nM (left to right) toxins. Whereas WT cells are dying, the mutant displays severe inhibition of toxicity. (C) SEC profile for the purification of YenTc pores after dialysis in nanodiscs. Whereas peak 1 represents the lollipop fraction, further determined to consist of YenA2 and YenChi1 (D, left), peak 2 corresponds to the missing outer shell and was confirmed to be YenA1 and YenChi2 (D, right) according to the top16 MS hits.

Piper et al. were already able to determine a low-resolution reconstruction of the canonical pore state [79]; however, a high-resolution rebuilding would be needed to better understand the changes that lead to the lollipop state. For this reason, we set out to identify conditions that would allow us to generate the canonical pore state reproducibly. To avoid using the same arguably harmful published procedure of freeze-thawing the sample, we screened various buffer substances and pH ranges (Table 4).

Ultimately, we achieved reproducible pore formation by increasing the concentration of the non-ionic detergent Tween-20, which appeared to alter the chemical environment sufficiently to induce pore formation at neutral pH without compromising the outer shell. The resulting ~3.6 Å reconstruction of the canonical pore state of YenTc also enabled us to model the holotoxin fully (except the highly flexible Chi1) (Figure 23, top panel and S5).

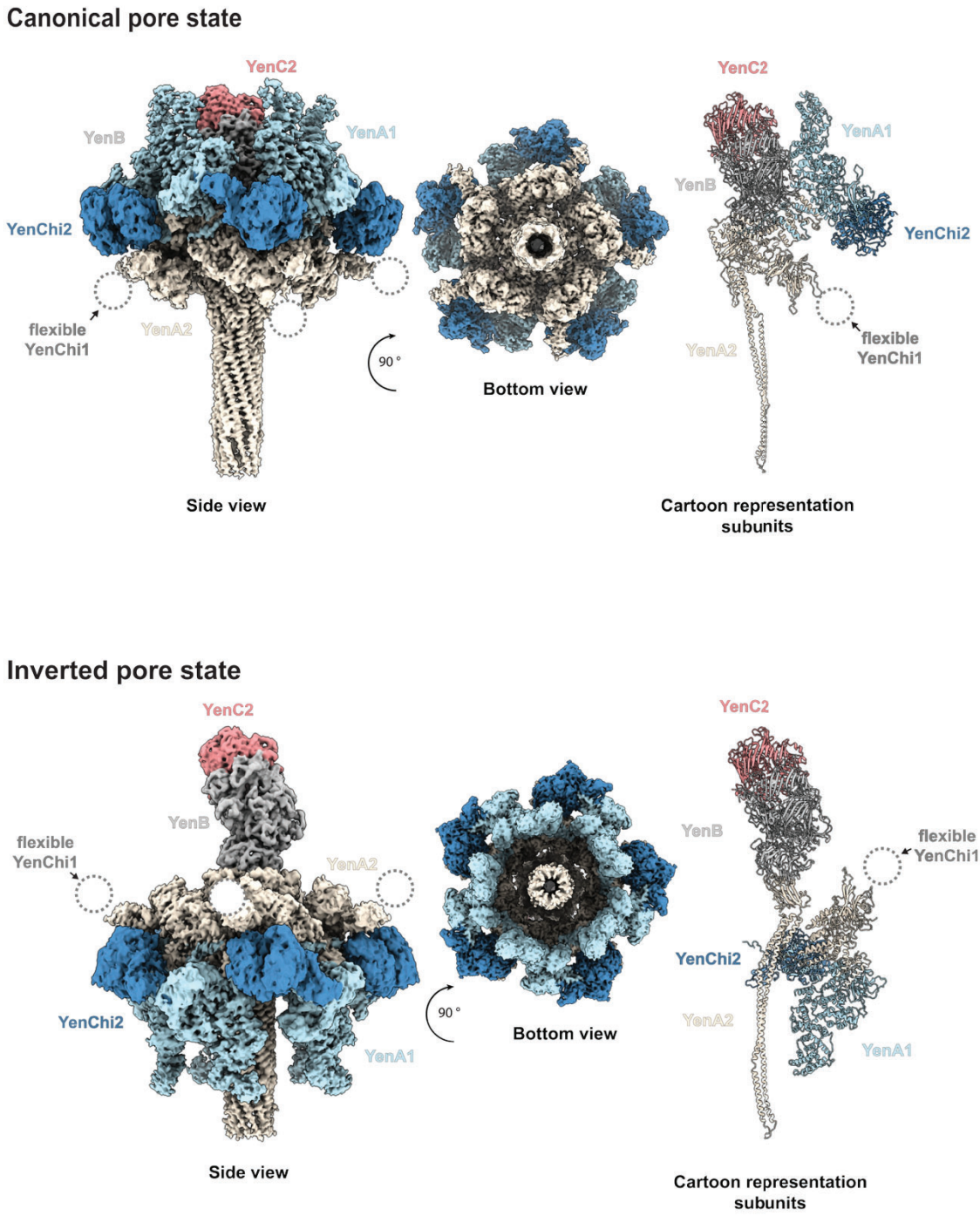

Figure 23: General architecture of YenTc canonical and inverted pore state
Composite cryo-EM maps (bottom and side view) and architectural model of canonical pore (top) as well as inverted pore state (bottom) colored according to the corresponding subunits (YenA1 in light blue, YenA2 in beige, YenChi2 in dark blue, YenB in gray, and YenC2 in red). Note: The additional subunit Chi1 could not be resolved in a regular cryo-EM reconstruction but would be attached to the protrusions of YenA2 visible in both panels (exemplified as dashed circles).

Not only are the interaction interfaces between YenA1 and YenA2 severely diminished in the pore state, increasing the likelihood of dissociation of YenA1 from the overall arrangement, but we could also observe a translational movement of Chi2 (Figure 24). This movement resulted in interrupted interfaces between the N-terminus of YenA1 and Chi2 and an increased degree of solvent exposure of the first, which is also the reason for the lower local resolution compared

to the prepore state (Figure 24). Since the N-terminus of YenA1 forms the trefoil knot together with YenA2, destabilizing this area might directly be linked to pore formation due to the interruption of the stabilizing trefoil knot.

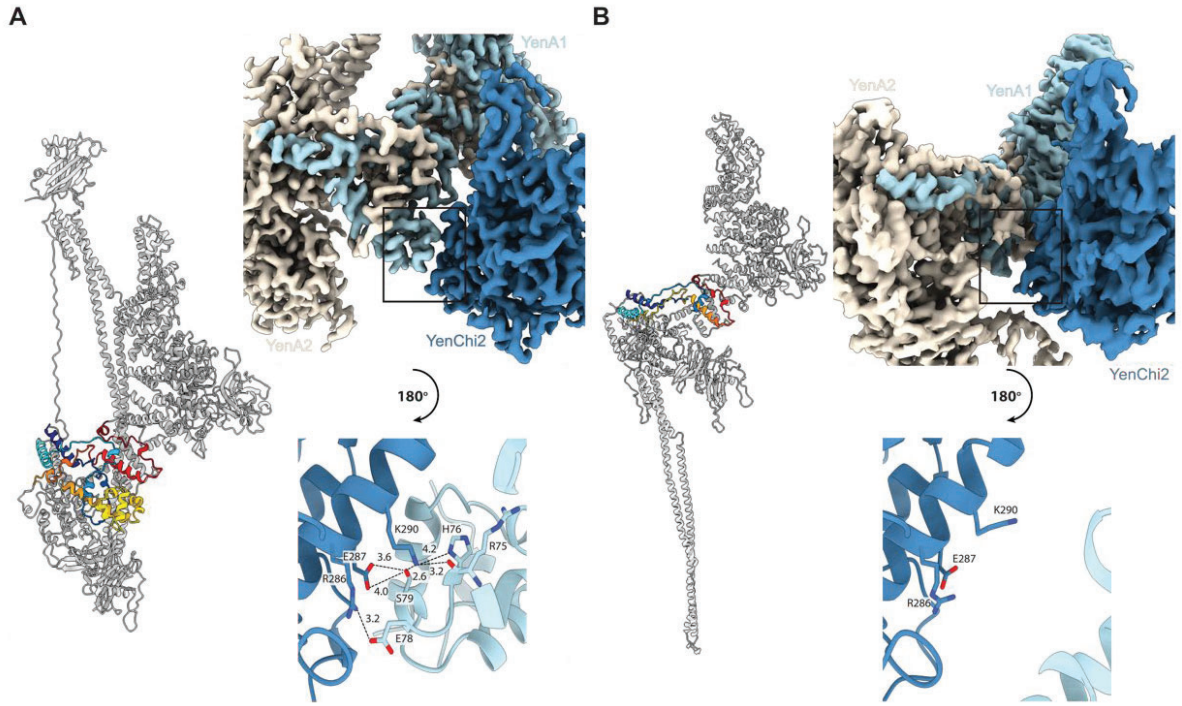

Figure 24: Chi2 mediates Trefoil knot solvent exposure
(A and B) Comparison of the YenA1-YenA2 interface with (A) and without (B Chi2 stabilizing it. Notably, the stabilization of Chi2 is centered around the N-terminal part of the trefoil knot, making the latter more solvent-accessible upon disruption of the interface, which favors the pore transition. (Atomic model of monomeric YenA1, YenA2, and YenChi2 for prepore (A) and pore (B) state of YenTc. Colored area depicting the conserved trefoil knot in closed (A) and open (B) states. Color code for A: YenA2 aa 715-813 from cyan to dark blue and YenA1 aa 16-203 from yellow to gold, orange, red, and dark red. For B: YenA2 aa 715-813 from cyan to dark blue and YenA1 aa 133-203 from yellow to gold, orange, red, and dark red.)

Additionally, we were also able to identify an electrostatic arrangement at the tip of the shell connecting it to the channel and keeping the latter in place (Figure 25). This electrostatic lock of the prepore state is distorted upon pore formation. The salt bridges formed by K256 and E257 of the next protomer keep the outer shell in a closed conformation which would support a pH-dependent mechanism, since the pKa of lysine is ~ 10.5 and the pH of the insect midgut lumen, in which the toxin is secreted, can be ~11-12 [143].

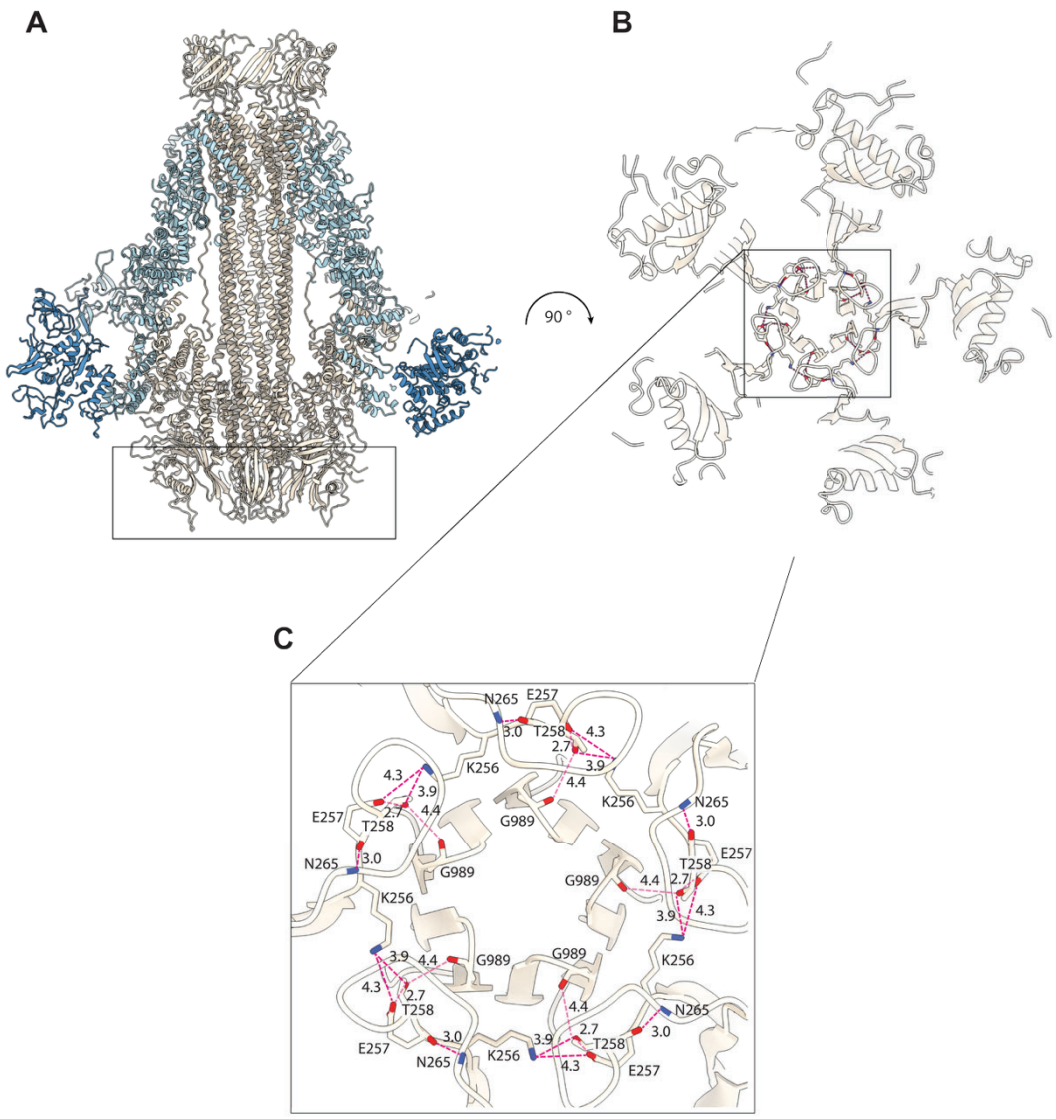

Figure 25: Electrostatic lock keeps the channel closed
Overview of the electrostatic lock keeping the channel in a closed state. (A) A cartoon representation shows the longitudinal section through the atomic model of YenTc prepore, with a focus on the neuraminidase-like domain encompassing the channel part. The bottom perspective (B) depicts the electrostatic arrangement (mainly facilitated via a salt bridge formed from K256 to E257), which stabilizes the closed channel conformation in its prepore state, and dashed lines in the zoomed-in (C) represent the interactions. Note that pKa(lysine) = 10.5, which could weaken the interface severely in an alkaline environment (like the insect midgut).

Taken together, these findings suggest that whenever chitinase 2 changes its position, for example due to substrate binding, pore formation is favoured. This is likely accompanied by a pH shift, which weakens the electrostatic lock and further destabilizes the arrangement. In addition, the data also provides insight into why the canonical state might be an intermediate state, whereas the actual result of the whole arrangement finishes in the 'lollipop state'.

To our surprise, in the cryo-EM data acquired for the canonical pore state, we also identified an almost equal number of particles resembling the pore state with an inverted arrangement of the outer shell, when compared to the canonical pore state (Figure 23, bottom panel, Figure S6). Since such an orientation was novel for all Tc toxins, we had considered it a processing artifact;

however, after performing multiple 3D classifications with and without image shift alignments, we could exclude this consideration.

After building and analysing the overall ~ 4 Å reconstruction of what we termed the 'inverted pore state' (Figure 23 bottom panel), we could identify a pivotal area (YenA2 aas 853-861) (Figure 26). The collapsing linker forms this feature during pore formation, after which the formed alpha-helix either points upwards, resulting in the outer shell arrangement resembling the canonical pore state (Figure 26A), or downwards, causing the inverted orientation (Figure 26B). Whereas in the canonical pore state, the amino acids from 857 onwards move towards the B-binding funnel of YenA2 and the formed α-helices interact quite closely with the existing arrangements, the helices in case of the inverted pore state are facing towards the channel tip and do not display an equally stable interface like the canonical pore state. This, however, might be a misleading interpretation since the aas 1250-1276 and 1346-1364 could not be modelled for both states and would coincide with the suggested interface. Ideally, the established interface would stabilise the arrangement and should allow for better modelling. However, the overall resolution already makes model building challenging, explaining why we cannot make statements about this area. Besides these and the orientational differences, the C-terminal parts of YenA2 in both pore states are identical in terms of the arrangement of the YenA2-YenA1 interface as well as the organization of the Chi1 bridging region.

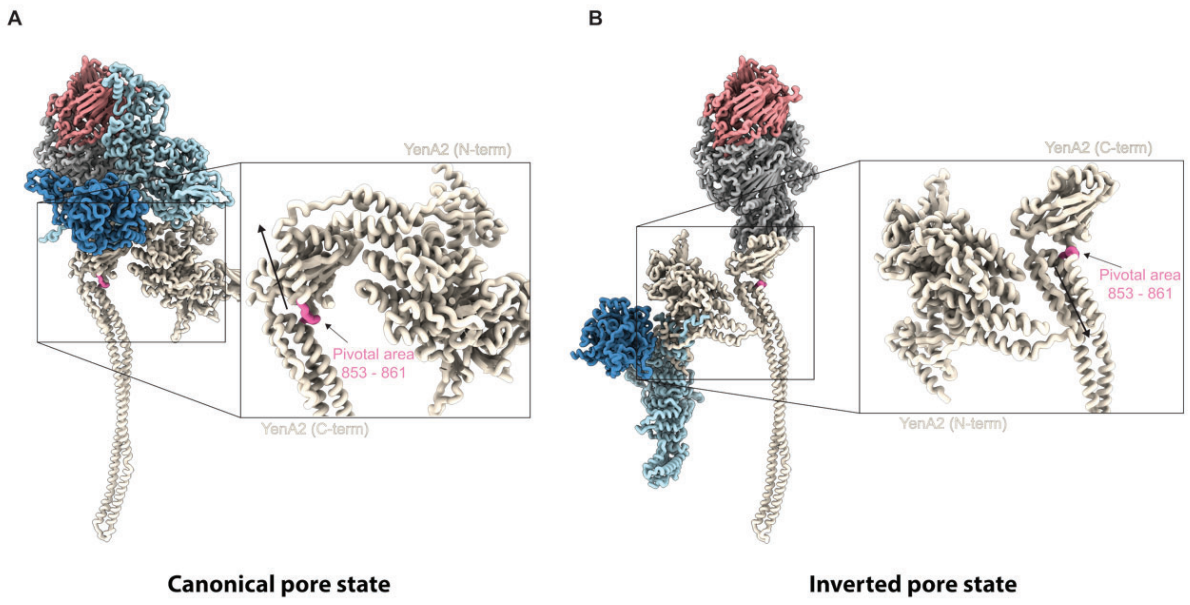

Figure 26: Pivotal area determines pore state orientation
(A and B) Overview of the pivotal area (pink) for both canonical (A) and inverted pore state (B). Zoom-ins highlight the orientational shift of the α-helical arrangement after the pivotal area, which determines the toxin's formation of a canonical (A) and inverted pore state (B).

Since this switching point appears to be related to the collapse of the linker, our assumption for the entire arrangement is that it is not a reversible process, allowing for flipping between the up

and down conformations, but rather that either one of those states is formed. Given that the inverted orientation significantly alters the distance of chitinases towards the channel tip region, these arrangements may allow for greater flexibility and enable the toxin to overcome potential height differences during sample interaction.

This could be an essential feature, as in insect midguts, the first level of pathogen protection is formed via a so-called 'peritrophic matrix', a mesh-like arrangement of mainly chitin layers that shields the epithelial cells from potential pathogens [144, 145]. The area between the peritrophic matrix and the cells, known as the ectoperitrophic space, is not a static distance but rather varies throughout the midgut. In this context, it would make sense to have a system that allows for bridging various distances and enables the toxin to react to changes more flexibly.

7.2.3 Structures and functions of YenTc effectors

To fully understand the entire toxin, we also investigated its effectors (RHS2, YenC1, and YenC2) and their potential mechanism. Since the RHS2 toxin structure had already been solved by crystallography (PDB accession code: 6AQK) (Figure 27A), we used AlphaFold2 predictions for the remaining YenC1 and YenC2 (Figure 27C and D, top panel) [142]. We compared the structural models with the homology structure to derive potential mechanisms from previously characterized effectors. This analysis revealed a striking resemblance of RHS2 with the Iota toxin from *Clostridium perfringens* (PDB accession code: 4H03), which ADP-ribosylates globular (G-) actin at R177 (Figure 27A, lower panel) [146]. Biochemical analysis (performed by my colleague Dr. A. Belyy, unpublished) of the toxin showed that indeed RHS2 shares the exact mechanism as the iota toxin, in contrast to the commonly studied Tc toxin effector TccC3 from *Photorhabdus luminescens*, which ADP-ribosylates only filamentous (F-) actin (Figure 27B) [92].

The structure homology search identified the predicted YenC1 model to be closely related to the structure of cytotoxic necrotizing factor 1 (CNF1) (PDB accession code: 1HQ0) [147] and CNF1 homologous Tc toxin effectors (PDB accession code: 6YHM) from *Yersinia pseudotuberculosis* (Figure 27C lower panel) [148]. Most importantly, the active centre is conserved, as H833 and C818 (H881 and C866 in CNF1) form the catalytic triad together with the backbone hydroxyl group of L785 (V833 in CNF1) [147]. This suggests that YenC1 deaminates Rho-GTPases and therefore has a crucial influence on the cytoskeleton of the target cells. The biochemical activity studies have not yet been performed until the generation of this document and will have to be persued in future.

The results for YenC2 were not as convincing as for RHS2 and YenC1. Not only is the confidence rate lower for the predicted structure, but also identifying possible homologous structures proved to be more difficult. There seems to be some structural similarity with the human cytidine deaminase (HCD) structure (PDB accession code: 1MQ0) [149] as well as the nucleotide deaminase superfamily from Bacillus YwqJ. However, this similarity holds only for the inner core of the prediction (Figure 27D, lower panel).

Multiple sequence alignments (MSA) between homologous sequences (Figure 27E) suggest a potential conserved zinc finger motif (Cys_2His_2 zinc finger) between H878, H896, C940 and C943. In general, the high conservation of H868 would indicate potential involvement, but the predicted structural distance suggests otherwise. The version of the zinc finger motif, however, does not line up with HCD, which employs a Cys_4 zinc finger motif to modify nucleotides [149]. If the zinc finger hypothesis holds, it is another indication that the AlphaFold prediction is not very accurate, since the most significant distance between the moieties is ~ 9 Å apart, which would not be a physiologically relevant distance.

Combined, the data suggest that YenC2 functions as a DNA/RNA-modifying enzyme, which also explains the increased toxicity observed in cell culture assays and would be the first known Tc toxin effector that does not directly affect the cytoskeleton. This, however, requires further biochemical characterization.

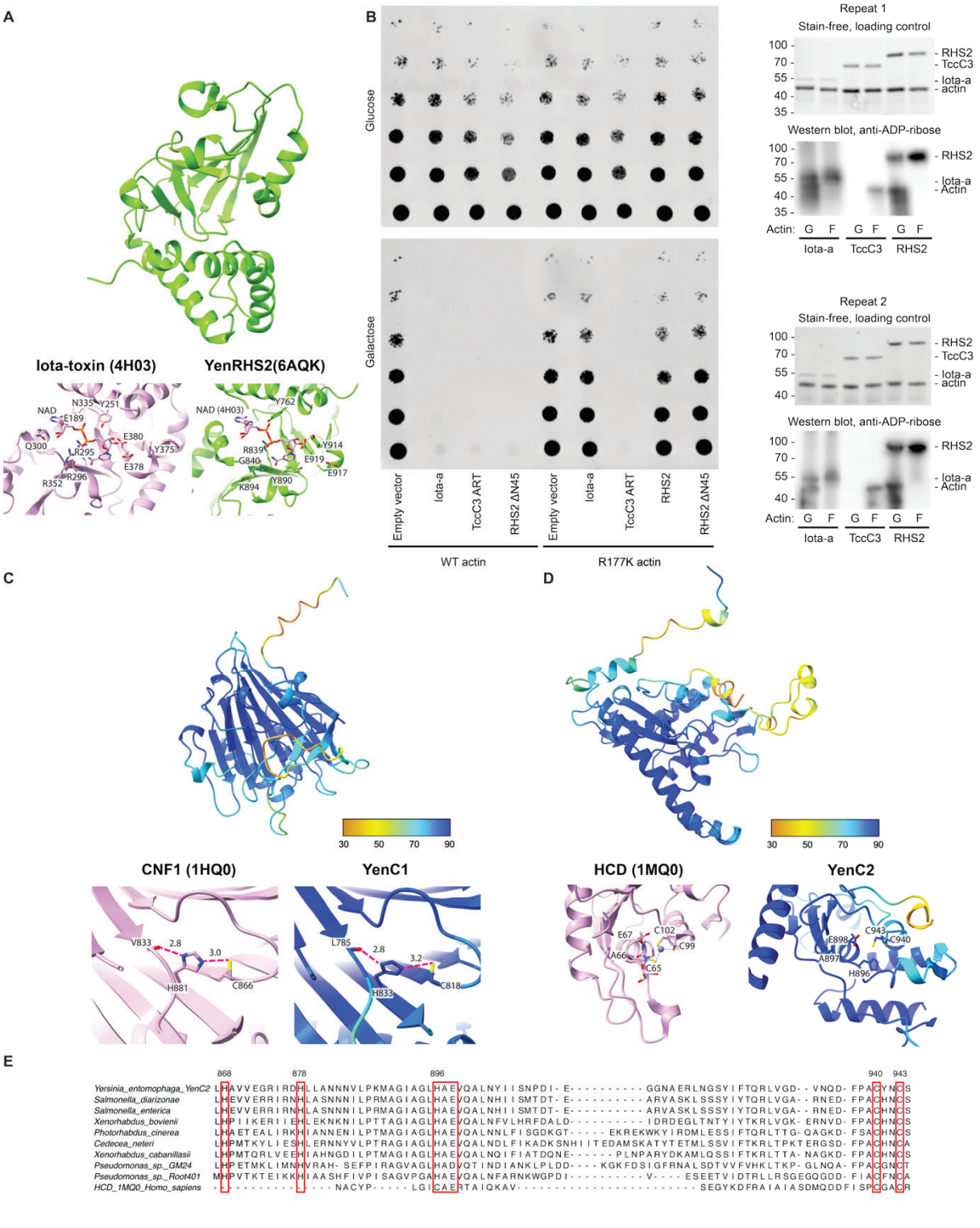

Figure 27: YenTc effectors and their supposed function

(A) Overview of YenTc effector RHS2 structure (PDB code: 6AQK) (upper panel) and zoom-in images on the active center of Iota-toxin (PDB code: 4H03) compared to RHS2 with overlaid NAD structure. Notably, although the sequence identity is relatively low, the interface is largely maintained.

(B) Yeast drop test demonstrates RHS2's toxicity and the dependence on actin R177 compared to the Iota toxin (left panel) and Western Blot analysis against ADP-ribose in G- and F-actin samples treated with Iota toxin, TccC3, and RHS2 (right panel), highlighting its targeting of G-actin.

(C + D) Structural overview (upper panel) of YenC1 (C) and YenC2 (D) AlphaFold2 predictions and comparison of the active center to close homologs (lower panels), namely 'cytotoxic necrotizing factor 1' (CNF1 – PDB code: 1MQ0) for C1 as well as 'Human Cytidine Deaminase' for C2. Note: Whereas CNF1 is very closely conserved towards YenC1, HCD and YenC2 are rather distant, except a potential zinc-finger motif further highlighted (red marks) in an MSA of toxic effectors for different bacteria (E).

7.2.4 Concluding Discussion

Previously, it has been demonstrated that chitinase 2 is the enzymatically active chitinase, whereas chi1 primarily serves a receptor recognition function [27]. Furthermore, the insect midgut cells, which *Yersinia entomophaga* naturally targets, are not only embedded in a highly alkaline environment (pH 11-12) but are also protected by a separate mesh-like arrangement called the peritrophic matrix [144, 150]. This defence grid is primarily composed of multiple layers of chitin chains, which become increasingly dense throughout the insect's midgut, thereby preventing pathogens from attacking. Whereas the anterior parts of the matrix would allow Tc toxins to attack the midgut cells, the posterior parts would be protected successfully. Together with our experimental data, we therefore propose a mechanism (Figure 28) in which the Tc toxins use their structural variability to adapt to different conditions and potentially allow a degradation of the peritrophic matrix after their release into the midgut lumen:

After the release, the large Tc toxins would only be able to penetrate the anterior parts of the peritrophic matrix due to size limitations. The contact is most likely first initiated by the highly flexible Chi1 subunits (to allow for distance shifts in the mesh arrangement). When Chi2 then binds to the matrix, it not only starts degrading the matrix but also changes the interaction interface with the N-terminus of YenA1, destabilizing and surface-exposing the trefoil knot.

Together with the highly alkaline environment of the midgut, which weakens the electrostatic lock, and the change of electric potential due to the proximity to membrane lipids, pore formation is induced and depending on the distance between the peritrophic matrix and the plasma membrane, either the canonical or the inverted pore state is formed.

Furthermore, due to the smaller interaction interface of YenA1 + Chi2 and YenA2 combined with the alkaline environment, YenA1 + Chi2 dissociate from the complex, leaving the lollipop state as the final conformation. The release of Chi2 also provides the advantage that the enzymatically active chitinase is no longer locked in place but is released into the lumen, allowing it to degrade the matrix further and thereby priming it for attacks by other Tc toxins in more posterior parts of the midgut.

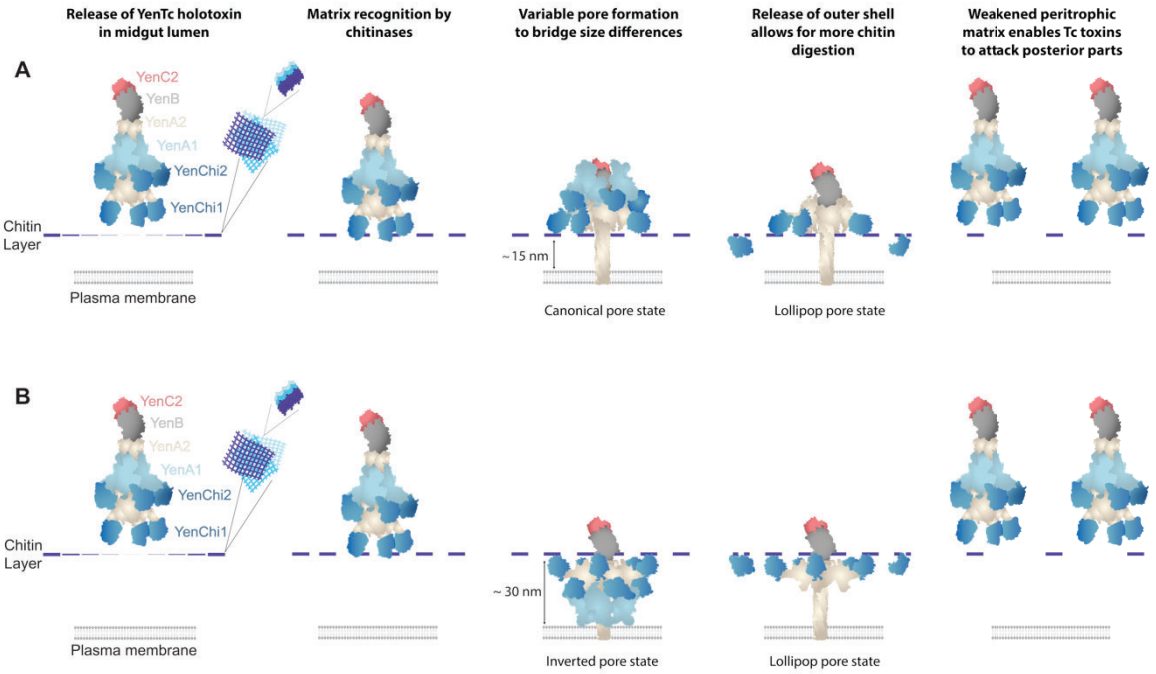

Figure 28: YenTc translocation mechanism and importance of conformational changes
(A and B) Schematic representation of YenTc intoxication. Upon release of YenTc into the midgut, the Chitinases attached to YenTc interact with the chitin layer (as part of the peritrophic matrix), shielding the epithelium. Initiated via the alkaline pH (weakening the electrostatic lock), the chitin-binding (weakening the stabilization of the trefoil knot) and the interaction with the plasma membrane (PM), the Tc toxin is transitioning from its prepore to its pore state and ultimately ending in the lollipop state, shedding YenA1 and YenChi2 completely. The chitinase release, in turn, enables the continuous digestion of the chitin layer and subsequently the attack of more toxins. Conformational changes between an up-facing shell (A) in the neutral pore state and a down-facing shell in the alternate pore state (B) are used to bridge the differences in distance.

A previous study identified the pH optimum for Chi2 to be around pH 5 and was unable to detect activity at pH values above 10, which would be in conflict with our hypothesis. However, studies on acidic mammalian chitinase (a very close homologous structure to Chi2 according to Foldseek [135], e-value = 2.74e-24) showed that even chitinases which usually work best at low pH ranges, can display profound activity at highly alkaline pH values (up to pH 11) [151]. Together with the observation from the previously mentioned paper that Chi2 displays higher activity in the presence of alkaline pH ranges and the entire Tc toxin, this might support our concept. Ideally, this ambiguity is best resolved by biochemical analysis; however, proving this hypothesis in a more physiological system may be challenging, as none of the established cell lines have chitin layers surrounding them or can survive in alkaline pH conditions for extended periods. However, there are attempts to develop insect midgut cells for cell culture, which could provide the base for future control experiments [152]. Additionally, introducing point mutations to YenTc is not only challenging due to the native host system but also leads quickly to improper folding and unsuccessful expression (especially when targeting the N-terminus of YenA1). Most promising in this regard would be the direct analysis of infected tissues via cryo-

ET. However, this requires access to the native host system and an established cryo-ET protocol to follow the interaction of Tc toxin with host cells, which will be discussed in the next chapter.

This study has raised several questions that could be addressed in future research. A critical area of investigation is the exact mechanism of toxicity of the hypervariable regions (HVRs) of YenC1 and YenC2. They are predicted to function as a Rho GTPase deaminase and a nucleotide deaminase, respectively; however, further biological controls are needed to confirm these predictions. Furthermore, it would be interesting to know whether the effectors are being used randomly (the different copy numbers provided by MS analysis (Figure S8) would suggest otherwise) or follow a specific pattern, e.g., host dependence.

Additionally, molecular dynamics simulations could be used to gain a better understanding of why Tc toxin pore formation can be efficiently triggered by increasing the local concentration of toxin and detergent micelles, as achieved in this study using a concentrator membrane. This suggests that the toxin's pre-pore state can be destabilized by direct contact with lipid membranes, which is independent of other known triggers such as receptor binding or pH changes.

While we can edit the genome of *Y. entomophaga* to make larger changes, it remains difficult to create precise point mutations in this system. Therefore, another goal for the future could be to improve the existing system or establish a more effective one. For example, generating *Y. entomophaga* strains that already possess an endogenous CRISPR-Cas system would make future genetic work significantly more targeted and efficient [153].

Regarding translational research, the use of chitinases as a specific receptor recognition system may not be directly applicable; however, understanding the general steps of intoxication for YenTc might allow for the adaptation of the system accordingly. Furthermore, features like the ability to eject the shell during intoxication might be shared among more split-A Tc toxins. They could potentially be exploited to generate a system where, for example, specific glycosidases are released to counteract cancer immune suppression, such as PD-L1 glycosylation in triple-negative breast cancer [150], thereby creating a fail-safe option in case killing the cancer cells is not effective.

7.3 Towards structural characterization of Tc toxin entry into host cells

To date, most studies on Tc toxins have been based on *in vitro* experiments, as experiments performed *in vivo*, i.e., in a native organism, are technically challenging to execute. However, *in vitro* experiments cannot compensate for the complexity of biological systems and may introduce artifacts. Especially in the context of structural studies, it is desirable to study single molecules or complexes in their physiological environment.

While some *in vitro* experiments suggest that pore formation of Tc toxins can occur at alkaline pH (see pore formation protocol in Chapter 6 for more details), colocalization studies using fluorescent light microscopy (Figure 29) indicate that they use the endosomal pathway and are activated by acidification of endosomes during the endosomal maturation process [68]. Furthermore, previous toxicity studies employing bafilomycin have shown that the inhibition of V-ATPases strongly impairs the toxicity of Tc toxins, supporting the hypothesis of endosomal uptake [81].

As previously mentioned, CRISPR knock-out studies have identified a family of highly glycosylated plasma membrane receptors (VSG) that are crucial for toxin binding and subsequent endocytosis [83]. However, despite extensive efforts by many researchers, including myself, it has proven challenging to isolate receptors in complex with the toxins, although *in vitro* affinity measurements suggest strong binding.

Collectively, these contradictory observations suggest that key factors governing these complex machineries are still not fully understood, and *in vitro* experiments may lack the complexity to analyse the molecular mechanisms in sufficient depth. To address these issues, we set out to observe the process of Tc toxin interaction with their host cell and its cellular entry as well as intracellular trafficking by employing cryo-ET.

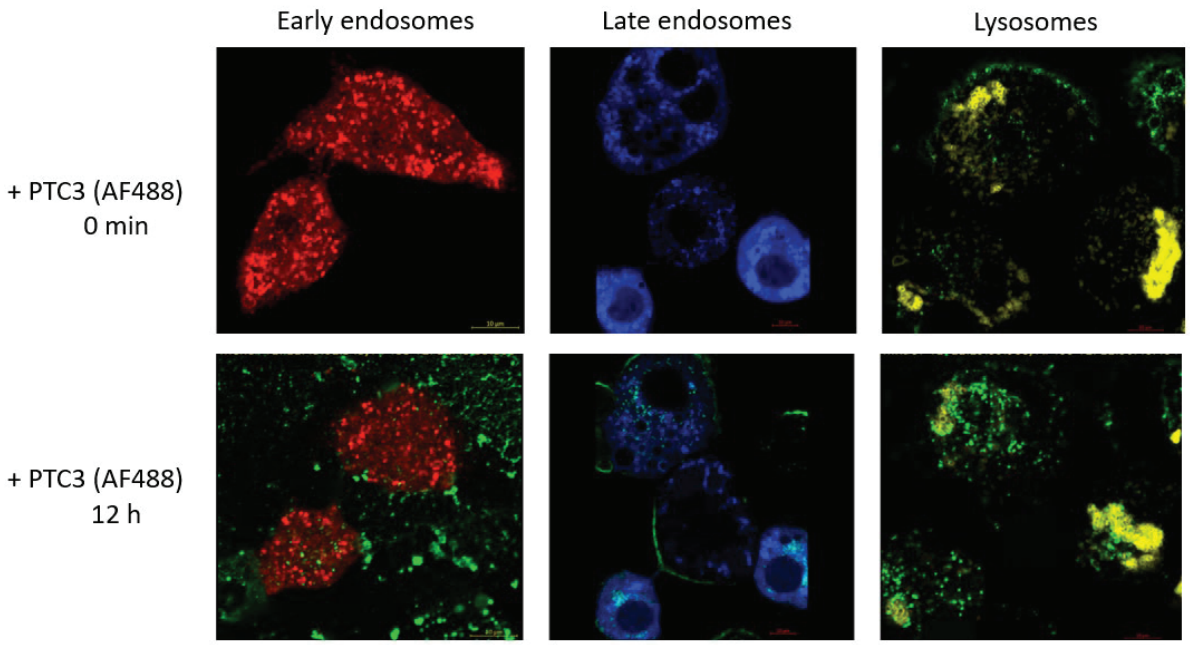

Figure 29: Fluorescently labeled Tc toxin infecting cells with progressive endosomal maturation
Light microscopy images representing fluorescently labeled early endosomes (left panels), late endosomes (middle panels), and lysosomes (right panels) in the presence of 10 nM fluorescently labeled (green) PTC3 after 0 min (upper panels) or 12 h (lower panels) incubation time.

7.3.1 Fluorescent reporter system

To study the uptake of Tc toxins into mammalian host cells using cryo-ET, the overall aim was to precisely localise the target of interest using cryo-CLEM. To this end, we fluorescently labelled the toxins using a two-step click-chemistry labelling method. After successfully purifying the individual components, we labelled the A component with AlexaFluor 488 via an NHS-ester linkage and the B/C component with AlexaFluor 647 via a maleimide linkage to control holotoxin formation. To demonstrate that we were able to generate fluorescently labelled, yet still functional, holotoxins, we performed cellular infection assays that showed unimpeded toxicity. To visualise components of the endosomal pathway at the ultrastructural level, we transfected HEK cells with plasmids encoding either mCherry-Rab5a for early endosomes, BFP-Rab7a for late endosomes, and LAMP1-mKOet (Kusabira Orange) for lysosomes. While the expression of endolysosomal marker proteins provided clear signals for the individual states of the endolysosomal compartments, it did not allow for the tracking of endosomal vesicles throughout the entire maturation process. However, this would be necessary to undoubtedly follow the Tc toxin uptake into the cells via the endolysosomal route and their proposed interactions with the different endosomal compartments. Co-transfection of plasmids for multiple maturation stages, however, leads to a high variance in expression profiles and may be potentially misleading.

To achieve a homogeneous and strong expression profile in the cell population, we designed a single construct that combines all fluorescent markers under the same three promoters (Figure S11). Since standard transfection reagents yielded inconsistent results, we employed the Multi-Bac system, which was designed to express multiple proteins in stoichiometric amounts [154]. Dr. O. Sitsel kindly provided the initial vectors.

Surprisingly, the transfection efficiency turned out to be low, with only ~10% of cells showing a fluorescent signal, most likely due to the virus's low potency, which may be related to low generation cycles or batch-to-batch variations. Upon regenerating the P2 virus with a stronger potency and the addition of 10 mM sodium butyrate, the transfection efficiency increased to 25%, which we deemed sufficient for our experiments. Initial discrepancies in the synchronicity of protein expression, where we observed fluorescence for one maturation stage but not for the other, could be resolved by increasing the incubation time.

All in all, we were able to generate a functional fluorescent expression system for the mammalian endosomal system, which we could use as a basis for our reporter system (Figure 30 and Figure 31).

7.3.2 Initial intoxication tests using reporter system

Next, we designed an RT-fluorescent microscopy experiment, utilizing the fluorescent reporter system in conjunction with fluorescently labelled Tc toxins to test the experimental concept.

For this, we infected cells with the virus and added 10 nM of the fluorescently labelled Tc toxin. We found that the toxin uptake took about eight hours. The addition of 5 mM $CaCl_2$ accelerated this process to ~1-2 hours, which is consistent with observations from previous studies (Figure 30) [83]. The exact mechanism by which $CaCl_2$ assists uptake is unknown. One hypothesis is that the addition of $CaCl_2$ leads to a general increase in endocytic activity [155].

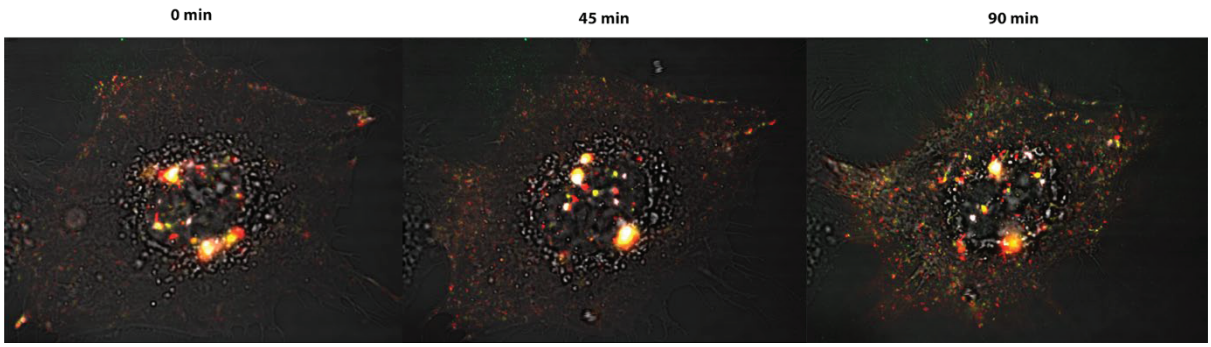

Figure 30: Intoxication timeline monitored by fluorescence

HeLa cell intoxication monitored over time for 0 min (left panel), 45 min (middle panel) and 90 min (right panel) using fluorescent markers for early endosomes (red), late endosomes (blue), lysosomes (yellow) and Tc toxins (green) indicating a

successful intoxication of the cells. Note: No fluorescent signal was detected for late endosomes and the cell underwent apoptosis later throughout the time-lapse recording due to the laser power.

Alternatively, the additional ions may favour the interaction between the plasma membrane receptor and the toxin, thereby increasing uptake into cells. Another, however less likely possibility is that the addition of $CaCl_2$ changes the local electric potential of the cell and thereby causes structural rearrangements that would favour the uptake of the toxin.

We were able to observe all endosomal maturation states and the fluorescent toxins using a Zeiss LSM 800 confocal fluorescent microscope (Figure 31). Although occasionally not all fluorescent signals were present in all cells (Figure 30 and Figure 31), we can nonetheless track the fluorescently labelled toxin throughout the cells. With this system in hand, we moved to the next step of implementing it into a cryo-ET workflow.

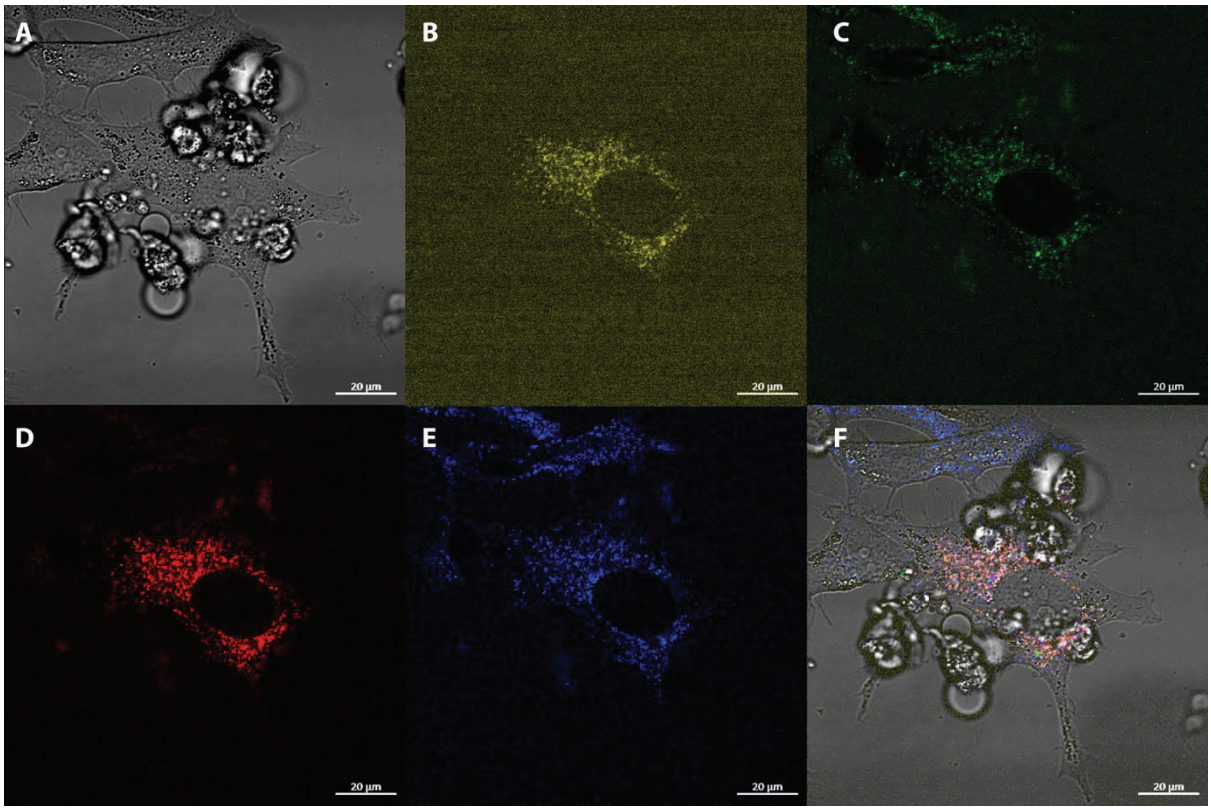

Figure 31: Fluorescent reporter system expressed in HeLa cells
Light microscopy images representing fluorescently labelled HeLa cells with an epifluorescence channel (A), a mKOet channel (B) for lysosomes, an AlexaFluor488 channel for the Tc toxin, a mCherry channel (D) for early endosomes and BFP channel (E) for late endosomes. The channel merger (F) represents a clear distinction of the fluorophore and a proof of principle.

7.3.3 Sample preparation and tomogram acquisition

To successfully analyse Tc toxins using cryo-ET, it is crucial to avoid the formation of intracellular ice crystals as much as possible. To this end, we optimised the blotting conditions for HeLa cells. Initial attempts were monitored using SEM imaging. Although the sample appeared

relatively thin and vitreous, clear reflections were detected inside the cells during the milling process, indicating either insufficient vitrification due to non-optimal blotting conditions or insufficient heat dissipation due to cell thickness.

To address this issue, we adjusted various blotting parameters, including longer blotting times, stronger blotting forces, and more extensive PBS washing steps before plunge freezing, to minimise excess media that could limit vitrification. However, this result either did not improve the ice quality or resulted in cell deformation, indicating that too much force had been applied.

As the composition of the cell medium also affects the quality of vitrification, we added different cryoprotectants to achieve a more homogeneous freezing process. Adding 5% glycerol to the medium 15 minutes before plunge freezing improved the vitrification process, resulting in no reflections being detected during SEM imaging.

Following successful sample preparation, the frozen grids were imaged in the FIB/SEM using the built-in fluorescent microscope, which allowed precise correlation of the regions of interest. However, due to the LED lamp system and a weak detector, the crosstalk effects between the mCherry, mKOet, and AF488 signals were too strong to allow proper differentiation between the different signals (Figure 32). While a laser-based fluorescent system can excite samples with a single wavelength, the LED system uses prisms to filter out wavelengths. This process, however, only allows the excitation wavelength to be limited to a range of wavelengths. If this range encompasses the excitation wavelengths for multiple fluorophores in the sample, the detected emission cannot distinguish between them, leading to the aforementioned crosstalk effects.

The crosstalk between the channels still allowed us to perform 2D correlation and indicate the approximate location for milling, albeit without the differentiation between the maturation states (we were able to use the AF647 signal to distinguish the toxin signal).

In a general cryo-ET setup, plunge-frozen samples are transferred into the SEM cryo-stage and sputtered with platinum to protect the sample from radiation damage. Hereafter, the target of interest is identified, and the material above and below is milled away using gallium ions (decreasing currents to limit sample damage) (Figure 32D, E and G). To ensure a high signal in TEM imaging, the cells are thinned to a final thickness of ~100–150 nm, referred to as lamellae. Since the size of endosomes, generally varying between 100 nm and 1µm, is already bigger than the lamella, the localisation of the target of interest must be as precise as possible to avoid removal of the ROI by accident.

The most optimal version for this goal would be a 3D correlation to also account for the z dimension. However, 3D correlation with our setup was impossible without the use of specialised fluorescent beads, as shown by colleagues. These beads, in turn, require treatment of the grid, which is incompatible with our sample preparation, as we need to incubate the cells with baculovirus. We therefore decided to restrict the analysis to 2D correlation only, hoping to hit the right z-dimension by chance.

Next, the milled samples were transferred into a TEM to acquire tomograms of the fluorescent areas, as observed during SEM imaging. Initially, image acquisition was performed at 81,000× magnification, with defocus values ranging from -2 to -4 µm, to obtain images that would enable high-resolution reconstruction in the event of sub-tomogram averaging. However, as no toxins were identified in the initial reconstructions, we continued with lower magnification (42,000x) and higher defocus values of -5 to -8 µm to achieve greater contrast and a larger field of view. This magnification corresponds to a pixel size of ~ 2.3 Å per pixel. It allows the ~ 350 Å toxin to be represented by 15-20 pixels even when the image is downsampled (bin8), which is typically used to increase the contrast of the reconstructed tomogram.

Initial attempts at manual and reference-based picking using crYOLO [128] and TomoTwin [156] revealed the presence of vesicles inside the cells that were decorated with particles that appeared homogeneous in appearance (Figure 33). However, these particles were later identified as ribosomes – previous studies had reported these arrangements to be ribosome-associated vesicles (RAVs) [157]. No picking setup was able to identify particles corresponding to Tc toxins, leading us to conclude that they are not present in the imaged samples.

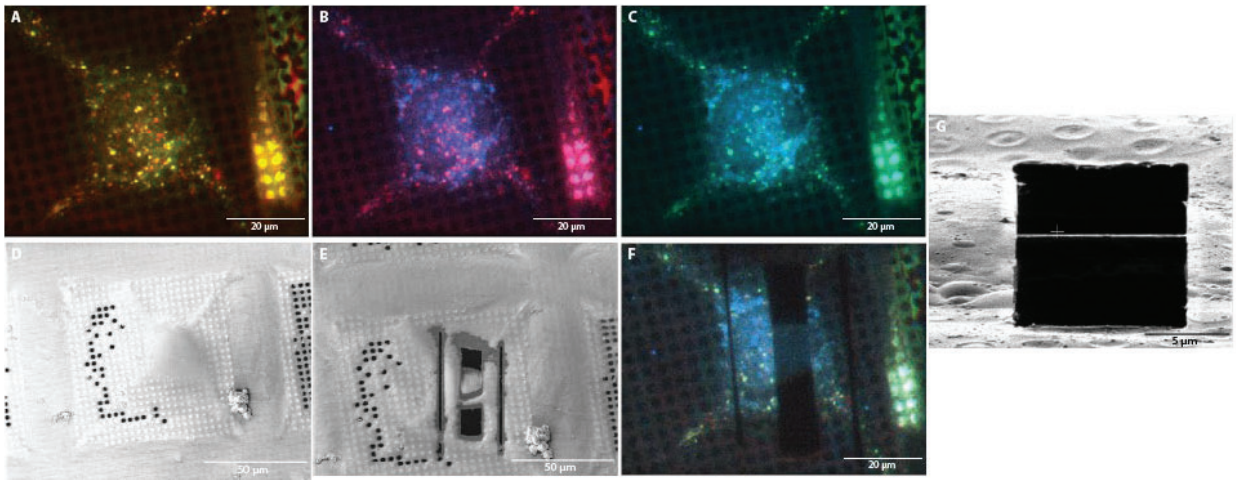

Figure 32: Correlative light and electron microscopy
(A-C) Cryo light microscopy images of a HeLa cell, plunge frozen on a grid, representing different fluorophores present. Green fluorescence represents the endocytosed toxin within the cell. Red signal corresponding to the early endosomes, as well as blue fluorescence for the late endosomes. Note: Lysosomes were not imaged due to limitations in detecting them against the red emission. (D, E and G) Cryo scanning electron images of the same cell as in A-C before milling (D), during milling (E), and with the final lamella (G). (F) Exemplary fluorescent image after milling.

7.3.4 Direct imaging of the cell periphery

As the CLEM-mediated approach yielded no promising results, we decided to try a different approach to track Tc toxins throughout the cells. As previously mentioned, cells are usually too thick to be imaged directly with TEMs; however, the cell periphery of HeLa cells was determined to have an average thickness of ~200 nm [158]. This thickness is within the range required to acquire high-quality tomograms when using a well-aligned energy filter. An energy filter is designed to filter out inelastically scattered electrons, which would otherwise be represented as noise in the reconstructed tomograms and decrease the overall contrast. Avoiding the milling step allowed us to save time and reduce contamination from transferring the sample back and forth multiple times. This problem was also addressed during this study by colleagues through the implementation of a cryogenic glove box, which maintains a constant humidity level. However, we encountered some problems during the process due to the varying degrees of thickness at the cellular periphery, resulting from their heterogeneity, which led to tomograms of different thicknesses. Another factor contributing to the lower contrast was the fibronectin coating applied during sample preparation for cell attachment to the grids, which also resulted in less optimal data acquisition.

To address these issues, we pre-treated the grids with Galectin-8, which promotes cellular adhesion and causes the cell body to spread in the cellular periphery, resulting in sufficiently thin cellular samples [159]. Galectin-8 plays a crucial role in cellular proliferation processes, is upregulated in cancer cells, and is of particular interest due to its involvement in motility, which involves interactions with integrins and the extracellular matrix. It additionally acts as a matricellular protein with a potency similar to that of fibronectin.

Although growing cells on Gal-8-coated grids resulted in uniformly shaped cells, we were still unable to identify toxins in the reconstructed tomograms. This may be due to lower contrast in the tomograms caused by the galectin treatment, a local decrease in toxin-endosome concentration at the cellular periphery since the cell body is drastically enlarged, insufficient detection of Tc toxins using crYOLO/TomoTwin, or simply under-sampling of the cells. Without a fiducial-based localisation, it was not possible to identify Tc toxins in the acquired tomograms.

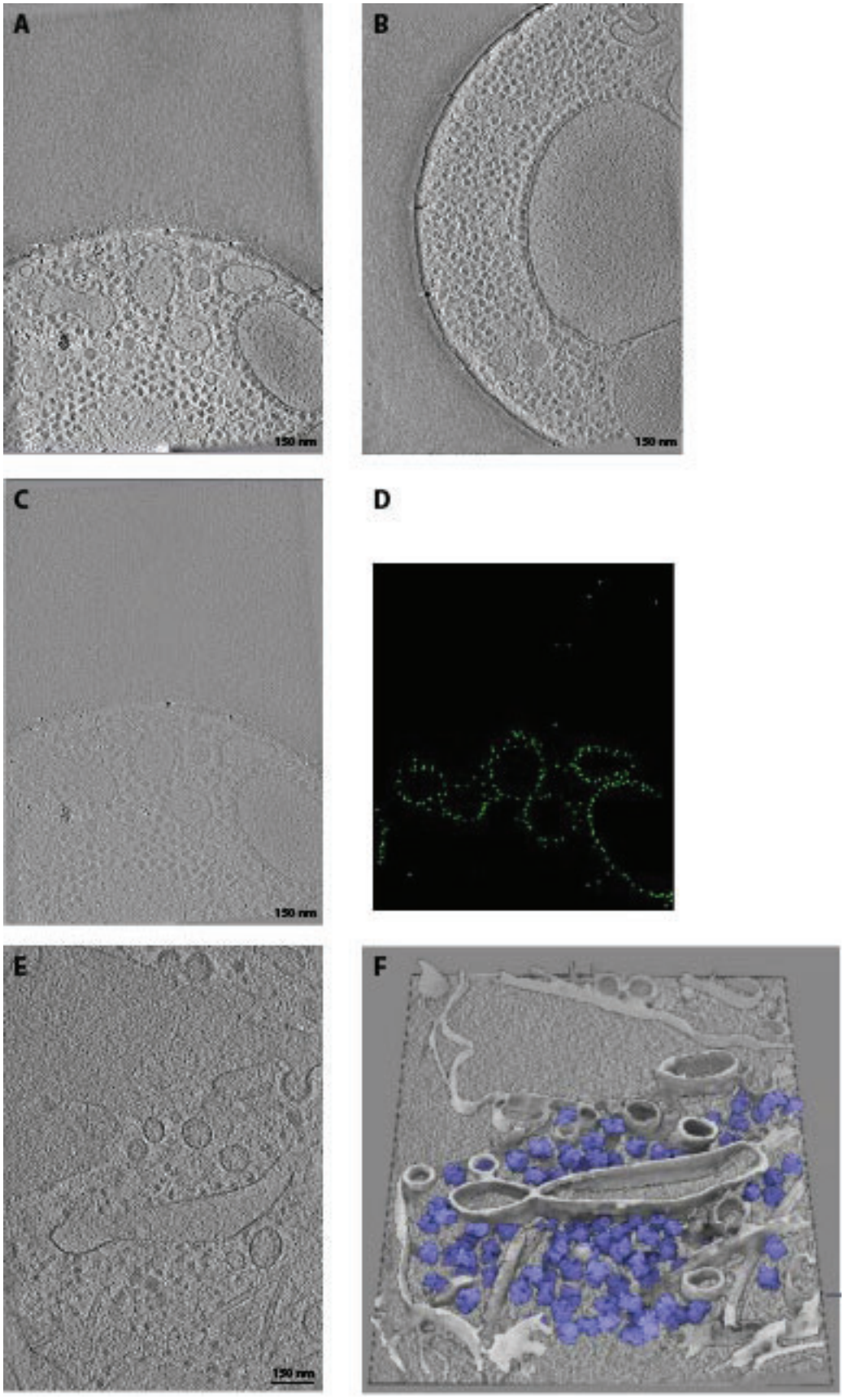

Figure 33: Direct imaging results with different picking procedures
(A-C, E) Examples of Cryo-ET tomograms depicting features in the size of toxins.
(D, F) Exemplary representation of identified ribosomes by crYOLO (D) and with TomoTwin (E). Segmentation in F is adapted from [156].

7.3.5 Localisation using gold beads as fiducials

As we were unable to identify Tc toxins in tomograms acquired near the cellular peripheries (direct imaging), we attempted to optimise CLEM-guided localisation by labelling the Tc toxins with gold fiducials. Gold beads can be easily identified in electron microscopy images, due to their high electron density. Initially, we added biotin-coated 10 nm gold beads to the intoxication mixture to be endocytosed, as described in other studies. This results in dark, prominent spots in both the SEM and TEM images, which should facilitate the localisation of Tc toxins in the final reconstructed tomogram.

However, the resulting tomograms showed dense clusters of fiducials, despite us not detecting any Tc toxins. The most likely explanation is that the biotin-coated gold particles oligomerize preferentially and are therefore not taken up by the cells homogeneously, but rather in clusters. This may cause excessive scattering, making it difficult to detect the Tc toxins in this mixture, which could explain why we did not detect any. In addition, the clustering behaviour means that uptake into endosomal vesicles is not evenly distributed, which could explain why we missed the correct spots.

To improve the process, we attempted to optimise the labelling of the toxin using click chemistry. To this end, we used 1.4 nm monomaleimido- and sulfo-NHS-nanogold to link the nanogold to the toxin chemically. Also, the smaller diameter of the gold particles should reduce their influence on the resulting contrast. Initially, we intended to use Tc toxins labelled with both fluorescent dyes and gold particles to allow for a rough correlation via CLEM. However, we noticed that labelling the Tc toxins with both labels (fluorophores and gold) resulted in quenching of the fluorescent signal. To avoid this, we decided to label two batches of the toxin individually and add a mixture of gold-labelled and fluorescently labelled Tc toxins to the cells during the intoxication step. Despite all optimisations, we were still unable to detect gold particles during FIB milling. This is most likely caused by the lower pixel size in the SEM setup compared to the TEM (~4–10 nm/pixel), which might fail to detect individual gold spots. One way to solve this would be to use larger gold labels, which, however, would first need to be generated in-house, as commercially available larger versions varied significantly in size and orientation. An alternative option is to detect the gold signal via high-resolution transmission electron microscopy (HRTEM); however, the sample would no longer be usable for standard TEM imaging due to the high exposure and resulting radiation damage. Therefore, the best option was to increase the resolution during the FIB-SEM procedure.

7.3.6 Insights into cellular architecture using cryo-volume imaging

To increase the likelihood of detecting the nanogold signal during the SEM stage, we employed cryo-volume imaging, an emerging method used for visualization during the milling process [159]. Unlike FIB milling, where thin sheets of material (lamellae) are generated that can later be imaged in a TEM, resulting in a loss of the majority of the sample, volume imaging uses the scanning function of a scanning electron microscope to ablate layers of the region of interest which can sequentially be imaged and aligned with each other, therefore sampling the whole specimen.

Unlike a standard data acquisition in a TEM, the detectors used for this purpose typically monitor either secondary electrons (SE), which are ideal for detecting biological specimens, or backscattered electrons (BSE), which are suitable for detecting heavy atoms, such as gold molecules. Combining this approach with motion-corrected image optimization (as described in section 6.2) leads to higher resolution and the detection of gold particles while slicing through a whole block of sample (e.g., whole cells) (Figure 34).

This enabled us to track cellular features throughout the cells while also obtaining information about the number of heavy metals present inside them. Although we were able to detect biological features in SE mode and coinciding features in BSE mode, which were concentrated around the periphery of the cells in line with endosomal entry, we were unable to identify Tc toxins in the resulting tomograms. This suggests that either we did not image the correct position or that our TEM imaging is suboptimal for visualizing Tc toxins within cells.

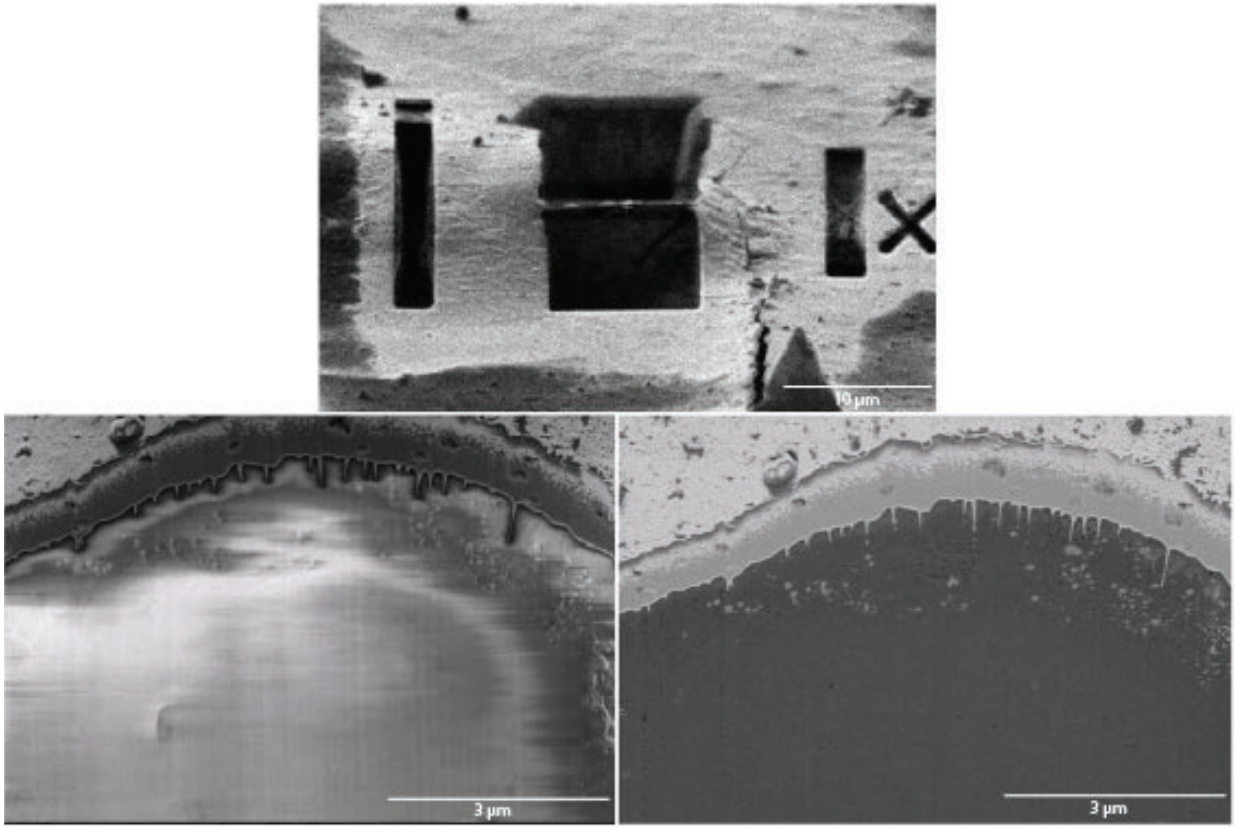

Figure 34: Cryo volume imaging with gold-labeled Tc toxins
(Upper panel) Milled lamella after cryo-electron volume imaging
(lower panel) Volume imaging results using secondary electrons (left panel) and back-scattering electrons (right panel).

7.3.7 Concluding Discussion

All in all, we have successfully established an fluorescent reporter system to track endosomal maturation, which, together with fluorescently labelled Tc toxins, allows us to monitor their entry into cells. However, mainly due to hardware and software limitations, we have yet to identify Tc toxins in any of the acquired tomograms. A possible explanation for this is the difficult 3D correlation between fluorescent signals and electron images in an SEM setup.

Not only is the detected fluorescent signal dispersed due to the thickness of the sample and the reflection of ice, but the position and angle at which both images are acquired also differ, leading to distortion and reduced resolution, which hinders localization. An increasing number of software tools aim to tackle these challenges and may enhance tomography data. However, at the moment they all rely on the addition of fluorescent beads prior to freezing to have defined signal spots for estimating distortion on the grid surface. The bead application to grids is not compatible with our protocol for growing cells on them, infecting them with the baculovirus, and subsequently with the Tc toxins (see Chapter 6.2 for more details).

Neither is it possible to apply the beads after the cells on grids due to the fixation treatment being lethal to the cells; additionally, they might end up on top of the cells, biasing the correction estimation. Nor is it possible to do it the other way around since the cells still proliferate during the 2-3 days of preparation time and therefore either engulf the beads or push them to the edges, once more biasing the calculations. For the CLEM procedure to work correctly, either the hardware of the fluorescent microscope must be improved to enhance spatial resolution and avoid ice reflection and similar effects that influence the z-correlation, or the software options to correct for these errors need to be improved.

Another central limitation of *in situ* tomography in general is the weak contrast of biological samples, which makes it difficult to localize specific features in a crowded environment. Given the enormous size of Tc toxins, they should be recognizable in tomograms, but it is still possible to miss them due to the weak contrast. To address these issues, either improvements in detectors or software optimization might be necessary. The picking tools used during this thesis – crYOLO and TomoTwin - already have a high success rate at identifying bigger proteins and complexes, but struggle to perform consistently in membranous environments. However, the underlying encoder and decoder principle (for TomoTwin) provides the basis for even identifying targets that would be difficult to spot for the human eye [156]. With ongoing improvements in that direction, weaker contrasts might no longer be a limitation.

A high-throughput approach to imaging the cell periphery without sample milling has not yet been successful, potentially because most endosomal vesicles are located closer to the cell centre, reducing the likelihood of hits. Our attempt to counter this by using Galactin-8 as an extracellular matrix to allow cells to stretch out further and thinner has not yet yielded positive results.

Once more, this might be a matter of chance or related to the fact that Galactin-8 treatment mimics a cancer-like state, causing unaccounted cellular responses concerning endosomal uptake and maturation[160, 161]. Additionally, combining these cells with attempts to detect gold fiducials linked to Tc toxins was unsuccessful, likely due to detector limitations (1.4 nm is generally less than 1 pixel), potential gold label aggregation, or an unaccounted cross-reaction between Galectin-induced changes and the gold labels.

The most promising results so far have been obtained using cryo-volume imaging, which enables the sampling of the whole cell body. This approach, combined with fiducial-based tracking, allowed us to identify fiducials inside the cell body. In conjunction with targeted TEM imaging, this method is expected to enhance the identification of toxins. However, due to the labour-intensive setup and the still-prototype nature of the system, we have not yet fully implemented

this method. Further optimization of the detectors (both SE and BSE), as well as different imaging voltages and acceleration voltages, might further enhance image quality. Additionally, improvements in image processing on a software level could help advance the current state of the art.

Alternatively, the biological sample could be optimized, for example, by generating larger constructs (adding additional fragments) to enhance size and, ideally, the resulting signal in cryo-ET. This, in turn, however, might also impede their function and a proper uptake. As proof of principle, it should also be possible to use chemicals, such as dynasore, that arrest endosomal import during intoxication [162]. Those samples would then confine the area in which the Tc toxins could potentially be trapped.

In conclusion, while cryo-electron tomography has experienced revolutionary advances in recent years, challenges remain in areas such as 3D correlation, particle picking in low-quality or crowded tomograms, and volume imaging. Improvements in hardware and software are still necessary to reach their full potential. As these technical barriers are overcome, and building on the foundation established by this work, structural analysis of Tc toxins inside cells will become feasible, offering new insights into receptor complex formation, acidic environment, and other open questions.

8 References

1. Granato, E.T., T.A. Meiller-Legrand, and K.R. Foster, *The Evolution and Ecology of Bacterial Warfare.* Current Biology, 2019. **29**(11): p. R521-R537.
2. Waterfield, N.R., T. Ciche, and D. Clarke, *Photorhabdus and a Host of Hosts.* Annual Review of Microbiology, 2009. **63**(Volume 63, 2009): p. 557-574.
3. Boemare, N.E., R.J. Akhurst, and R.G. Mourant, *DNA Relatedness between Xenorhabdus spp. (Enterobacteriaceae), Symbiotic Bacteria of Entomopathogenic Nematodes, and a Proposal To Transfer Xenorhabdus luminescens to a New Genus, Photorhabdus gen. nov.* International Journal of Systematic and Evolutionary Microbiology, 1993. **43**(2): p. 249-255.
4. Akhurst, R.J. and N.E. Boemare, *A Non-luminescent Strain of Xenorhabdus luminescens (Enterobacteriaceae).* Microbiology, 1986. **132**(7): p. 1917-1922.
5. Goodrich-Blair, H. and D.J. Clarke, *Mutualism and pathogenesis in Xenorhabdus and Photorhabdus: two roads to the same destination.* Molecular Microbiology, 2007. **64**(2): p. 260-268.
6. Clarke, D.J., *Photorhabdus: a model for the analysis of pathogenicity and mutualism.* Cellular Microbiology, 2008. **10**(11): p. 2159-2167.
7. Forst, S., et al., *XENORHABDUS AND PHOTORHABDUS SPP.: Bugs That Kill Bugs.* Annual Review of Microbiology, 1997. **51**(Volume 51, 1997): p. 47-72.
8. Waterfield, N.R., et al., *The tc genes of Photorhabdus: a growing family.* Trends in Microbiology, 2001. **9**(4): p. 185-191.
9. Daborn, P.J., et al., *A single Photorhabdus gene, makes caterpillars floppy (mcf), allows Escherichia coli to persist within and kill insects.* Proceedings of the National Academy of Sciences, 2002. **99**(16): p. 10742-10747.
10. Gulsen, S.H., et al., *Antiprotozoal activity of different Xenorhabdus and Photorhabdus bacterial secondary metabolites and identification of bioactive compounds using the easyPACId approach.* Scientific Reports, 2022. **12**(1): p. 10779.
11. Johnigk, S.-A. and R.-U. Ehlers, *Endotokia matricida in hermaphrodites of Heterorhabditis spp. and the effect of the food supply.* Nematology, 1999. **1**(7): p. 717-726.
12. Eckstein, S., et al., *Phenotypic Heterogeneity of the Insect Pathogen Photorhabdus luminescens: Insights into the Fate of Secondary Cells.* Applied and Environmental Microbiology, 2019. **85**(22): p. e01910-19.
13. Hussa, E.A. and H. Goodrich-Blair, *It Takes a Village: Ecological and Fitness Impacts of Multipartite Mutualism.* Annual Review of Microbiology, 2013. **67**(Volume 67, 2013): p. 161-178.
14. Meusch, D., et al., *Mechanism of Tc toxin action revealed in molecular detail.* Nature, 2014. **508**(7494): p. 61-5.
15. Bowen, D., et al., *Insecticidal Toxins from the Bacterium Photorhabdus luminescens.* Science, 1998. **280**(5372): p. 2129-2132.
16. Belyy, A., et al., *Structure and activation mechanism of the Makes caterpillars floppy 1 toxin.* Nat Commun, 2023. **14**(1): p. 8226.
17. Yang, G., et al., *Photorhabdus virulence cassettes confer injectable insecticidal activity against the wax moth.* J Bacteriol, 2006. **188**(6): p. 2254-61.
18. Schubert, E., et al., *Membrane insertion of α-xenorhabdolysin in near-atomic detail.* eLife, 2018. **7**: p. e38017.
19. Ribeiro, C., M. Vignes, and M. Brehélin, *Xenorhabdus nematophila (Enterobacteriacea) Secretes a Cation-selective Calcium-independent Porin Which*

*Causes Vacuolation of the Rough Endoplasmic Reticulum and Cell Lysis *.* Journal of Biological Chemistry, 2003. **278**(5): p. 3030-3039.
20. Waterfield, N.R., et al., *Rapid Virulence Annotation (RVA): Identification of virulence factors using a bacterial genome library and multiple invertebrate hosts.* Proceedings of the National Academy of Sciences, 2008. **105**(41): p. 15967-15972.
21. Hurst, M.R.H., et al., *Yersinia entomophaga sp. nov., isolated from the New Zealand grass grub Costelytra zealandica.* International Journal of Systematic and Evolutionary Microbiology, 2011. **61**(4): p. 844-849.
22. Hurst, M.R., et al., *The main virulence determinant of Yersinia entomophaga MH96 is a broad-host-range toxin complex active against insects.* J Bacteriol, 2011. **193**(8): p. 1966-80.
23. Landsberg, M.J., et al., *3D structure of the Yersinia entomophaga toxin complex and implications for insecticidal activity.* Proceedings of the National Academy of Sciences, 2011. **108**(51): p. 20544-20549.
24. Sitsel, O., et al., *Yersinia entomophaga Tc toxin is released by T10SS-dependent lysis of specialized cell subpopulations.* Nat Microbiol, 2024. **9**(2): p. 390-404.
25. Feldmüller, M., et al., *Stepwise assembly and release of Tc toxins from Yersinia entomophaga.* Nature Microbiology, 2024. **9**(2): p. 405-420.
26. Hurst Mark, R.H., et al., *Plasmid-Located Pathogenicity Determinants of Serratia entomophila, the Causal Agent of Amber Disease of Grass Grub, Show Similarity to the Insecticidal Toxins of Photorhabdus luminescens.* Journal of Bacteriology, 2000. **182**(18): p. 5127-5138.
27. Busby, J.N., et al., *Structural Analysis of Chi1 Chitinase from Yen-Tc: The Multisubunit Insecticidal ABC Toxin Complex of Yersinia entomophaga.* Journal of Molecular Biology, 2012. **415**(2): p. 359-371.
28. Peraro, M.D. and F.G. van der Goot, *Pore-forming toxins: ancient, but never really out of fashion.* Nature Reviews Microbiology, 2016. **14**(2): p. 77-92.
29. Los Ferdinand, C.O., et al., *Role of Pore-Forming Toxins in Bacterial Infectious Diseases.* Microbiology and Molecular Biology Reviews, 2013. **77**(2): p. 173-207.
30. Iacovache, I., F.G. van der Goot, and L. Pernot, *Pore formation: An ancient yet complex form of attack.* Biochimica et Biophysica Acta (BBA) - Biomembranes, 2008. **1778**(7): p. 1611-1623.
31. Gilbert, R.J.C., *Pore-forming toxins.* Cellular and Molecular Life Sciences, 2002. **59**(5): p. 832-844.
32. Benke, S., et al., *The assembly dynamics of the cytolytic pore toxin ClyA.* Nature Communications, 2015. **6**(1): p. 6198.
33. Wallace, A.J., et al., *E. coli Hemolysin E (HlyE, ClyA, SheA): X-Ray Crystal Structure of the Toxin and Observation of Membrane Pores by Electron Microscopy.* Cell, 2000. **100**(2): p. 265-276.
34. Eifler, N., et al., *Cytotoxin ClyA from Escherichia coli assembles to a 13‐meric pore independent of its redox‐state.* The EMBO Journal, 2006. **25**(11): p. 2652-2661-2661.
35. Ribeiro, C., M. Vignes, and M. Brehélin, *Xenorhabdus nematophila (enterobacteriacea) secretes a cation-selective calcium-independent porin which causes vacuolation of the rough endoplasmic reticulum and cell lysis.* J Biol Chem, 2003. **278**(5): p. 3030-9.
36. Vigneux, F., et al., *The xaxAB Genes Encoding a New Apoptotic Toxin from the Insect Pathogen Xenorhabdus nematophila Are Present in Plant and*

*Human Pathogens *.* Journal of Biological Chemistry, 2007. **282**(13): p. 9571-9580.
37. Zhang, X., et al., *XaxAB-like binary toxin from Photorhabdus luminescens exhibits both insecticidal activity and cytotoxicity.* FEMS Microbiology Letters, 2014. **350**(1): p. 48-56.
38. Tweten Rodney, K., *Cholesterol-Dependent Cytolysins, a Family of Versatile Pore-Forming Toxins.* Infection and Immunity, 2005. **73**(10): p. 6199-6209.
39. Gilbert, R.J.C., *Inactivation and Activity of Cholesterol-Dependent Cytolysins: What Structural Studies Tell Us.* Structure, 2005. **13**(8): p. 1097-1106.
40. Song, L., et al., *Structure of Staphylococcal α-Hemolysin, a Heptameric Transmembrane Pore.* Science, 1996. **274**(5294): p. 1859-1865.
41. Iacovache, I., M. Bischofberger, and F.G. van der Goot, *Structure and assembly of pore-forming proteins.* Current Opinion in Structural Biology, 2010. **20**(2): p. 241-246.
42. Ezekwe, E.A.D., C. Weng, and J.A. Duncan, *ADAM10 Cell Surface Expression but Not Activity Is Critical for Staphylococcus aureus α-Hemolysin-Mediated Activation of the NLRP3 Inflammasome in Human Monocytes.* Toxins, 2016. **8**(4): p. 95.
43. Smith, H. and J. Keppie, *Observations on Experimental Anthrax: Demonstration of a Specific Lethal Factor produced in vivo by Bacillus anthracis.* Nature, 1954. **173**(4410): p. 869-870.
44. Young, J.A.T. and R.J. Collier, *Anthrax Toxin: Receptor Binding, Internalization, Pore Formation, and Translocation.* Annual Review of Biochemistry, 2007. **76**(Volume 76, 2007): p. 243-265.
45. Goodsell, D. *Molecule of the Month: Anthrax Toxin*. April 2002.
46. Tonello, F., P. Ascenzi, and C. Montecucco, *The Metalloproteolytic Activity of the Anthrax Lethal Factor Is Substrate-inhibited*.* Journal of Biological Chemistry, 2003. **278**(41): p. 40075-40078.
47. Hammond, S.E. and P.C. Hanna, *Lethal Factor Active-Site Mutations Affect Catalytic Activity In Vitro.* Infection and Immunity, 1998. **66**(5): p. 2374-2378.
48. Leppla, S.H., *Anthrax toxin edema factor: a bacterial adenylate cyclase that increases cyclic AMP concentrations of eukaryotic cells.* Proceedings of the National Academy of Sciences, 1982. **79**(10): p. 3162-3166.
49. Kumar, P., N. Ahuja, and R. Bhatnagar, *Anthrax Edema Toxin Requires Influx of Calcium for Inducing Cyclic AMP Toxicity in Target Cells.* Infection and Immunity, 2002. **70**(9): p. 4997-5007.
50. Dal Molin, F., et al., *Cell entry and cAMP imaging of anthrax edema toxin.* The EMBO Journal, 2006. **25**(22): p. 5405-5413-5413.
51. Bann, J.G., *Anthrax toxin protective antigen--insights into molecular switching from prepore to pore.* Protein Sci, 2012. **21**(1): p. 1-12.
52. Jiang, J., et al., *Atomic structure of anthrax protective antigen pore elucidates toxin translocation.* Nature, 2015. **521**(7553): p. 545-549.
53. Pilpa, R.M., et al., *A Receptor-based Switch that Regulates Anthrax Toxin Pore Formation.* PLOS Pathogens, 2011. **7**(12): p. e1002354.
54. Hardenbrook, N.J., et al., *Atomic structures of anthrax toxin protective antigen channels bound to partially unfolded lethal and edema factors.* Nature Communications, 2020. **11**(1): p. 840.
55. Schnepf, E., et al., *Bacillus thuringiensis and Its Pesticidal Crystal Proteins.* Microbiology and Molecular Biology Reviews, 1998. **62**(3): p. 775-806.
56. Xu, C., et al., *Structural Insights into Bacillus thuringiensis Cry, Cyt and Parasporin Toxins.* Toxins, 2014. **6**(9): p. 2732-2770.

57. Jurat-Fuentes, J.L., D.G. Heckel, and J. Ferré, *Mechanisms of Resistance to Insecticidal Proteins from Bacillus thuringiensis.* Annual Review of Entomology, 2021. **66**(Volume 66, 2021): p. 121-140.
58. Vecchio, A.J., S.S. Rathnayake, and R.M. Stroud, *Structural basis for Clostridium perfringens enterotoxin targeting of claudins at tight junctions in mammalian gut.* Proceedings of the National Academy of Sciences, 2021. **118**(15): p. e2024651118.
59. Nagarajan, S.K., et al., *C. perfringens enterotoxin-claudin pore complex: Models for structure, mechanism of pore assembly and cation permeability.* Computational and Structural Biotechnology Journal, 2025. **27**: p. 287-306.
60. Bräuning, B., et al., *Structure and mechanism of the two-component α-helical pore-forming toxin YaxAB.* Nature Communications, 2018. **9**(1): p. 1806.
61. Law, R.H.P., et al., *The structural basis for membrane binding and pore formation by lymphocyte perforin.* Nature, 2010. **468**(7322): p. 447-451.
62. Serna, M., et al., *Structural basis of complement membrane attack complex formation.* Nature Communications, 2016. **7**(1): p. 10587.
63. Anderluh, G. and J.H. Lakey, *Disparate proteins use similar architectures to damage membranes.* Trends in Biochemical Sciences, 2008. **33**(10): p. 482-490.
64. Cao, C., et al., *Single-molecule sensing of peptides and nucleic acids by engineered aerolysin nanopores.* Nature Communications, 2019. **10**(1): p. 4918.
65. Aziz, U.B.A., et al., *Targeted small molecule inhibitors blocking the cytolytic effects of pneumolysin and homologous toxins.* Nature Communications, 2024. **15**(1): p. 3537.
66. Pantaleo, G., et al., *Antibodies to combat viral infections: development strategies and progress.* Nature Reviews Drug Discovery, 2022. **21**(9): p. 676-696.
67. Albrecht Mark, T., et al., *Human Monoclonal Antibodies against Anthrax Lethal Factor and Protective Antigen Act Independently To Protect against Bacillus anthracis Infection and Enhance Endogenous Immunity to Anthrax.* Infection and Immunity, 2007. **75**(11): p. 5425-5433.
68. Roderer, D. and S. Raunser, *Tc Toxin Complexes: Assembly, Membrane Permeation, and Protein Translocation.* Annu Rev Microbiol, 2019. **73**: p. 247-265.
69. Song, N., et al., *Genome-wide dissection reveals diverse pathogenic roles of bacterial Tc toxins.* PLoS Pathog, 2021. **17**(2): p. e1009102.
70. Ffrench-Constant, R. and N. Waterfield, *An ABC Guide to the Bacterial Toxin Complexes.* Adv Appl Microbiol, 2005. **58c**: p. 169-183.
71. Spinner, J.L., et al., *Yersinia pestis insecticidal-like toxin complex (Tc) family proteins: characterization of expression, subcellular localization, and potential role in infection of the flea vector.* BMC Microbiol, 2012. **12**: p. 296.
72. Gendlina, I., et al., *Identification and type III-dependent secretion of the Yersinia pestis insecticidal-like proteins.* Molecular Microbiology, 2007. **64**(5): p. 1214-1227.
73. Hurst Mark, R.H., et al., *Temperature-Dependent Galleria mellonella Mortality as a Result of Yersinia entomophaga Infection.* Applied and Environmental Microbiology, 2015. **81**(18): p. 6404-6414.
74. Aleksandrova, N.A., et al., *Recent insights into mechanisms of cellular toxicity and cell recognition associated with the ABC family of pore-forming toxins.* Biochemical Society Transactions, 2023. **51**(3): p. 1235-1244.
75. Leidreiter, F., et al., *Common architecture of Tc toxins from human and insect pathogenic bacteria.* Science Advances, 2019. **5**(10): p. eaax6497.
76. Roderer, D., et al., *Structure of a Tc holotoxin pore provides insights into the translocation mechanism.* Proceedings of the National Academy of Sciences, 2019. **116**(46): p. 23083-23090.

77. Gatsogiannis, C., et al., *Membrane insertion of a Tc toxin in near-atomic detail.* Nat Struct Mol Biol, 2016. **23**(10): p. 884-890.
78. Landsberg, M.J., et al., *3D structure of the Yersinia entomophaga toxin complex and implications for insecticidal activity.* Proceedings of the National Academy of Sciences, 2011. **108**(51): p. 20544-20549.
79. Piper, S.J., et al., *Cryo-EM structures of the pore-forming A subunit from the Yersinia entomophaga ABC toxin.* Nature Communications, 2019. **10**(1): p. 1952.
80. Roderer, D., et al., *Glycan-dependent cell adhesion mechanism of Tc toxins.* Nature Communications, 2020. **11**(1): p. 2694.
81. Ng'ang'a, P.N., et al., *Involvement of N-glycans in binding of Photorhabdus luminescens Tc toxin.* Cellular Microbiology, 2021. **23**(8): p. e13326.
82. Song, N., et al., *N-Glycans and sulfated glycosaminoglycans contribute to the action of diverse Tc toxins on mammalian cells.* PLOS Pathogens, 2021. **17**(2): p. e1009244.
83. Xu, Y., et al., *CRISPR screens in Drosophila cells identify Vsg as a Tc toxin receptor.* Nature, 2022. **610**(7931): p. 349-355.
84. Taylor, W.R., *A deeply knotted protein structure and how it might fold.* Nature, 2000. **406**(6798): p. 916-919.
85. Taylor, W.R. and K. Lin, *Protein knots: A tangled problem.* Nature, 2003. **421**(6918): p. 25-25.
86. Gatsogiannis, C., et al., *A syringe-like injection mechanism in Photorhabdus luminescens toxins.* Nature, 2013. **495**(7442): p. 520-523.
87. Jackson, V.A., et al., *Structures of Teneurin adhesion receptors reveal an ancient fold for cell-cell interaction.* Nature Communications, 2018. **9**(1): p. 1079.
88. Gatsogiannis, C., et al., *Tc toxin activation requires unfolding and refolding of a β-propeller.* Nature, 2018. **563**(7730): p. 209-213.
89. Roderer, D., et al., *Towards the application of Tc toxins as a universal protein translocation system.* Nature Communications, 2019. **10**(1): p. 5263.
90. Ng'ang'a, P.N., et al., *Multistate kinetics of the syringe-like injection mechanism of Tc toxins.* Science Advances, 2025. **11**(1): p. eadr2019.
91. Lang, A.E., et al., *Photorhabdus luminescens Toxins ADP-Ribosylate Actin and RhoA to Force Actin Clustering.* Science, 2010. **327**(5969): p. 1139-1142.
92. Belyy, A., et al., *Mechanism of threonine ADP-ribosylation of F-actin by a Tc toxin.* Nature Communications, 2022. **13**(1): p. 4202.
93. Lang, A.E., et al., *Actin ADP-ribosylation at Threonine148 by Photorhabdus luminescens toxin TccC3 induces aggregation of intracellular F-actin.* Cellular Microbiology, 2017. **19**(1): p. e12636.
94. Dong, S., et al., *Photorhabdus luminescens TccC3 Toxin Targets the Dynamic Population of F-Actin and Impairs Cell Cortex Integrity.* Int J Mol Sci, 2022. **23**(13).
95. Sitsel, O., et al., *Yersinia entomophaga Tc toxin is released by T10SS-dependent lysis of specialized cell subpopulations.* Nature Microbiology, 2024.
96. Kreitz, J., et al., *Programmable protein delivery with a bacterial contractile injection system.* Nature, 2023. **616**(7956): p. 357-364.
97. Deamer, D., M. Akeson, and D. Branton, *Three decades of nanopore sequencing.* Nature Biotechnology, 2016. **34**(5): p. 518-524.
98. Wang, Y., et al., *Nanopore sequencing technology, bioinformatics and applications.* Nature Biotechnology, 2021. **39**(11): p. 1348-1365.
99. Glare, T., et al., *Have biopesticides come of age?* Trends in Biotechnology, 2012. **30**(5): p. 250-258.

100. Rani, A.T., et al., *Biopesticides: An Alternative to Synthetic Insecticides*, in *Microbial Technology for Sustainable Environment*, P. Bhatt, et al., Editors. 2021, Springer Singapore: Singapore. p. 439-466.
101. Kühlbrandt, W., *The Resolution Revolution.* Science, 2014. **343**(6178): p. 1443-1444.
102. Cheng, Y., *Single-particle cryo-EM—How did it get here and where will it go.* Science, 2018. **361**(6405): p. 876-880.
103. Nogales, E., *The development of cryo-EM into a mainstream structural biology technique.* Nature Methods, 2016. **13**(1): p. 24-27.
104. Frank, J., *Single-Particle Imaging of Macromolecules by Cryo-Electron Microscopy.* Annual Review of Biophysics, 2002. **31**(Volume 31, 2002): p. 303-319.
105. Beck, M. and W. Baumeister, *Cryo-Electron Tomography: Can it Reveal the Molecular Sociology of Cells in Atomic Detail?* Trends in Cell Biology, 2016. **26**(11): p. 825-837.
106. Turk, M. and W. Baumeister, *The promise and the challenges of cryo-electron tomography.* FEBS Letters, 2020. **594**(20): p. 3243-3261.
107. Scheres, S.H.W., *RELION: Implementation of a Bayesian approach to cryo-EM structure determination.* Journal of Structural Biology, 2012. **180**(3): p. 519-530.
108. Punjani, A., et al., *cryoSPARC: algorithms for rapid unsupervised cryo-EM structure determination.* Nature Methods, 2017. **14**(3): p. 290-296.
109. Au - Moriya, T., et al., *High-resolution Single Particle Analysis from Electron Cryo-microscopy Images Using SPHIRE.* JoVE, 2017(123): p. e55448.
110. Yip, K.M., et al., *Atomic-resolution protein structure determination by cryo-EM.* Nature, 2020. **587**(7832): p. 157-161.
111. Küçükoğlu, B., et al., *Low-dose cryo-electron ptychography of proteins at sub-nanometer resolution.* Nature Communications, 2024. **15**(1): p. 8062.
112. Mahamid, J., et al., *Visualizing the molecular sociology at the HeLa cell nuclear periphery.* Science, 2016. **351**(6276): p. 969-972.
113. Wan, W. and J.A.G. Briggs, *Chapter Thirteen - Cryo-Electron Tomography and Subtomogram Averaging*, in *Methods in Enzymology*, R.A. Crowther, Editor. 2016, Academic Press. p. 329-367.
114. Wang, Z., et al., *Structures from intact myofibrils reveal mechanism of thin filament regulation through nebulin.* Science, 2022. **375**(6582): p. eabn1934.
115. de Boer, P., J.P. Hoogenboom, and B.N.G. Giepmans, *Correlated light and electron microscopy: ultrastructure lights up!* Nature Methods, 2015. **12**(6): p. 503-513.
116. Pierson, J.A., J.E. Yang, and E.R. Wright, *Recent advances in correlative cryo-light and electron microscopy.* Current Opinion in Structural Biology, 2024. **89**: p. 102934.
117. Bykov, Y.S., et al., *Correlative light and electron microscopy methods for the study of virus–cell interactions.* FEBS Letters, 2016. **590**(13): p. 1877-1895.
118. VAN HEST, J.J.H.A., et al., *Towards robust and versatile single nanoparticle fiducial markers for correlative light and electron microscopy.* Journal of Microscopy, 2019. **274**(1): p. 13-22.
119. Tegunov, D., et al., *Multi-particle cryo-EM refinement with M visualizes ribosome-antibiotic complex at 3.5 Å in cells.* Nature Methods, 2021. **18**(2): p. 186-193.
120. Tegunov, D. and P. Cramer, *Real-time cryo-electron microscopy data preprocessing with Warp.* Nature Methods, 2019. **16**(11): p. 1146-1152.
121. Berkamp, S., et al., *Correlative Light and Electron Cryo-Microscopy Workflow Combining Micropatterning, Ice Shield, and an In-Chamber Fluorescence Light Microscope.* Bio-protocol, 2023. **13**(24): p. e4901.
122. Tacke, S., et al., *A streamlined workflow for automated cryo focused ion beam milling.* Journal of Structural Biology, 2021. **213**(3): p. 107743.

123. Yang, J., et al., *Integrated Fluorescence Microscopy (iFLM) for Cryo-FIB-milling and In-situ Cryo-ET.* bioRxiv, 2023: p. 2023.07.11.548578.
124. Kukulski, W., et al., *Correlated fluorescence and 3D electron microscopy with high sensitivity and spatial precision.* Journal of Cell Biology, 2011. **192**(1): p. 111-119.
125. Stabrin, M., et al., *TranSPHIRE: automated and feedback-optimized on-the-fly processing for cryo-EM.* Nature Communications, 2020. **11**(1): p. 5716.
126. Zheng, S.Q., et al., *MotionCor2: anisotropic correction of beam-induced motion for improved cryo-electron microscopy.* Nature Methods, 2017. **14**(4): p. 331-332.
127. Rohou, A. and N. Grigorieff, *CTFFIND4: Fast and accurate defocus estimation from electron micrographs.* Journal of Structural Biology, 2015. **192**(2): p. 216-221.
128. Wagner, T., et al., *SPHIRE-crYOLO is a fast and accurate fully automated particle picker for cryo-EM.* Communications Biology, 2019. **2**(1): p. 218.
129. Kimanius, D., et al., *New tools for automated cryo-EM single-particle analysis in RELION-4.0.* Biochemical Journal, 2021. **478**(24): p. 4169-4185.
130. Punjani, A., H. Zhang, and D.J. Fleet, *Non-uniform refinement: adaptive regularization improves single-particle cryo-EM reconstruction.* Nature Methods, 2020. **17**(12): p. 1214-1221.
131. Zivanov, J., T. Nakane, and S.H.W. Scheres, *A Bayesian approach to beam-induced motion correction in cryo-EM single-particle analysis.* IUCrJ, 2019. **6**(1): p. 5-17.
132. Adams, P.D., et al., *PHENIX: a comprehensive Python-based system for macromolecular structure solution.* Acta Crystallographica Section D, 2010. **66**(2): p. 213-221.
133. Punjani, A. and D.J. Fleet, *3D variability analysis: Resolving continuous flexibility and discrete heterogeneity from single particle cryo-EM.* Journal of Structural Biology, 2021. **213**(2): p. 107702.
134. Jumper, J., et al., *Highly accurate protein structure prediction with AlphaFold.* Nature, 2021. **596**(7873): p. 583-589.
135. van Kempen, M., et al., *Fast and accurate protein structure search with Foldseek.* Nature Biotechnology, 2024. **42**(2): p. 243-246.
136. Pettersen, E.F., et al., *UCSF ChimeraX: Structure visualization for researchers, educators, and developers.* Protein Science, 2021. **30**(1): p. 70-82.
137. Emsley, P., et al., *Features and development of Coot.* Acta Crystallogr D Biol Crystallogr, 2010. **66**(Pt 4): p. 486-501.
138. Croll, T., *ISOLDE: a physically realistic environment for model building into low-resolution electron-density maps.* Acta Crystallographica Section D, 2018. **74**(6): p. 519-530.
139. Afonine, P.V., et al., *Real-space refinement in PHENIX for cryo-EM and crystallography.* Acta Crystallographica Section D, 2018. **74**(6): p. 531-544.
140. Krissinel, E. and K. Henrick, *Inference of macromolecular assemblies from crystalline state.* J Mol Biol, 2007. **372**(3): p. 774-97.
141. Abramson, J., et al., *Accurate structure prediction of biomolecular interactions with AlphaFold 3.* Nature, 2024. **630**(8016): p. 493-500.
142. Yang, Z., et al., *AlphaFold2 and its applications in the fields of biology and medicine.* Signal Transduction and Targeted Therapy, 2023. **8**(1): p. 115.
143. Dow, J.A.T., *pH gradients in lepidopteran midgut.* Journal of Experimental Biology, 1992. **172**(1): p. 355-375.
144. Lehane, M.J., *PERITROPHIC MATRIX STRUCTURE AND FUNCTION.* Annual Review of Entomology, 1997. **42**(Volume 42, 1997): p. 525-550.

145. Ma, E., et al., *Interaction of Viruses with the Insect Intestine.* Annual Review of Virology, 2021. **8**(Volume 8, 2021): p. 115-131.
146. Vandekerckhove, J., et al., *Clostridium perfringens iota toxin ADP-ribosylates skeletal muscle actin in Arg-177.* FEBS Letters, 1987. **225**(1-2): p. 48-52.
147. Buetow, L., et al., *Structure of the Rho-activating domain of Escherichia coli cytotoxic necrotizing factor 1.* Nature Structural Biology, 2001. **8**(7): p. 584-588.
148. Chaoprasid, P., et al., *Crystal structure of bacterial cytotoxic necrotizing factor CNF_Y reveals molecular building blocks for intoxication.* The EMBO Journal, 2021. **40**(4): p. e105202.
149. Chung, S.J., J.C. Fromme, and G.L. Verdine, *Structure of Human Cytidine Deaminase Bound to a Potent Inhibitor.* Journal of Medicinal Chemistry, 2005. **48**(3): p. 658-660.
150. Awais, M.M., et al., *Insights into midgut cell types and their crucial role in antiviral immunity in the lepidopteran model Bombyx mori.* Frontiers in Immunology, 2024. **Volume 15 - 2024**.
151. Kashimura, A., et al., *Protein A-Mouse Acidic Mammalian Chitinase-V5-His Expressed in Periplasmic Space of Escherichia coli Possesses Chitinase Functions Comparable to CHO-Expressed Protein.* PLOS ONE, 2013. **8**(11): p. e78669.
152. Macpherson, C.V., et al., *The untapped potential of cell culture in disentangling insect-microbial relationships.* Microbiome Res Rep, 2024. **3**(2): p. 20.
153. Doudna, J.A. and E. Charpentier, *The new frontier of genome engineering with CRISPR-Cas9.* Science, 2014. **346**(6213): p. 1258096.
154. Sari, D., et al., *The MultiBac Baculovirus/Insect Cell Expression Vector System for Producing Complex Protein Biologics*, in *Advanced Technologies for Protein Complex Production and Characterization*, M.C. Vega, Editor. 2016, Springer International Publishing: Cham. p. 199-215.
155. Wu, X.-S., et al., *Ca2+ and calmodulin initiate all forms of endocytosis during depolarization at a nerve terminal.* Nature Neuroscience, 2009. **12**(8): p. 1003-1010.
156. Rice, G., et al., *TomoTwin: generalized 3D localization of macromolecules in cryo-electron tomograms with structural data mining.* Nature Methods, 2023. **20**(6): p. 871-880.
157. Carter, S.D., et al., *Ribosome-associated vesicles: A dynamic subcompartment of the endoplasmic reticulum in secretory cells.* Science Advances, 2020. **6**(14): p. eaay9572.
158. Clark, Andrew G., K. Dierkes, and Ewa K. Paluch, *Monitoring Actin Cortex Thickness in Live Cells.* Biophysical Journal, 2013. **105**(3): p. 570-580.
159. Li, W., et al., *Differential cellular responses to adhesive interactions with galectin-8- and fibronectin-coated substrates.* Journal of Cell Science, 2021. **134**(8).
160. Hong, M.-H., et al., *Intracellular galectins sense cytosolically exposed glycans as danger and mediate cellular responses.* Journal of Biomedical Science, 2021. **28**(1): p. 16.
161. Purić, E., U.J. Nilsson, and M. Anderluh, *Galectin-8 inhibition and functions in immune response and tumor biology.* Medicinal Research Reviews, 2024. **44**(5): p. 2236-2265.
162. Preta, G., J.G. Cronin, and I.M. Sheldon, *Dynasore - not just a dynamin inhibitor.* Cell Communication and Signaling, 2015. **13**(1): p. 24.

9 Appendix

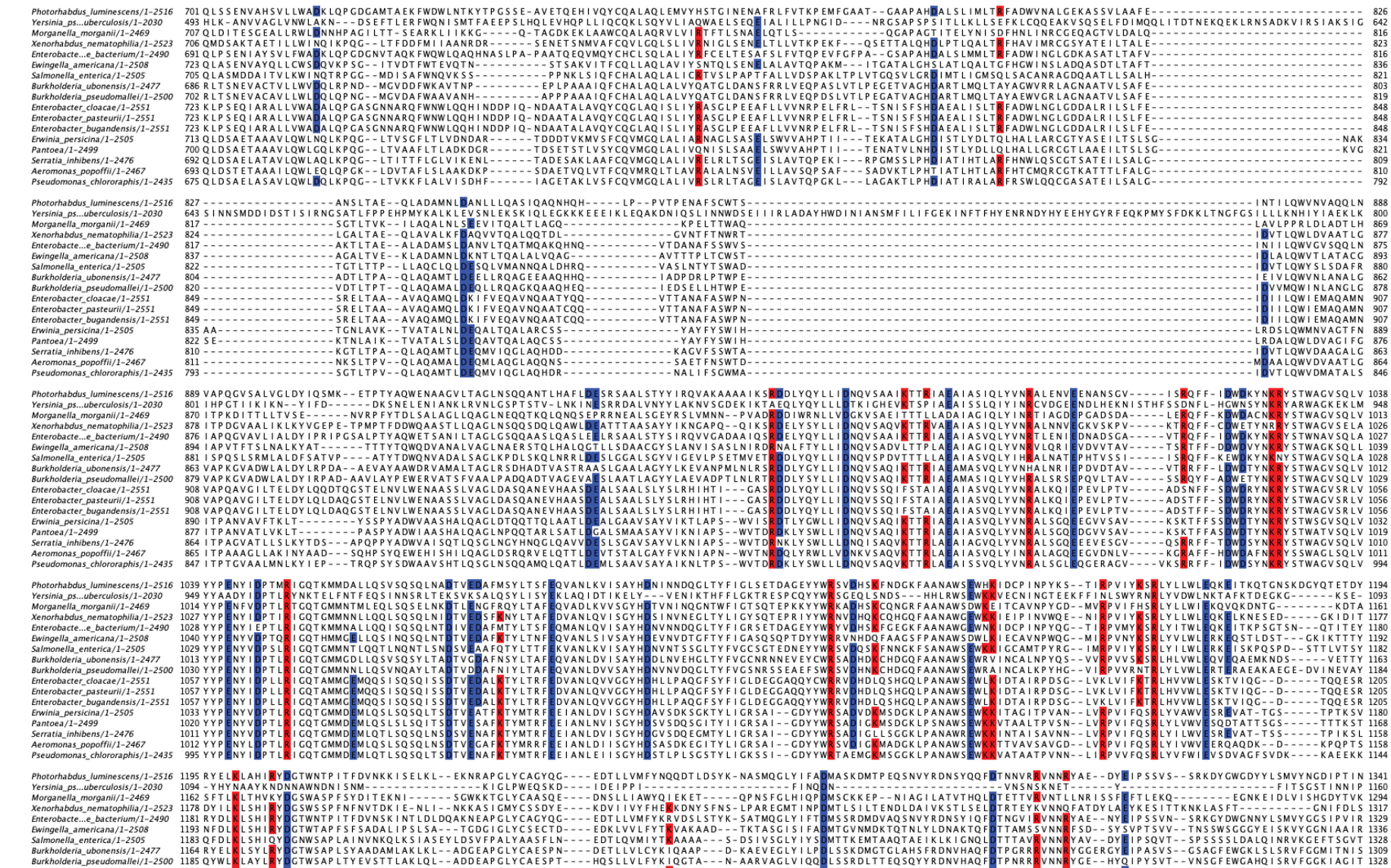
Photorhabdus_luminescens/1-2516
Yersinia_ps...uberculosis/1-2030
Morganella_morganii/1-2469
Xenorhabdus_nematophilia/1-2523
Enterobacte...e_bacterium/1-2490
Ewingella_americana/1-2508
Salmonella_enterica/1-2505
Burkholderia_ubonensis/1-2477
Burkholderia_pseudomallei/1-2500
Enterobacter_cloacae/1-2551
Enterobacter_pasteurii/1-2551
Enterobacter_bugandensis/1-2551
Erwinia_persicina/1-2505
Pantoea/1-2499
Serratia_inhibens/1-2476
Aeromonas_popoffii/1-2467
Pseudomonas_chlororaphis/1-2435

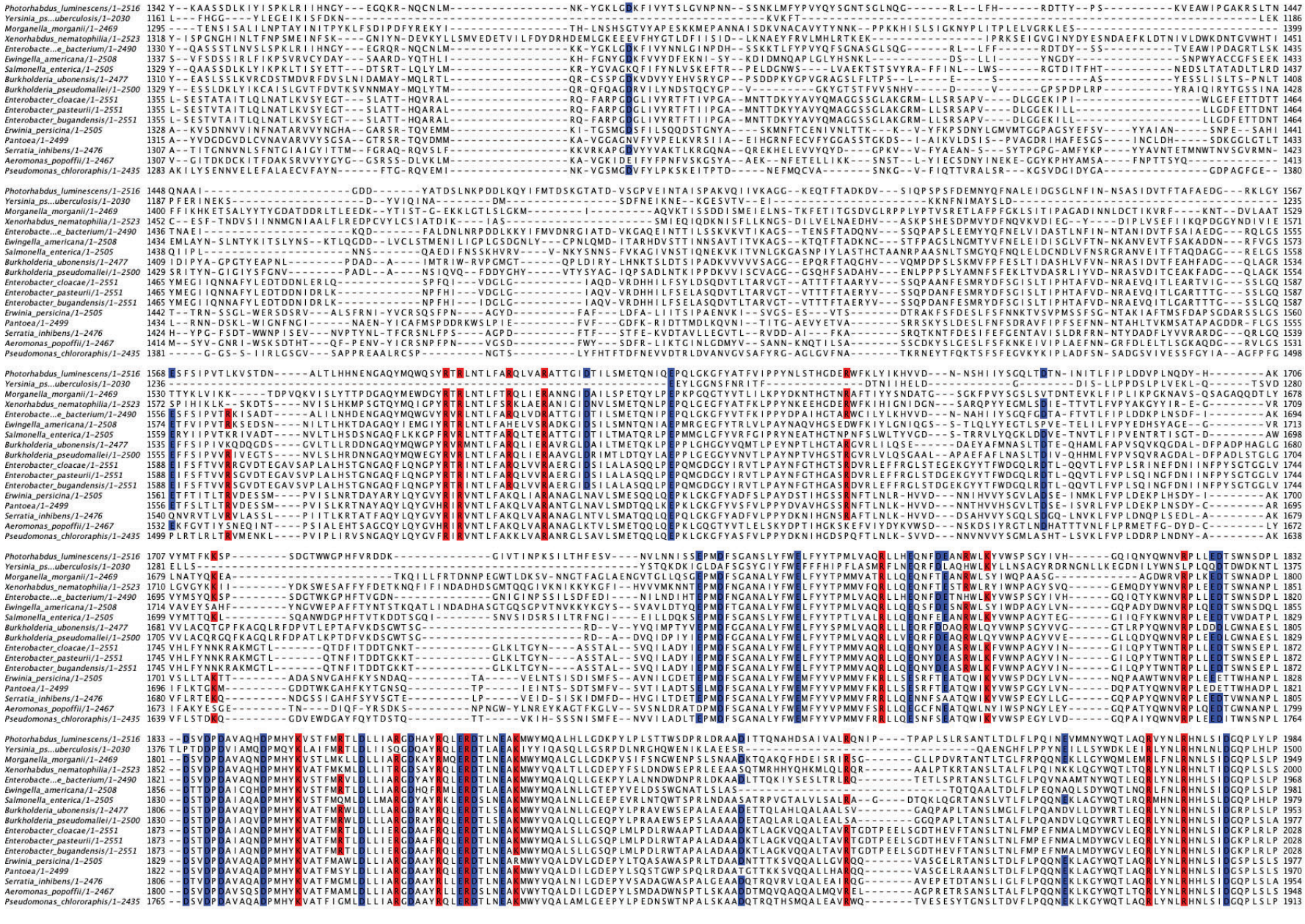

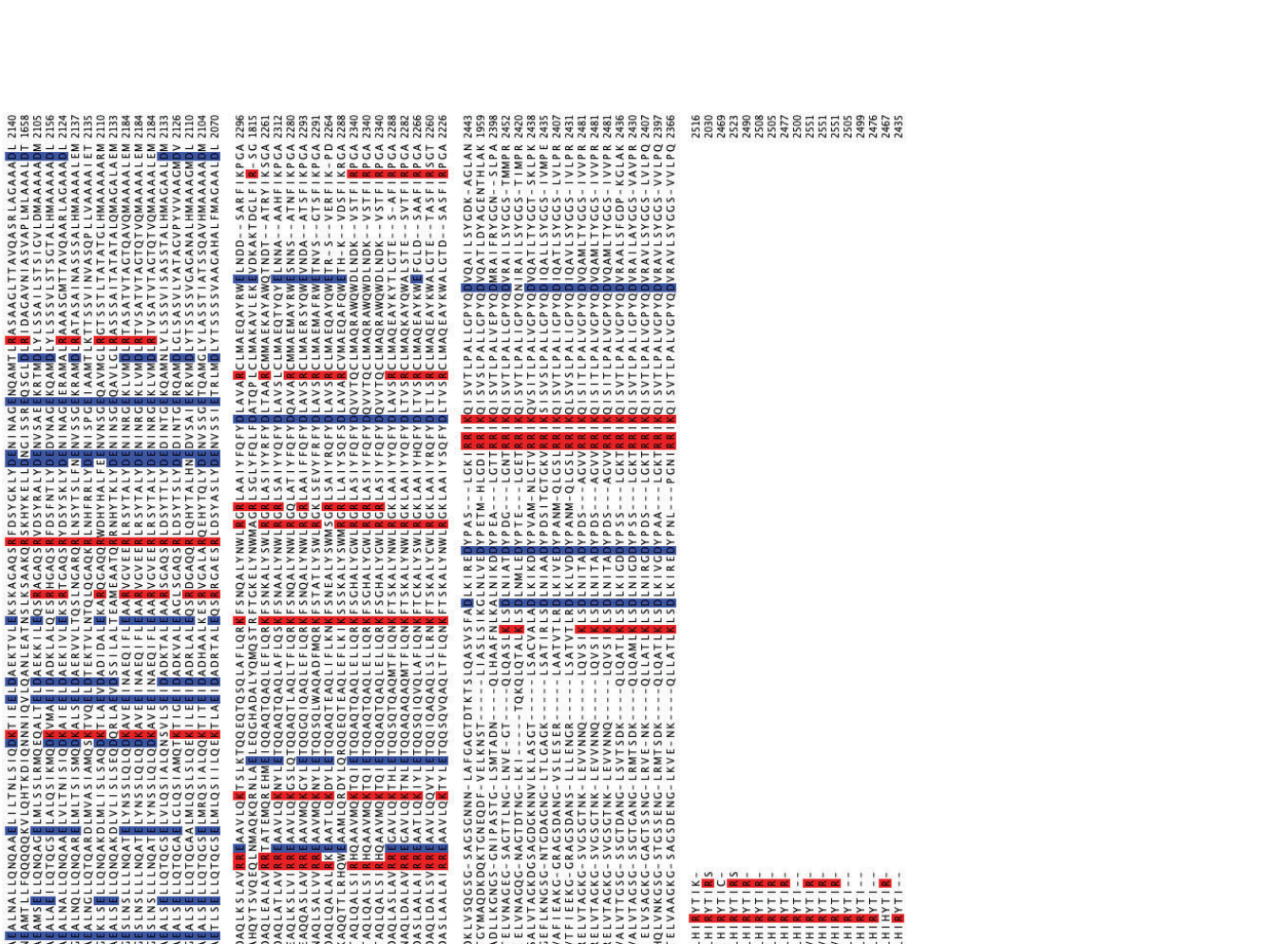

Figure S 1: Multiple Sequence Alignment (MSA) of Photorhabdus luminescens TcdA1 protein sequence with homologous Tc toxins

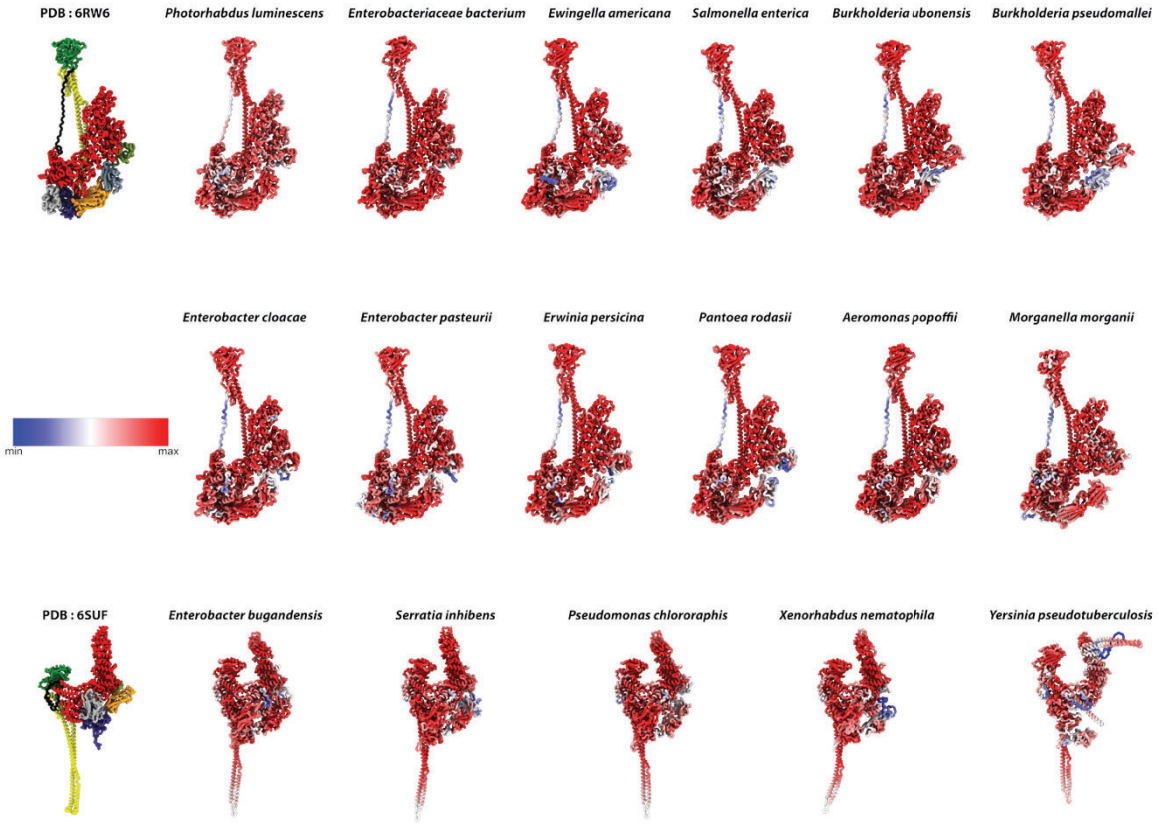

Figure S 2: High structural conservation of Tc toxins

AlphaFold3 predicted structural models for sequences used in the MSA reveal for all predictions a clear Tc toxin fold, either following the structure of the TcdA1 prepore state (PDB:6RW6) or the pore state (PDB:6SUF). Models are in their respective subclass (prepore or pore) sorted according to their position in the MSA. AlphaFold predicted structures are colored to the confidence threshold overwriting the b-factor values (red = highest confidence and blue = lowest confidence).

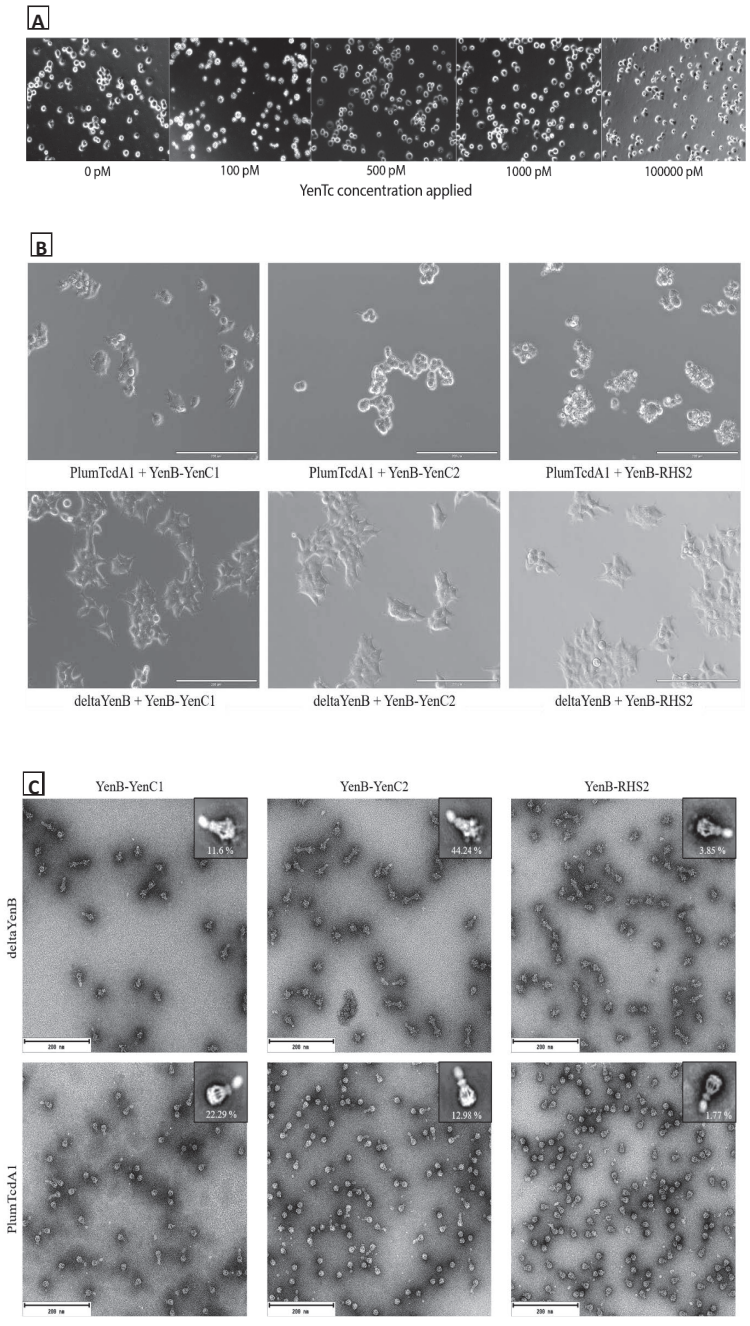

Figure S 3: YenTc lacks receptors on human cells but its HVRs are toxic

(A) YenTc is not toxic against Spodoptera frugiperda derived Sf9 cells even at high concentrations.

(B) Toxicity comparison of YenTc(ΔYenB) -YenBC and PlTcdA1-YenBC holotoxin complexes at 10 nM concentration against human-derived HEK293T cells.

(C) Negative stain micrographs of P. luminescens PlTcdA1 and Y. entomophaga YenTc(ΔYenB) A-subunits mixed with the three possible BC-cocoons of YenTc. Insects: representative class averages for the respective resulting holotoxins, with percentages of holotoxin particles compared to the total number of pentamer particles indicated. Note that unlike the PlTcdB2-TccC3 cocoon that demonstrates sub nanomolar binding affinity to PlTcdA1, the YenTc cocoons show a much lower apparent affinity to pre-formed A-subunits.

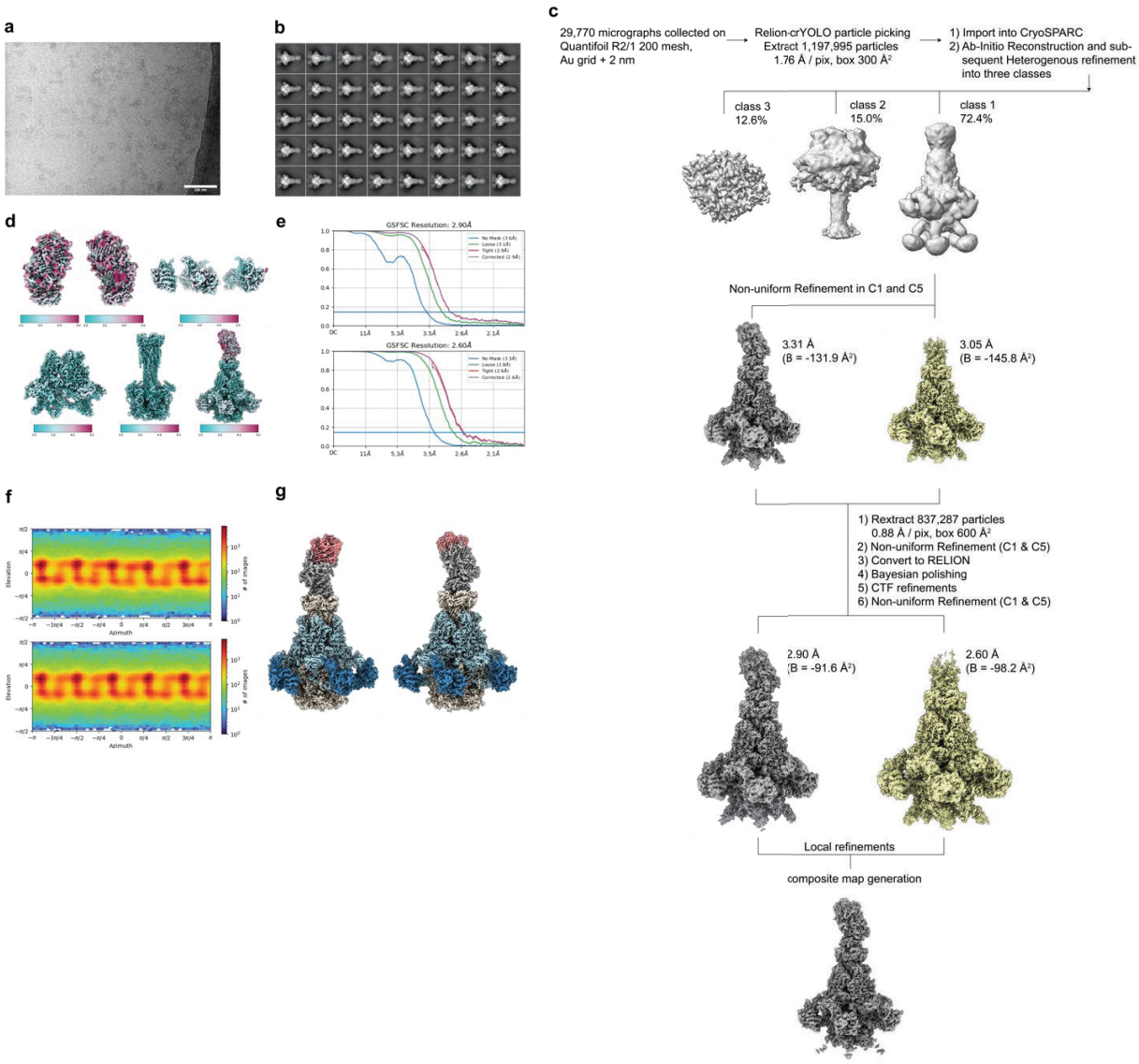

Figure S 4: Cryo-EM image processing of YenTc prepore state (a-g)

(a) Exemplary micrograph of YenTc prepore state at a defocus value of -1.6 µm. (b) Representative 2D classes for the data set. (c) Overview of processing strategy and exemplary intermediate volumes. (d) Local resolution estimates represented via color code on the corresponding volumes. (e) FSC curves showing the results of the final refinements without (top panel) and by applying C5 symmetry (lower panel). (f) PDD plots visualizing the alignment precision and angular distribution for both, C1 (top panel) and C5 (lower panel), symmetries. (g) Side-view representations of final composite map for YenTc prepore state.

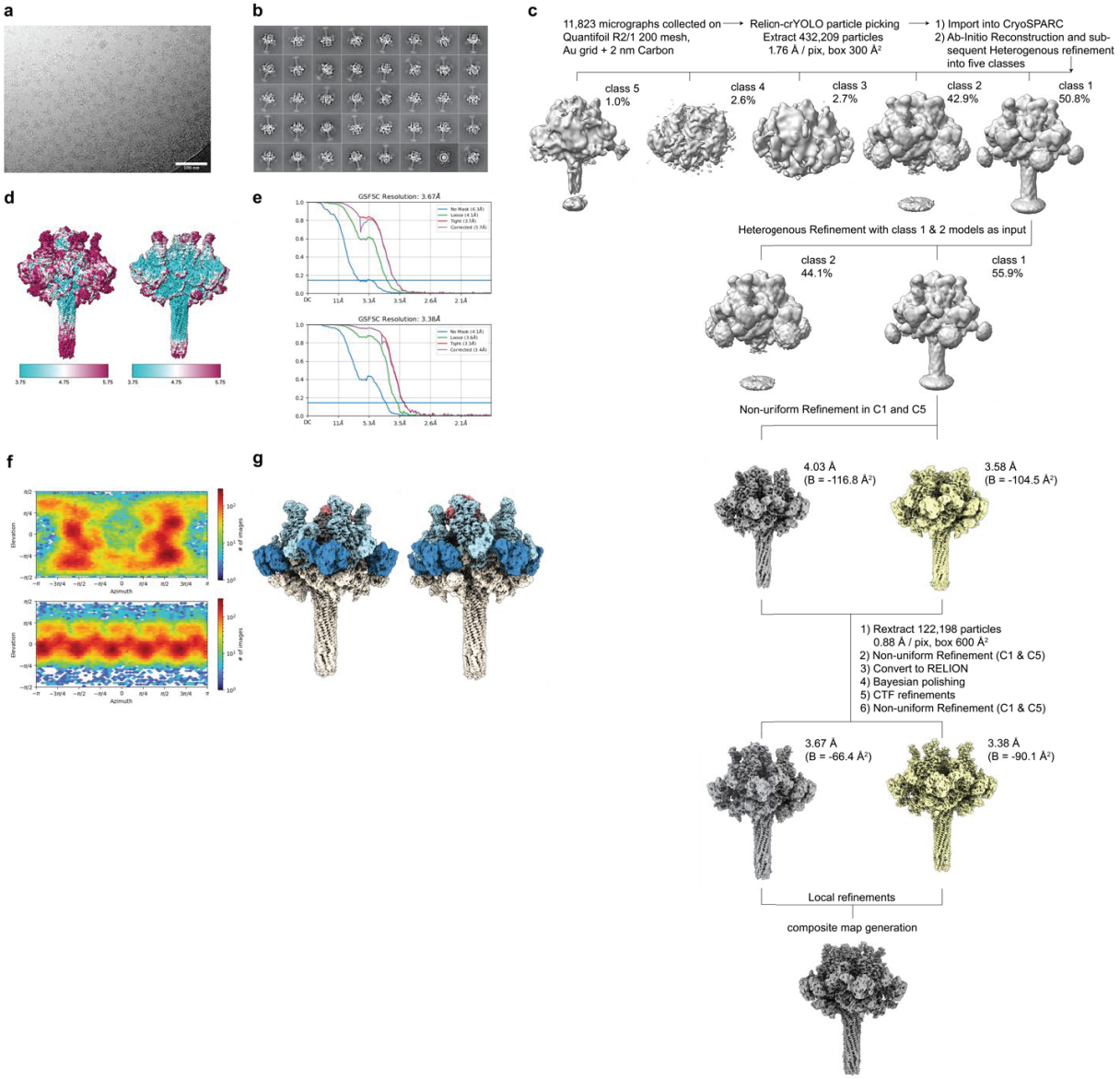

Figure S 5: Cryo-EM image processing of YenTc neutral pore state (a-g)

(**a**) Exemplary micrograph of YenTc neutral pore state at a defocus value of -1.6 µm. (**b**) Representative 2D classes for the data set. (**c**) Overview of processing strategy and exemplary intermediate volumes. (**d**) Local resolution estimates represented via color code on the corresponding volumes with (right panel) and without (left panel) C5 symmetry applied. (**e**) FSC curves showing the results of the final refinements without (top panel) and by applying C5 symmetry (lower panel). (**f**) PDD plots visualizing the alignment precision and angular distribution for both, C1 (top panel) and C5 (lower panel), symmetries. (**g**) Side-view representations of final composite map for YenTc neutral pore state.

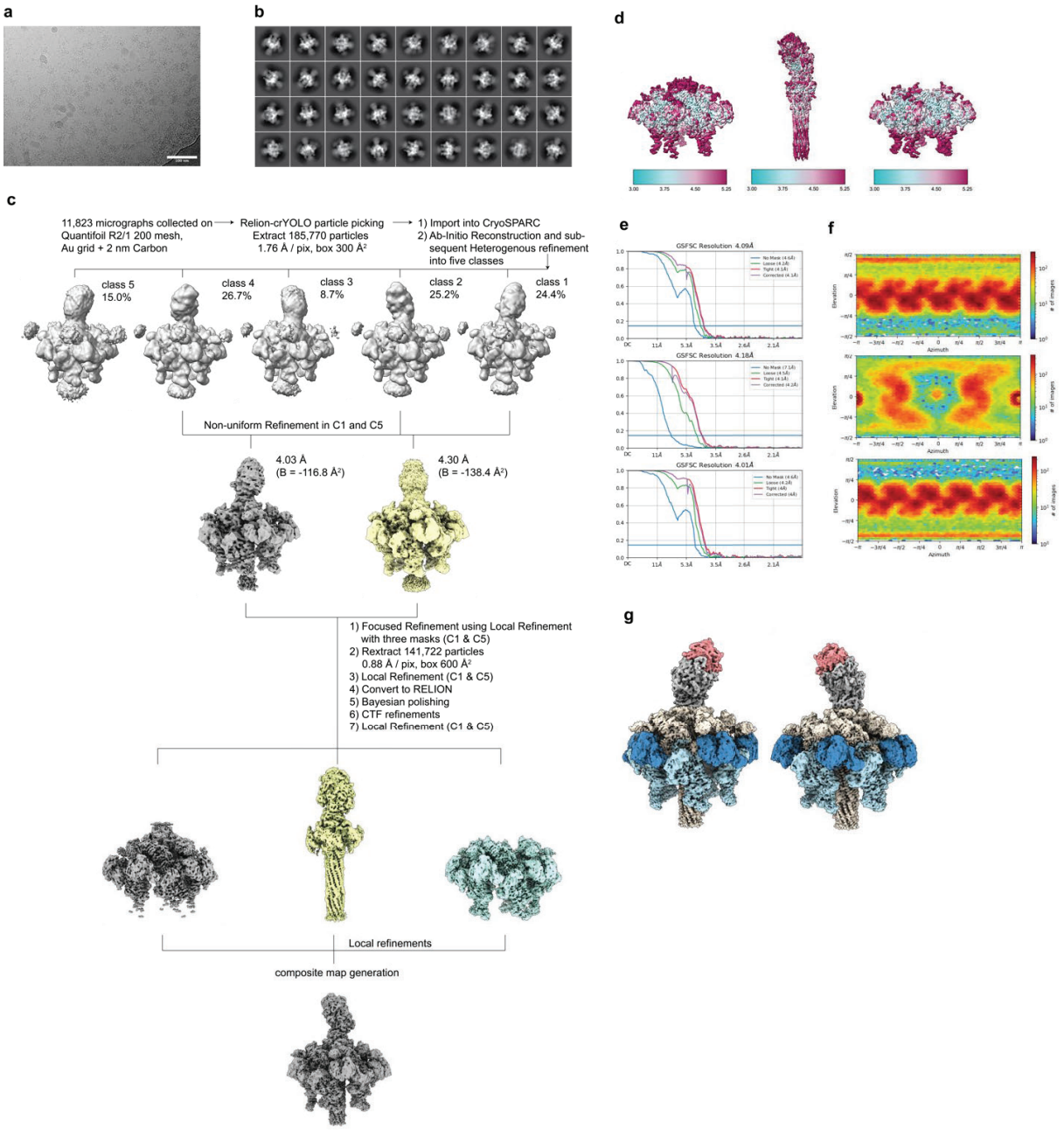

Figure S 6: Cryo-EM image processing of YenTc alternate pore state (a-g)

(**A**) Exemplary micrograph of YenTc alternate pore state at a defocus value of -1.6 µm. (**B**) Representative 2D classes for the data set. (**C**) Overview of processing strategy and exemplary intermediate volumes. (**D**) Local resolution estimates represented via color code on the corresponding volumes. (**E**) FSC curves showing the results of the final refinements for focused refinement on the central part (top panel), the channel and cocoon (middle panel) and the outer shell applying C5 symmetry (lower panel). (**F**) PDD plots visualizing the alignment precision and angular distribution focused refinements described in (e). (**G**) Side-view representations of final composite map for YenTc alternate pore state.

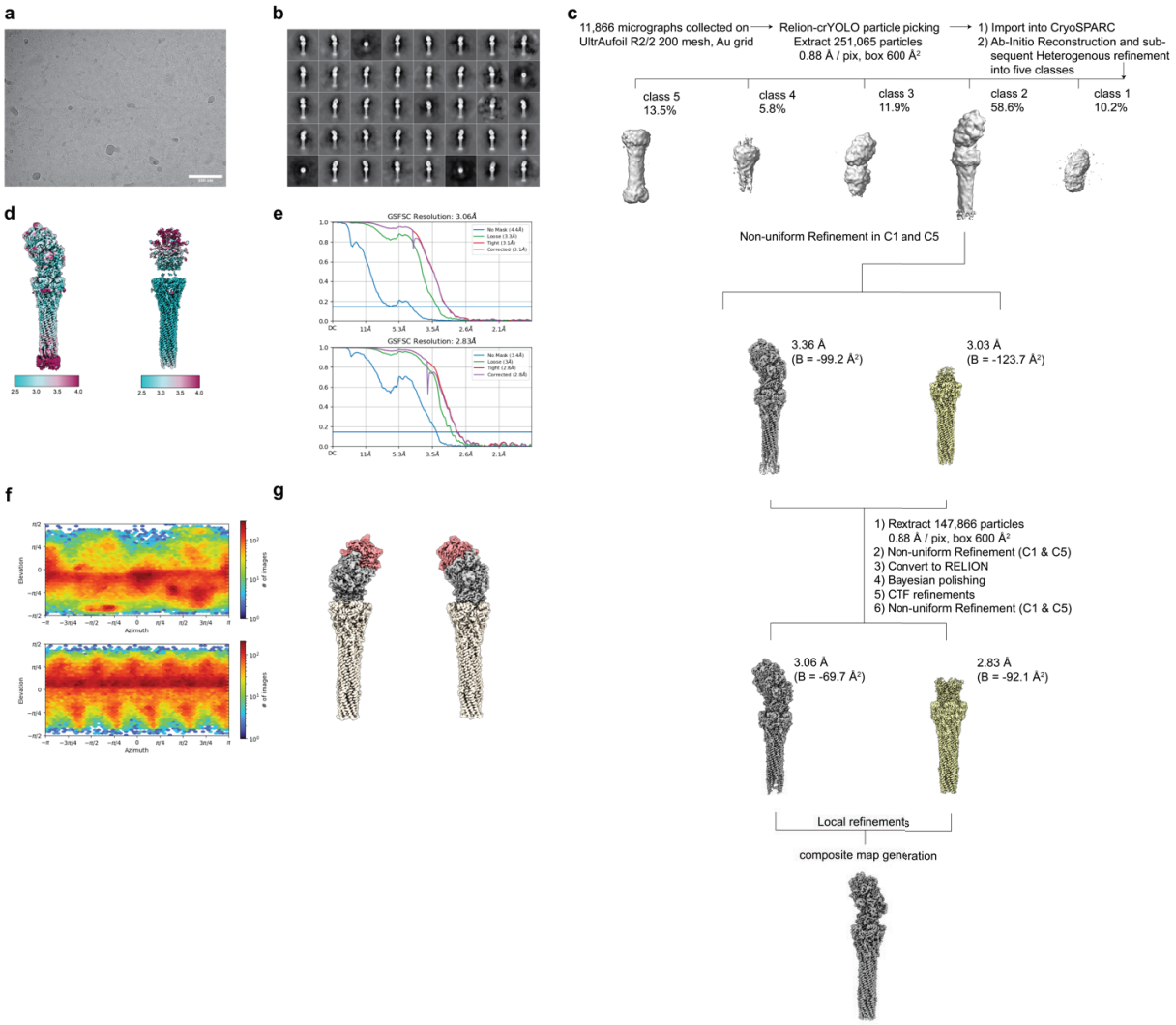

Figure S 7: Cryo-EM image processing of YenTc lollipop state (a-g)

(**A**) Exemplary micrograph of YenTc lollipop state at a defocus value of -1.6 µm. (**B**) Representative 2D classes for the data set. (**C**) Overview of processing strategy and exemplary intermediate volumes. (**D**) Local resolution estimates represented via color code on the corresponding volumes. (**E**) FSC curves showing the results of the final refinements without (top panel) and by applying C5 symmetry (lower panel). (**F**) PDD plots visualizing the alignment precision and angular distribution for both, C1 (top panel) and C5 (lower panel), symmetries. (**G**) Side-view representations of final composite map for YenTc lollipop state.

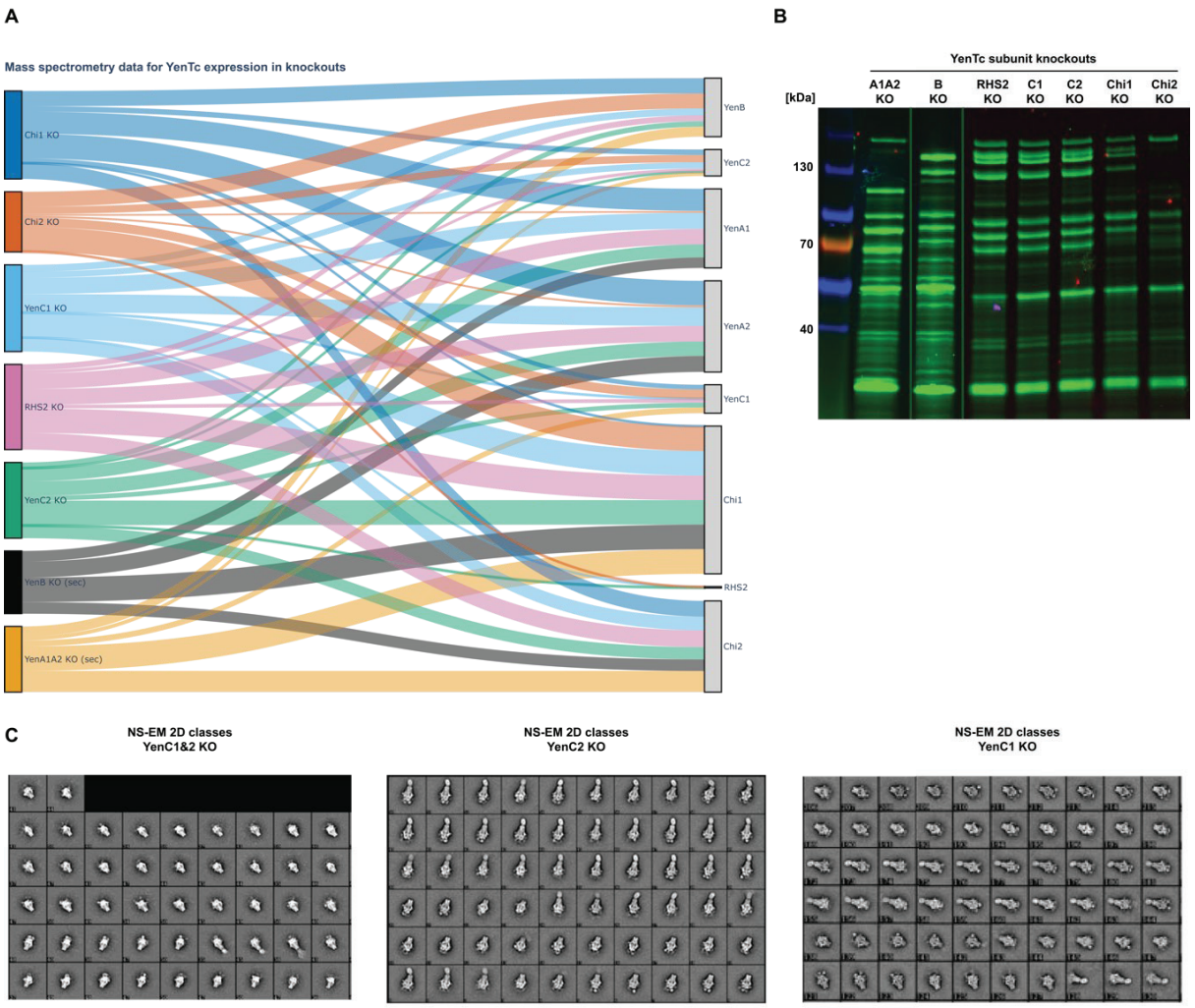

Figure S 8: Complex subunit arrangement uncovered using knockout mutants

(A) Mass spectrometry data from YenTc knockouts representing the abundance of expressed subunits visualized as Sankey Plot. (Thinner lines indicate a lower relative expression.) Note: Chi2 KO has a similar effect on the amounts of YenA1 and YenA2 detected as YenA1A2 KO.

(B) SDS_PAGE visualizing the absence of protein bands for specific KO versions. Notably once more is the effect of Chi2 KO on the YenA1A2 level.

(C) RHS2 being the least expressed toxic effector is visually supported by the amount of holotoxin classes detected in the YenC1andC2 KO (left panel), YenC2 KO (middle panel) as well as YenC1 KO (right panel). Almost no holotoxin class can be detected for the double knockout and almost equal amounts for the two single knockouts corresponding to the C effector not being deleted.

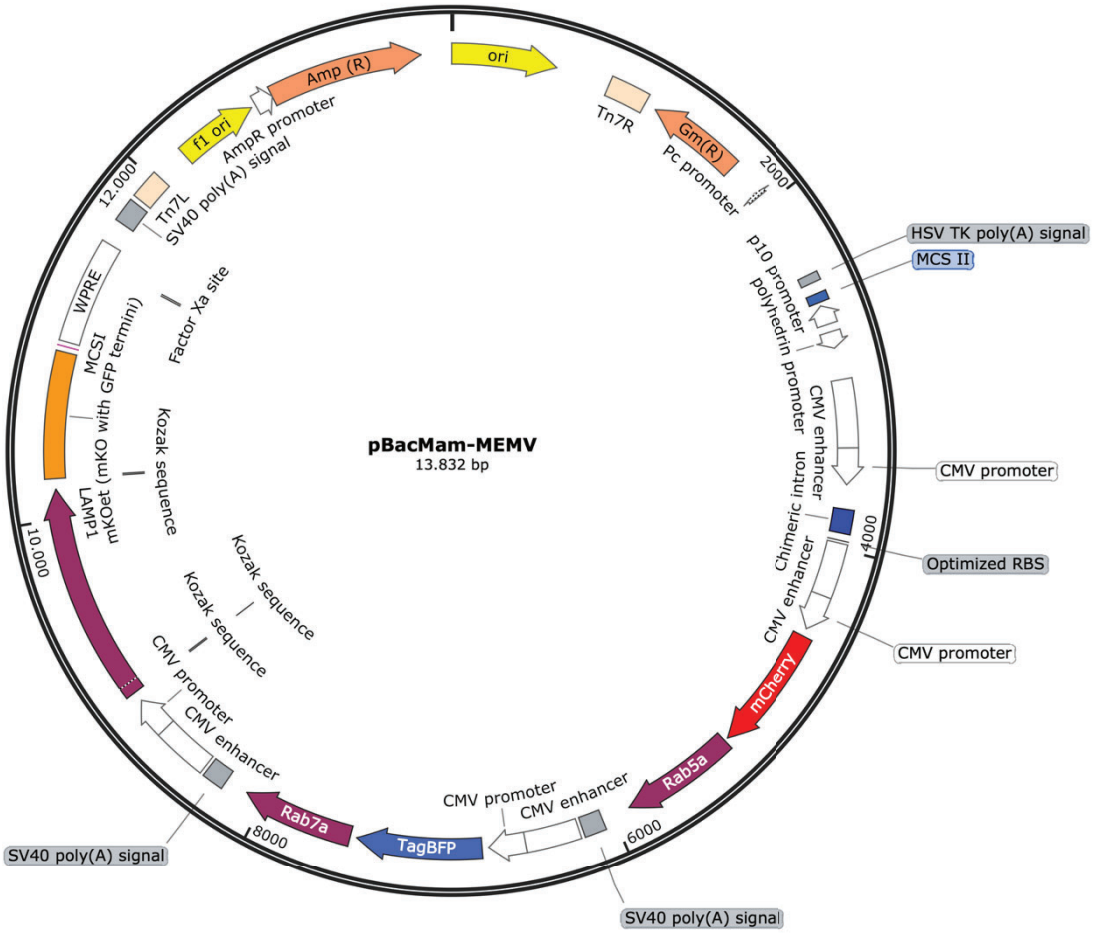

Figure S 9: Overview of the generated vector for fluorescent reporter system

Table 1: Cryo-EM statistics

YenTc Holotoxin	Prepore state	Pore state (neutral pH)	Pore state (neutral pH-inv)	Pore state (alkaline pH)
Data collection and processing				
Magnification	81,000	81,000	81,000	81,000
Voltage (kV)	300	300	300	300
Electron exposure ($e^{-}/Å^2$)	64.2	63	63	44.7
Defocus range (μm)	-0.8 to -1.6	-1.2 to -2.2	-1.2 to -2.2	-0.8 to -1.6
Pixel size (Å)	0.44	0.44	0.44	0.44
Symmetry imposed	C1	C1	C1	C1
Refinement				
Initial models used (PDB code)	6OGD 3OA5 4DWS 6H6E	6SUF	6SUF	6SUF
Model resolution (Å)	2.8	3.5	4.1	3.4
0.5 FSC threshold				
Map sharpening B factor ($Å^2$)				
Model composition				
Non-hydrogen atoms	133,323	129.058	128.933	69.736
Protein residues	16,807	16.272	16.262	4.452
Waters	0	0	0	0
Ligands	0	0	0	0
B factors ($Å^2$)				
Protein	76.73	99.54	158.77	130.11
Waters	0	0	0	0
Ligand	0	0	0	0
R.m.s. deviations				
Bond lengths (Å)	0.003	0.002	0.003	0.002
Bond angles (°)	0.675	0.501	0.562	0.514
Validation				
EM-ringer score	3.29			
MolProbity score	1.39	1.30	1.38	1.14
Clashscore	7.15	4.24	5.07	3.51
Poor rotamers (%)	0.81	0.11	0.16	0.55
Ramachandran plot				
Favored (%)	98.27	97.55	97.42	98.62
Allowed (%)	1.73	2.45	2.58	1.38
Disallowed (%)	0.00	0.00	0.00	0.00

Table 2: Analysis of AB interaction interfaces for YenTc (left) and PlTcdA1 (right)

STRUCTURE1	DISTANCE	STRUCTURE2
D:THR 503[OG1]	2.86963	B:LEU1229[O]
D:THR 503[N]	2.57764	B:MET1231[O]
D:THR 503[OG1]	3.11525	B:MET1231[O]
D:LEU 501[N]	3.37134	B:LEU1232[O]
D:ARG 481[NH1]	3.37143	B:GLY1234[O]
D:THR 503[OG1]	2.8925	B:MET1231[N]
D:LEU 501[O]	3.62754	B:VAL1233[N]
D:ASP 546[OD1]	3.66606	B:ASN1332[ND2]
STRUCTURE1	DISTANCE	STRUCTURE2
D:ARG 563[NH2]	3.04673	G:SER1179[OG]
D:ARG 563[NH2]	2.32801	G:ASP1333[OD2]
D:ASP 561[OD1]	3.52949	G:MET1231[N]
STRUCTURE1	DISTANCE	STRUCTURE2
D:ASN 667[N]	2.51324	J:MET1231[O]
D:ASN 667[OD1]	3.5973	J:MET1231[N]
STRUCTURE1	DISTANCE	STRUCTURE2
D:ILE 453[N]	3.4437	P:LEU1232[O]
D:ARG 455[N]	3.20698	P:MET1231[O]
D:ARG 455[NE]	3.20156	P:VAL1233[O]
D:ARG 455[NH2]	2.63522	P:GLY1234[O]
D:ARG 455[NH2]	2.53928	P:GLU1237[O]
D:PRO 423[O]	3.75784	P:TYR1236[N]
D:ILE 453[O]	3.32587	P:VAL1233[N]
D:ILE 453[O]	3.35934	P:GLY1234[N]
D:SER 477[O]	3.61531	P:ASN1291[ND2]
STRUCTURE1	DISTANCE	STRUCTURE2
D:ARG 563[NH2]	2.32801	G:ASP1333[OD2]

STRUCTURE1	DISTANCE	STRUCTURE2
A:LEU2423[N]	2.80968	F:LEU 492[O]
A:ASN2505[ND2]	2.70767	F:GLY 535[O]
A:ASP2358[OD2]	3.11298	F:LYS 534[NZ]
A:ALA2421[O]	2.85691	F:VAL 494[N]
A:LEU2423[O]	2.83721	F:LEU 492[N]
A:PRO2425[O]	3.04539	F:ARG 472[NH1]
A:GLN2427[O]	3.26131	F:ARG 472[NH2]
A:LYS2502[O]	2.75401	F:LYS 534[NZ]
STRUCTURE1	DISTANCE	STRUCTURE2
B:TYR2426[OH]	2.7304	F:ASP 413[OD2]
B:LEU2423[N]	2.98159	F:ILE 444[O]
B:ASN2505[ND2]	2.83342	F:PHE 486[O]
B:LEU2423[O]	2.83538	F:ILE 444[N]
B:TYR2426[OH]	2.91685	F:TRP 418[NE1]
B:MET2454[SD]	3.37423	F:GLN 448[N]
B:MET2454[SD]	3.36634	F:SER 449[N]
B:MET2454[SD]	3.32361	F:SER 449[OG]
B:LYS2502[O]	2.97196	F:ARG 485[NH1]
STRUCTURE1	DISTANCE	STRUCTURE2
C:ALA2421[N]	2.97213	F:TYR 411[OH]
C:ASN2505[ND2]	3.5456	F:MET 438[SD]
C:LEU2423[O]	2.97044	F:GLN 394[NE2]
STRUCTURE1	DISTANCE	STRUCTURE2
D:GLN2355[NE2]	3.39721	F:GLU 652[OE2]
D:ASN2505[ND2]	2.7527	F:ASP 657[OD2]
D:ALA2421[O]	2.93284	F:HIS 658[N]
D:ALA2421[O]	3.1648	F:HIS 658[ND1]
D:LEU2423[O]	2.80911	F:ASN 606[ND2]
D:LYS2502[O]	2.89699	F:ARG 655[NH2]
D:LEU2504[O]	3.67507	F:ARG 655[NH2]
D:ASN2505[OD1]	2.5268	F:ARG 655[NE]
STRUCTURE1	DISTANCE	STRUCTURE2
E:ALA2421[N]	3.22816	F:ALA 551[O]
E:TYR2426[OH]	2.69786	F:GLU 495[OE1]
E:ASN2505[ND2]	3.06744	F:ASP 552[OD2]
E:LEU2423[O]	2.92605	F:ARG 500[NH1]
E:GLY2424[O]	3.20523	F:ARG 500[NH2]
E:ASN2505[O]	2.89038	F:ARG 554[NH2]
E:ASP2506[OD2]	3.79676	F:ARG 554[NH1]
STRUCTURE1	DISTANCE	STRUCTURE2
A:ASP2358[OD1]	3.78633	F:LYS 534[NZ]
A:ASP2358[OD2]	3.11298	F:LYS 534[NZ]
STRUCTURE1	DISTANCE	STRUCTURE2
E:ASP2506[OD2]	3.79676	F:ARG 554[NH1]

Table 3: Mass spectrometry results for YenTc pore formation

Sequence	Proteins	Start	End posi-	Intensity	Intensity peak2
LSLVTQSVQQYINR	Toxin_variant_1;A0A3S6EXX9;Toxin_vari-	1774	1787	2.2E+10	1.5E+08
LALVAFK	Toxin_variant_1;A0A3S6EXX9;Toxin_vari-	2026	2032	2.1E+10	1.6E+09
VFISLDTPR	Toxin_variant_1;A0A3S6EWX1;Toxin_vari-	462	470	1.8E+10	3.0E+06
LSYSTASSLLGR	Toxin_variant_1;A0A3S6EXX9;Toxin_vari-	2433	2444	1.7E+10	9.7E+08
VIELQSQAANSLLMAQGMR	Toxin_variant_1;A0A3S6EXX9;Toxin_vari-	2667	2685	1.7E+10	5.2E+07
ALLGESWPAELNK	Toxin_variant_1;A0A3S6EXX9;Toxin_vari-	2892	2904	1.7E+10	1.0E+08
QLILYPVIINR	Toxin_variant_1;A0A3S6EXX9;Toxin_vari-	2100	2110	1.5E+10	1.5E+09
LNTLFAK	Toxin_variant_1;A0A3S6EXX9;Toxin_vari-	2266	2272	1.5E+10	1.1E+09
NATITTSIPSEEALK	Toxin_variant_1;A0A3S6EWX1;Toxin_vari-	389	403	1.4E+10	6.9E+08
GYSLTQPSDPDAIAASDPIHYR	Toxin_variant_1;A0A3S6EXX9;Toxin_vari-	2380	2401	1.3E+10	1.2E+08
YSIDDAVTHLIDEK	Toxin_variant_1;A0A3S6EWX1;Toxin_vari-	356	369	1.3E+10	
GLLGGFR	Toxin_variant_1;A0A3S6EWX1;Toxin_vari-	195	201	1.2E+10	
FSIDLQQQDIDINK	Toxin_variant_1;A0A3S6EXX9;Toxin_vari-	2619	2632	1.1E+10	2.4E+06
YGYWAANQQLR	Toxin_variant_1;A0A3S6EXX9;Toxin_vari-	1813	1823	1.1E+10	4.1E+08
GISIASSADPAK	Toxin_variant_1;A0A3S6EWX1;Toxin_vari-	296	307	1.0E+10	6.7E+08
ELYDENISSTEQK	Toxin_variant_1;A0A3S6EXX9;Toxin_vari-	2654	2666	1.0E+10	6.7E+07
AIFIGYAGYTR	Toxin_variant_1;A0A3S6EWX1;Toxin_vari-	375	385	9.9E+09	2.2E+08
EINMDLYDSSISPR	Toxin_variant_1;A0A3S6EXX9;Toxin_vari-	2531	2544	9.6E+09	6.4E+06
LGVATDPDDAIANHK	Toxin_variant_1;A0A3S6EWX1;Toxin_vari-	142	156	9.5E+09	8.3E+07
LIYSFGGLIGDKK	Toxin_variant_1;A0A3S6EWX1;Toxin_vari-	117	129	9.3E+09	4.2E+08
SESLSVSESYR	Toxin_variant_1;A0A3S6EXX9;Toxin_vari-	2729	2739	8.8E+09	6.0E+07
TNFVEGIKDFFQR	Toxin_variant_1;A0A3S6EWX1;Toxin_vari-	236	248	8.6E+09	
YSADGNASIAVR	Toxin_variant_1;A0A3S6EWX1;Toxin_vari-	130	141	8.0E+09	2.3E+08
TIPVDPDGAVLASINCGFTK	Toxin_variant_1;A0A3S6EWX1;Toxin_vari-	159	178	7.8E+09	
NANSQELYPTAWSEWK	Toxin_variant_1;A0A3S6EXX9;Toxin_vari-	1917	1932	7.8E+09	1.1E+08
NIIYGIWK	Toxin_variant_1;A0A3S6EXX9;Toxin_vari-	2160	2167	7.7E+09	
DWPIELDK	Toxin_variant_1;A0A3S6EXX9;Toxin_vari-	2111	2118	7.4E+09	
PLVDEPFK	Toxin_variant_1;A0A3S6EXX9;Toxin_vari-	2372	2379	7.3E+09	2.2E+08
LTDDVAQK	Toxin_variant_1;A0A3S6EXX9;Toxin_vari-	1854	1861	6.7E+09	6.2E+08
LNTPDGRPFK	Toxin_variant_1;A0A3S6EWX1;Toxin_vari-	106	115	6.3E+09	3.6E+08
QAEWEVNSVEQQINLQNMQIK	Toxin_variant_1;A0A3S6EXX9;Toxin_vari-	2751	2771	6.1E+09	
AAGLLGGLR	Toxin_variant_1;Toxin_variant_2;Toxin_vari-	3360	3368	5.8E+09	7.0E+09
LVAFGDQTGSK	Toxin_variant_1;A0A3S6EWV3;Toxin_vari-	1048	1058	5.7E+09	8.6E+07
RRQEWELQYK	Toxin_variant_1;A0A3S6EXX9;Toxin_vari-	2741	2750	5.2E+09	
MFPEIYVDPTLR	Toxin_variant_1;A0A3S6EXX9;Toxin_vari-	1824	1835	5.2E+09	1.6E+08
NIIDQGDMEYR	Toxin_variant_1;A0A3S6EXX9;Toxin_vari-	2411	2421	5.1E+09	1.6E+08
LSLDNDALYK	Toxin_variant_1;A0A3S6EWV3;Toxin_vari-	740	749	5.1E+09	4.5E+09
SPYPDDLPETLFDSSYDTQQQQLHLTK	Toxin_variant_1;Toxin_variant_2;Toxin_vari-	4689	4715	4.9E+09	
LEALNDRDVTDEIPVLVNR	Toxin_variant_1;Toxin_variant_2;Toxin_vari-	4037	4055	4.8E+09	3.6E+06
DTDGFAQGTVDIPTHPSR	Toxin_variant_1;Toxin_variant_2;Toxin_vari-	4512	4529	4.8E+09	2.3E+07
EIQSLSNFR	Toxin_variant_1;A0A3S6EWV3;Toxin_vari-	1124	1132	4.8E+09	
ILFSDGFGR	Toxin_variant_1;Toxin_variant_2;Toxin_vari-	5070	5078	4.7E+09	
LIQDFIK	Toxin_variant_1;Toxin_variant_2;Toxin_vari-	3855	3861	4.6E+09	4.8E+07
SVVPLQLR	Toxin_variant_1;A0A3S6EWV3;Toxin_vari-	1490	1497	4.5E+09	
SEIFDEITGNR	Toxin_variant_1;Toxin_variant_2;Toxin_vari-	4473	4483	4.5E+09	3.3E+07
WEAGDANER	Toxin_variant_1;A0A3S6EWX1;Toxin_vari-	179	187	4.4E+09	
LAVVPTNNMVTFFK	Toxin_variant_1;A0A3S6EWV3;Toxin_vari-	1372	1385	4.3E+09	1.5E+07
LRGENIITYQR	Toxin_variant_1;A0A3S6EWV3;Toxin_vari-	930	940	4.1E+09	6.0E+09
VFNVIFDGK	Toxin_variant_1;Toxin_variant_2;Toxin_vari-	3117	3125	4.0E+09	
FIQSVELDGSNQAR	Toxin_variant_1;A0A3S6EWV3;Toxin_vari-	715	728	4.0E+09	3.0E+09
LTQPNWLGLTQPK	Toxin_variant_1;A0A3S6EWV3;Toxin_vari-	1553	1565	4.0E+09	
GDDQAFSPFSPR	Toxin_variant_1;Toxin_variant_2;Toxin_vari-	4552	4563	3.9E+09	3.5E+07
FGQPLTLEGFSQPQTSFNPDR	Toxin_variant_1;Toxin_variant_2;Toxin_vari-	4313	4333	3.9E+09	
NIIDQGDMEYRK	Toxin_variant_1;A0A3S6EXX9;Toxin_vari-	2411	2422	3.9E+09	4.1E+07
RQEWELQYK	Toxin_variant_1;A0A3S6EXX9;Toxin_vari-	2742	2750	3.8E+09	1.2E+07
VAADPQCSQQVVIK	Toxin_variant_1;Toxin_variant_2;Toxin_vari-	4652	4665	3.7E+09	2.8E+07
HNLTLDGK	Toxin_variant_1;A0A3S6EXX9;Toxin_vari-	2523	2530	3.7E+09	3.9E+07
VESEPDVWVAR	Toxin_variant_1;Toxin_variant_2;Toxin_vari-	4839	4849	3.6E+09	1.9E+07
LIYSFGGLIGDK	Toxin_variant_1;A0A3S6EWX1;Toxin_vari-	117	128	3.5E+09	9.4E+07
NVDDLYDHLLLDTQVSAK	Toxin_variant_1;A0A3S6EXX9;Toxin_vari-	1751	1768	3.4E+09	
SAVGGDLTTR	Toxin_variant_1;Toxin_variant_2;Toxin_vari-	3567	3576	3.4E+09	5.7E+09
KDSLSFDAYQMIQSGDLYR	Toxin_variant_1;A0A3S6EXX9;Toxin_vari-	2600	2618	3.3E+09	
IEYWQPVK	Toxin_variant_1;Toxin_variant_2;Toxin_vari-	3862	3869	3.3E+09	
GHIVPLDPYGDLGTAR	Toxin_variant_1;Toxin_variant_2;Toxin_vari-	3318	3333	3.2E+09	3.4E+09
RLEQVEAQQQQAMALLDYFSER	Toxin_variant_1;A0A3S6EXX9;Toxin_vari-	2776	2797	3.2E+09	
QEWELQYK	Toxin_variant_1;A0A3S6EXX9;Toxin_vari-	2743	2750	3.1E+09	
ENVSSETMVSRPFLTMTYR	Toxin_variant_1;A0A3S6EWV3;Toxin_vari-	992	1010	3.1E+09	5.8E+07
VDPQFSWNTTQEK	Toxin_variant_1;A0A3S6EWV3;Toxin_vari-	819	831	3.1E+09	3.0E+08
LQGIPLPFSYK	Toxin_variant_1;Toxin_variant_2;Toxin_vari-	3837	3847	3.1E+09	3.9E+07
NAQENLLSQTISAEYGVER	Toxin_variant_1;A0A3S6EWV3;Toxin_vari-	1471	1489	3.1E+09	3.4E+07
VIDMTPFYLDSDEELPTYTE-	Toxin_variant_1;A0A3S6EWX1;Toxin_vari-	515	546	3.0E+09	
GHFISLDTPR	Toxin_variant_1;Toxin_variant_2;Toxin_vari-	3635	3644	3.0E+09	2.7E+09
EGVGEAVMAALK	Toxin_variant_1;A0A3S6EWV3;Toxin_vari-	1691	1702	2.9E+09	2.2E+09
KAVFNFLTK	Toxin_variant_1;A0A3S6EXX9;Toxin_vari-	2402	2410	2.8E+09	4.8E+07
TDAAGAVLTTIDAVGNQQR	Toxin_variant_2;A0A3S6EWV9	5437	5455	2.8E+09	
TDLFADTHIYDPLGR	Toxin_variant_1;Toxin_variant_2;Toxin_vari-	5153	5167	2.8E+09	3.9E+06
DATGLYYYGFR	Toxin_variant_1;Toxin_vari-	5832	5842	2.7E+09	
GFDLATLMQNPATYDR	Toxin_variant_1;Toxin_variant_2;Toxin_vari-	3262	3277	2.7E+09	2.2E+06
LLTPEDYEPQINATLVMCDK	Toxin_variant_1;A0A3S6EXX9;Toxin_vari-	2181	2200	2.7E+09	
EEVLADQMEEMIAVVDR	Toxin_variant_1;A0A3S6EXX9;Toxin_vari-	2003	2019	2.6E+09	
QTDGTPFWIIYSPDGQTHILGK	Toxin_variant_1;Toxin_variant_2;Toxin_vari-	3870	3891	2.6E+09	
ALPTTDATVPSAWCSTIETR	Toxin_variant_1;Toxin_variant_2;Toxin_vari-	4626	4645	2.6E+09	
FVTEDGYVCALGR	Toxin_variant_1;Toxin_variant_2;Toxin_vari-	5011	5023	2.5E+09	8.7E+06
GAETCLFYR	Toxin_variant_1;Toxin_variant_2;Toxin_vari-	4431	4439	2.5E+09	
VYQPYFLDDWR	Toxin_variant_1;Toxin_variant_2;Toxin_vari-	5134	5144	2.5E+09	
SNLIYDKDPGYVWDNK	Toxin_variant_1;A0A3S6EWX1;Toxin_vari-	11	26	2.5E+09	4.9E+07
IGNPTTADVKPTENIPSPILVEDK	Toxin_variant_1;Toxin_variant_2;Toxin_vari-	3166	3189	2.4E+09	6.0E+08
QVAYETDGSPITQPPLEFDYQR	Toxin_variant_1;Toxin_variant_2;Toxin_vari-	4074	4095	2.3E+09	
EYQVITAK	Toxin_variant_1;Toxin_variant_2;Toxin_vari-	5168	5175	2.3E+09	2.9E+07
VLHWESGKPDGIINDQIR	Toxin_variant_2;A0A3S6EWV9	5769	5786	2.3E+09	4.8E+06
EGLGYVADSNQETIDMGPLYNPGK	Toxin_variant_1;Toxin_variant_2;Toxin_vari-	3679	3702	2.3E+09	6.9E+07
YYQPWAGR	Toxin_variant_1;Toxin_variant_2;Toxin_vari-	5843	5850	2.2E+09	
VYTNTYWVER	Toxin_variant_1;Toxin_variant_2;Toxin_vari-	3126	3135	2.2E+09	1.6E+09
LAHLGFDGVWSSGTTLR	Toxin_variant_1;A0A3S6EXX9;Toxin_vari-	1986	2002	2.1E+09	

AVSMANQVLQK	Toxin_variant_1;A0A3S6EWV3;Toxin_vari-	637	647	2.1E+09	9.6E+06
LAYDVAGFLK	Toxin_variant_1;A0A3S6EXC9	5449	5458	2.1E+09	
EYIDQSGQADK	Toxin_variant_1;A0A3S6EWV3;Toxin_vari-	767	777	2.1E+09	1.4E+06
VLYLAGLER	Toxin_variant_1;A0A3S6EXC9	5723	5731	2.0E+09	1.7E+07
QNLDSLNDVILHVK	Toxin_variant_1;A0A3S6EXX9;Toxin_vari-	3036	3049	2.0E+09	1.2E+07
YDFGIEIR	Toxin_variant_1;Toxin_variant_2;Toxin_vari-	4016	4023	2.0E+09	
TRDELLFSAGYQLAPR	Toxin_variant_1;Toxin_variant_2;Toxin_vari-	4820	4835	2.0E+09	
LDWVITSAGVR	Toxin_variant_1;Toxin_variant_2;Toxin_vari-	4186	4196	2.0E+09	6.4E+06
SQYSQSLADTLLGLGYR	Toxin_variant_1;A0A3S6EWV3;Toxin_vari-	589	605	2.0E+09	
SSAQFWLDEK	Toxin_variant_1;Toxin_variant_2;Toxin_vari-	4440	4449	1.9E+09	9.5E+06
YTYDPVGNVLR	Toxin_variant_1;A0A3S6EXC9	5529	5539	1.9E+09	2.2E+07
LTQEQEYAHGSWDGQER	Toxin_variant_1;Toxin_variant_2;Toxin_vari-	4484	4500	1.9E+09	9.2E+06
TPPHSLTITTDRYDSDDQQQLR	Toxin_variant_1;Toxin_variant_2;Toxin_vari-	5046	5067	1.9E+09	7.3E+06
NAMTIIR	Toxin_variant_1;A0A3S6EWV3;Toxin_vari-	1112	1118	1.9E+09	2.6E+09
AVNQILGDTHFPFTLPYSLPTQQINK	Toxin_variant_1;A0A3S6EWV3;Toxin_vari-	778	803	1.9E+09	
MEALSAWLTK	Toxin_variant_1;A0A3S6EWV3;Toxin_vari-	1346	1355	1.9E+09	
LSHHTNIYRDPSDVYSK	Toxin_variant_1;A0A3S6EWX1;Toxin_vari-	339	355	1.9E+09	9.5E+07
TLQAFVGVLDSK	Toxin_variant_1;Toxin_variant_2;Toxin_vari-	4808	4819	1.8E+09	
ETDSDGNIIVSGR	Toxin_variant_1;A0A3S6EXX9;Toxin_vari-	1967	1979	1.8E+09	
ITEHFVYAGNTPQEK	Toxin_variant_2;A0A3S6EWV9	5351	5365	1.8E+09	
LEQVEAQQQQAMALLDYFSER	Toxin_variant_1;A0A3S6EXX9;Toxin_vari-	2777	2797	1.8E+09	
QIGGDSNAVTYGAMK	Toxin_variant_1;Toxin_variant_2;Toxin_vari-	4149	4163	1.8E+09	
IHLGYANYGR	Toxin_variant_1;Toxin_variant_2;Toxin_vari-	3557	3566	1.7E+09	1.6E+09
FLPFEGSGVDSSWR	Toxin_variant_1;A0A3S6EXX9;Toxin_vari-	3015	3028	1.7E+09	
LSAYITDWCQYDAR	Toxin_variant_1;Toxin_variant_2;Toxin_vari-	3235	3248	1.6E+09	1.1E+07
QSAQDRYDHFKELYDENISSTEQK	Toxin_variant_1;A0A3S6EXX9;Toxin_vari-	2643	2666	1.6E+09	
YDHFKELYDENISSTEQK	Toxin_variant_1;A0A3S6EXX9;Toxin_vari-	2649	2666	1.6E+09	
EISIACSGVK	Toxin_variant_1;Toxin_variant_2;Toxin_vari-	3473	3482	1.6E+09	1.6E+09
DPSDVYSK	Toxin_variant_1;A0A3S6EWX1;Toxin_vari-	348	355	1.6E+09	1.2E+08
TVLLVAR	Toxin_variant_2;A0A3S6EWV9	5691	5697	1.5E+09	1.6E+07
KVQEVWDGWNAQAPSLGLPQIGK	Toxin_variant_1;Toxin_variant_2;Toxin_vari-	3295	3317	1.5E+09	
WQVPGIGSSDGNPHNAWK	Toxin_variant_1;Toxin_variant_2;Toxin_vari-	3136	3153	1.5E+09	7.1E+08
NECEGAAEETYQELNYEPSISADK	Toxin_variant_1;A0A3S6EWX1;Toxin_vari-	27	50	1.5E+09	
AIEMQSQPLTFEPVVHDQTMSAVDN-	Toxin_variant_1;A0A3S6EXX9;Toxin_vari-	2472	2508	1.5E+09	
VEAGESWQR	Toxin_variant_1;Toxin_variant_2;Toxin_vari-	5086	5094	1.5E+09	
TFADTPHLVR	Toxin_variant_1;A0A3S6EXX9;Toxin_vari-	2977	2986	1.5E+09	4.4E+06
LNTPDGRPFKR	Toxin_variant_1;A0A3S6EWX1;Toxin_vari-	106	116	1.5E+09	3.3E+08
AMSDISDVIGEPLAAWDSQVGGR	Toxin_variant_1;Toxin_variant_2;Toxin_vari-	3094	3116	1.4E+09	
FYWAGSDASQK	Toxin_variant_1;A0A3S6EXC9	5352	5362	1.4E+09	1.0E+07
QGYSEFGDYSQFWRPLSQR	Toxin_variant_1;Toxin_variant_2;Toxin_vari-	4850	4868	1.4E+09	
LQEEHGNGVLTTYSYEAETQR	Toxin_variant_1;A0A3S6EXC9	5485	5505	1.4E+09	4.1E+06
LLQSAQR	Toxin_variant_1;Toxin_variant_2;Toxin_vari-	5079	5085	1.4E+09	2.8E+07
AQVQAMHWELGQPTEVANDELR	Toxin_variant_1;A0A3S6EXC9	5755	5776	1.4E+09	
QNQLLPGQTLSWNAR	Toxin_variant_1;A0A3S6EXC9	5662	5676	1.4E+09	4.4E+06
GGQEQIIVK	Toxin_variant_1;A0A3S6EXC9	5466	5474	1.4E+09	1.8E+07
GGQEQVIIK	Toxin_variant_2;A0A3S6EWV9	5473	5481	1.4E+09	
VTEECITYHQFDFR	Toxin_variant_2;A0A3S6EWV9	5238	5251	1.4E+09	
SELYGDDGTPEAEIPYSVTEMR	Toxin_variant_1;Toxin_variant_2;Toxin_vari-	4600	4621	1.3E+09	
SDEEMLMEK	Toxin_variant_1;A0A3S6EWV3;Toxin_vari-	1438	1446	1.3E+09	1.7E+09
YLSDDSAR	Toxin_variant_1;Toxin_variant_2;Toxin_vari-	5145	5152	1.3E+09	
WLSADPAGTVDGLNLYR	Toxin_variant_2;A0A3S6EWV9	5861	5877	1.3E+09	
EVAGAGQQGSDLP-	Toxin_variant_2;A0A3S6EWV9	5583	5613	1.3E+09	
YEYDPVGNVLSITNDAEETR	Toxin_variant_2;A0A3S6EWV9	5536	5555	1.2E+09	
PAISISATGVSHTWQYEGENRPGR	Toxin_variant_1;A0A3S6EXC9	5310	5333	1.2E+09	
LCHQVLGFHR	Toxin_variant_1;Toxin_variant_2;Toxin_vari-	4027	4036	1.2E+09	
ANNLAGQCLR	Toxin_variant_1;A0A3S6EXC9	5363	5372	1.2E+09	1.4E+07
VLTYSAAGQK	Toxin_variant_2;A0A3S6EWV9	5482	5491	1.2E+09	
TPSVTVFDNR	Toxin_variant_2;A0A3S6EWV9	5211	5220	1.2E+09	1.3E+07
SLTYSAAGQK	Toxin_variant_1;Toxin_vari-	5475	5484	1.2E+09	
MQNSQEMAITTLSLPK	Toxin_variant_1;Toxin_variant_2;Toxin_vari-	3716	3731	1.2E+09	
NNLTPASLALLLGVTR	Toxin_variant_1;A0A3S6EWV3;Toxin_vari-	1356	1371	1.1E+09	
LGGVFSWSGDQDCGLLANAAR	Toxin_variant_1;Toxin_variant_2;Toxin_vari-	3658	3678	1.1E+09	
EMANIPQQSSQLPTLSPID-	Toxin_variant_1;A0A3S6EXC9	5576	5603	1.1E+09	
GPTQLVEHSDASYDVIELTCTNQAK	Toxin_variant_1;A0A3S6EWV3;Toxin_vari-	899	923	1.1E+09	
MVPFDNSSPFSR	Toxin_variant_1;A0A3S6EWV3;Toxin_vari-	945	956	1.1E+09	1.2E+09
QTQDKDFLSIILK	Toxin_variant_1;A0A3S6EWV3;Toxin_vari-	1333	1345	1.1E+09	4.7E+08
NDGYQYDQER	Toxin_variant_1;Toxin_variant_2;Toxin_vari-	4739	4748	1.1E+09	1.3E+07
HLNLQYK	Toxin_variant_1;A0A3S6EWV3;Toxin_vari-	1185	1191	1.1E+09	1.1E+08
IAFHQYDSYGFISQSIDPR	Toxin_variant_1;A0A3S6EXC9	5246	5264	1.1E+09	
LQEDLRDALVDYYLGQIVPNSK	Toxin_variant_1;A0A3S6EXX9;Toxin_vari-	1719	1740	1.0E+09	
IPTFEGGTTGWLARPDMFSR	Toxin_variant_1;Toxin_variant_2;Toxin_vari-	3996	4015	1.0E+09	
NVGLPPESADTSIESGTFLPYYQQNR	Toxin_variant_1;Toxin_variant_2;Toxin_vari-	3334	3359	9.9E+08	
HDESLLGNGAVIFDK	Toxin_variant_1;A0A3S6EWV3;Toxin_vari-	622	636	9.5E+08	3.7E+08
SEDSSLVVNVSGTPALVVTDNR	Toxin_variant_1;Toxin_variant_2;Toxin_vari-	5095	5116	9.4E+08	
SESLSVSESYRR	Toxin_variant_1;A0A3S6EXX9;Toxin_vari-	2729	2740	9.1E+08	
HTSAAANNSYTTNITVSK	Toxin_variant_1;A0A3S6EXC9	5618	5635	9.1E+08	
ADANGETLVQTDAMGNIQR	Toxin_variant_1;A0A3S6EXC9	5430	5448	8.9E+08	
CDLALNKPWLLNVMNNNR	Toxin_variant_1;Toxin_variant_2;Toxin_vari-	4413	4430	8.7E+08	
GLGASNIELGTVIQR	Toxin_variant_1;A0A3S6EWV3;Toxin_vari-	804	818	8.6E+08	1.6E+09
TYTYDSAGNLMR	Toxin_variant_2;A0A3S6EWV9	5614	5625	8.6E+08	4.4E+06
DKGLGGLFIWSGDQDNGILT-	Toxin_variant_1;A0A3S6EWX1;Toxin_vari-	481	508	8.5E+08	
QQQNYFHLTNDDNWLLGLPK	Toxin_variant_1;Toxin_variant_2;Toxin_vari-	4716	4735	7.8E+08	
NEDSIHEYLEFANIK	Toxin_variant_1;A0A3S6EWV3;Toxin_vari-	1591	1605	7.8E+08	2.7E+07
TLVDNSEK	Toxin_variant_1;A0A3S6EWV3;Toxin_vari-	1612	1619	7.7E+08	
QFSQTQYLQFPEASSADVWYIGK	Toxin_variant_1;A0A3S6EXX9;Toxin_vari-	2240	2262	7.7E+08	
HNLTLDGKEINMDLYDSSISPR	Toxin_variant_1;A0A3S6EXX9;Toxin_vari-	2523	2544	7.6E+08	
QLVAFADMLGSGQQHLVEITADSVK	Toxin_variant_1;Toxin_variant_2;Toxin_vari-	4279	4303	7.4E+08	
RLQTLSEK	Toxin_variant_1;A0A3S6EWV3;Toxin_vari-	1660	1667	7.3E+08	1.6E+09
VCAPMYNHYVGDK	Toxin_variant_1;Toxin_variant_2;Toxin_vari-	3218	3230	7.2E+08	4.3E+08
VVPENAYR	Toxin_variant_2;A0A3S6EWV9	5562	5569	7.0E+08	
TIHQGNTLFETLLVVK	Toxin_variant_1;A0A3S6EXC9	5733	5748	7.0E+08	
LTQHDVSER	Toxin_variant_1;Toxin_variant_2;Toxin_vari-	4987	4995	6.9E+08	
DAGYSTPQAK	Toxin_variant_1;Toxin_variant_2;Toxin_vari-	4943	4952	6.8E+08	
YSIDDAVTHLIDEKK	Toxin_variant_1;A0A3S6EWX1;Toxin_vari-	356	370	6.7E+08	
NYMDAEHSLSMGK	Toxin_variant_1;Toxin_variant_2;Toxin_vari-	3601	3613	6.6E+08	3.2E+08
QPAFDDKQTQDKDFLSIILK	Toxin_variant_1;A0A3S6EWV3;Toxin_vari-	1326	1345	6.6E+08	
HPDTPQEIAER	Toxin_variant_1;A0A3S6EXC9	5235	5245	6.5E+08	7.4E+06
KQDSSVKPNLSYFTALSGEVLR	Toxin_variant_1;A0A3S6EXC9	5270	5291	6.5E+08	
IPTFEGGTTGWLAR	Toxin_variant_1;Toxin_variant_2;Toxin_vari-	3996	4009	6.5E+08	
RVLYLAGLER	Toxin_variant_1;A0A3S6EXC9	5722	5731	6.3E+08	
EEVLADQMEEMIAVVDRMEDEPR	Toxin_variant_1;A0A3S6EXX9;Toxin_vari-	2003	2025	6.3E+08	

GIANGLSENVCLTTDDFQR	Toxin_variant_1;A0A3S6EWV3;Toxin_vari-	1386	1404	6.1E+08	
CLQQGQSLIWTPR	Toxin_variant_2;A0A3S6EWV9	5674	5686	6.1E+08	
TMTGGVAEAENLQVICIGEAGR	Toxin_variant_2;A0A3S6EWV9	5743	5764	6.1E+08	
KYSADGNASIAVR	Toxin_variant_1;A0A3S6EWX1;Toxin_vari-	129	141	5.9E+08	
YGSPLLSVAINYPR	Toxin_variant_1;Toxin_variant_2;Toxin_vari-	4669	4682	5.6E+08	
EVLEVSSGENITSANK	Toxin_variant_1;A0A3S6EXC9	5948	5963	5.5E+08	6.5E+07
GLGGLFIWSGDQDNGILTNAAHEGLK	Toxin_variant_1;A0A3S6EWX1;Toxin_vari-	483	508	5.5E+08	
LQEGATLMDINGDGR	Toxin_variant_1;Toxin_variant_2;Toxin_vari-	4171	4185	5.5E+08	2.1E+06
WLSADPAGTIDGLNLFR	Toxin_variant_1;A0A3S6EXC9	5851	5867	5.4E+08	
YDSLYQLVSASGR	Toxin_variant_2;A0A3S6EWV9	5570	5582	5.4E+08	4.2E+06
HYCVVIETQDAAQLVTQAR	Toxin_variant_1;Toxin_variant_2;Toxin_vari-	4883	4901	5.4E+08	
DVTDEIPVLVNR	Toxin_variant_1;Toxin_variant_2;Toxin_vari-	4044	4055	5.2E+08	
TERPAGHLSGAR	Toxin_variant_1;A0A3S6EXC9	5511	5522	5.0E+08	
GPYFANMDIYAAEWVR	Toxin_variant_1;A0A3S6EWV3;Toxin_vari-	976	991	5.0E+08	
PLVDEPFKGYSLTQPSDPDAIAASDPI-	Toxin_variant_1;A0A3S6EXX9;Toxin_vari-	2372	2401	4.7E+08	
NYHYDSAGNLMQIR	Toxin_variant_1;A0A3S6EXC9	5604	5617	4.7E+08	
RHDESLLGNGAVIFDK	Toxin_variant_1;A0A3S6EWV3;Toxin_vari-	621	636	4.7E+08	2.7E+07
GVMSSLTENPADVDALFTASGSQK	Toxin_variant_2;A0A3S6EWV9	5650	5673	4.7E+08	
LSHHTNIYR	Toxin_variant_1;A0A3S6EWX1;Toxin_vari-	339	347	4.7E+08	1.8E+06
QGYSEFGDYSQFWR	Toxin_variant_1;Toxin_variant_2;Toxin_vari-	4850	4863	4.6E+08	
VQEVWDGWNAQAPSLGLPQIGK	Toxin_variant_1;Toxin_variant_2;Toxin_vari-	3296	3317	4.6E+08	
DADNILNYR	Toxin_variant_1;A0A3S6EXC9	6104	6112	4.5E+08	
VADTEAFITGIR	Toxin_variant_2;A0A3S6EWV9	6048	6059	4.4E+08	5.7E+07
GDVNIITGFSLPNGGVDAGGK	Toxin_variant_1;A0A3S6EXX9;Toxin_vari-	2201	2221	4.4E+08	
ERDATGLYYYGFR	Toxin_variant_1;Toxin_vari-	5830	5842	4.4E+08	
SVIAMTNISR	Toxin_variant_2;A0A3S6EWV9	5301	5310	4.3E+08	
MAIQQSNNNTQTR	Toxin_variant_1;A0A3S6EXC9	5709	5721	4.3E+08	
QSAQDRYDHFK	Toxin_variant_1;A0A3S6EXX9;Toxin_vari-	2643	2653	4.2E+08	4.1E+06
MNFKVPNYR	Toxin_variant_1;A0A3S6EXX9;Toxin_vari-	2563	2571	4.1E+08	
AISVPLENVANGIVR	Toxin_variant_1;A0A3S6EXX9;Toxin_vari-	1933	1947	3.8E+08	
TFQYENAPLPGRPLSVTEQVNGENAR	Toxin_variant_2;A0A3S6EWV9	5325	5350	3.7E+08	
SKNIIYGIWK	Toxin_variant_1;A0A3S6EXX9;Toxin_vari-	2158	2167	3.6E+08	1.4E+07
TEFFFQLESALNQGK	Toxin_variant_1;A0A3S6EXX9;Toxin_vari-	1839	1853	3.6E+08	
LTFVAEDNPSLGNLDK	Toxin_variant_1;A0A3S6EWV3;Toxin_vari-	960	975	3.6E+08	5.9E+08
HSAPATNNNYTLNITVSER	Toxin_variant_2;A0A3S6EWV9	5628	5646	3.4E+08	
AISVPLENVANGIVRPIMMDNR	Toxin_variant_1;A0A3S6EXX9;Toxin_vari-	1933	1954	3.4E+08	
WENDSEAGSDVAFIPSEHDAFWLNR	Toxin_variant_1;Toxin_variant_2;Toxin_vari-	4567	4591	3.4E+08	
NTFPGVELIEDK	Toxin_variant_2;A0A3S6EWV9	6007	6018	3.4E+08	3.9E+07
KKDTLTISSLK	Toxin_variant_1;A0A3S6EXC9	5895	5905	3.3E+08	1.5E+08
LNKEFIFLR	Toxin_variant_1;A0A3S6EWV3;Toxin_vari-	1544	1552	3.3E+08	7.0E+08
STLLTGK	Toxin_variant_1;Toxin_variant_2;Toxin_vari-	4869	4875	3.2E+08	
DTLTISSLK	Toxin_variant_1;A0A3S6EXC9	5897	5905	2.9E+08	9.4E+07
YTAAIGSSTFSQGVR	Toxin_variant_1;A0A3S6EXX9;Toxin_vari-	3050	3064	2.9E+08	
KLQPSAR	Toxin_variant_1;A0A3S6EXX9;Toxin_vari-	2422	2428	2.8E+08	2.8E+07
SHIETAYK	Toxin_variant_2;A0A3S6EWV9	5825	5832	2.8E+08	
LEALNDR	Toxin_variant_1;Toxin_variant_2;Toxin_vari-	4037	4043	2.7E+08	
ENVSSETMVSR	Toxin_variant_1;A0A3S6EWV3;Toxin_vari-	992	1002	2.7E+08	2.2E+08
MADNGTLWNALLQAR	Toxin_variant_1;Toxin_variant_2;Toxin_vari-	4996	5010	2.6E+08	
ITNDAEATR	Toxin_variant_1;Toxin_vari-	5540	5548	2.6E+08	
SIFDIAK	Toxin_variant_1;A0A3S6EWV3;Toxin_vari-	606	612	2.6E+08	3.9E+08
GETADDSESYR	Toxin_variant_2;A0A3S6EWV9	5698	5708	2.4E+08	2.2E+06
YDSDDQQQLR	Toxin_variant_1;Toxin_variant_2;Toxin_vari-	5058	5067	2.4E+08	
NECEGAAEETYQELNYEPSISADKLT-	Toxin_variant_1;A0A3S6EWX1;Toxin_vari-	27	57	2.4E+08	
QLVEAAGQQPECHLPFPMHLHWR	Toxin_variant_1;Toxin_variant_2;Toxin_vari-	4450	4472	2.3E+08	
DSLSFDAYQMIQSGDLYR	Toxin_variant_1;A0A3S6EXX9;Toxin_vari-	2601	2618	2.3E+08	
GYSLTQPSDPDAIAASDPIHYRK	Toxin_variant_1;A0A3S6EXX9;Toxin_vari-	2380	2402	2.2E+08	7.3E+06
SSGTDLHAVVEGR	Toxin_variant_2;A0A3S6EWV9	6064	6076	2.1E+08	
YTEETYSRPDVNFKEDGSQGN-	Toxin_variant_1;Toxin_variant_2;Toxin_vari-	3190	3217	2.1E+08	
EQLFDQPFILDGGSFTYLDAK	Toxin_variant_1;A0A3S6EWV3;Toxin_vari-	1223	1243	2.0E+08	
NIIYGIWKEDANNNR	Toxin_variant_1;A0A3S6EXX9;Toxin_vari-	2160	2174	1.9E+08	
DGFLNLPGSLGNK	Toxin_variant_2;A0A3S6EWV9	5994	6006	1.9E+08	
SLDLVLSWETQNSR	Toxin_variant_1;A0A3S6EXX9;Toxin_vari-	2281	2294	1.9E+08	
DPGYVWDNKNECEGAAEETYQEL-	Toxin_variant_1;A0A3S6EWX1;Toxin_vari-	18	50	1.8E+08	
VFVASVVDFFVR	Toxin_variant_1;Toxin_variant_2;Toxin_vari-	3408	3419	1.8E+08	
GNNFYALHAGTGTPSEN-	Toxin_variant_1;A0A3S6EXC9	6028	6057	1.6E+08	
NEDSIHEYLEFANIKK	Toxin_variant_1;A0A3S6EWV3;Toxin_vari-	1591	1606	1.6E+08	3.5E+07
IALNLEPGLSINQQEATDWEEFANR	Toxin_variant_1;A0A3S6EXX9;Toxin_vari-	1788	1812	1.5E+08	
PFLTMTYR	Toxin_variant_1;A0A3S6EWV3;Toxin_vari-	1003	1010	1.5E+08	1.8E+08
PGAIEALDSPASYLLDLYK	Toxin_variant_1;A0A3S6EWV3;Toxin_vari-	696	714	1.5E+08	
KEISIACSGVK	Toxin_variant_1;Toxin_variant_2;Toxin_vari-	3472	3482	1.5E+08	3.2E+08
LYANQQGNWAPAQDVTQAEN-	Toxin_variant_1;Toxin_variant_2;Toxin_vari-	4248	4278	1.4E+08	
DGQESDSETYR	Toxin_variant_1;A0A3S6EXC9	5688	5698	1.4E+08	
GETADDSESYRYDGSSQR	Toxin_variant_2;A0A3S6EWV9	5698	5715	1.4E+08	
LRDKFQIK	Toxin_variant_1;A0A3S6EXX9;Toxin_vari-	2232	2239	1.2E+08	2.3E+07
TYAAHAGVLNTLQPDPVYK	Toxin_variant_2;A0A3S6EWV9	5975	5993	1.2E+08	6.6E+06
IRDHLLANNNVLPK	Toxin_variant_2;A0A3S6EWV9	6077	6090	1.2E+08	
LYISWFEVAEEK	Toxin_variant_1;A0A3S6EXX9;Toxin_vari-	1955	1966	1.2E+08	
LFRVESEPDVWVAR	Toxin_variant_1;Toxin_variant_2;Toxin_vari-	4836	4849	1.1E+08	
EEGGNGVVTTYTYEAETQR	Toxin_variant_2;A0A3S6EWV9	5494	5512	1.1E+08	
GLGGLFIWSGDQDNGILTNAAHEG-	Toxin_variant_1;A0A3S6EWX1;Toxin_vari-	483	509	1.0E+08	
RTFADTPHLVR	Toxin_variant_1;A0A3S6EXX9;Toxin_vari-	2976	2986	1.0E+08	
TPPHSLTITTDR	Toxin_variant_1;Toxin_variant_2;Toxin_vari-	5046	5057	9.9E+07	
LYISWFEVAEEKETDSDGNIIVSGR	Toxin_variant_1;A0A3S6EXX9;Toxin_vari-	1955	1979	9.9E+07	
AEYKQLILYPVIINR	Toxin_variant_1;A0A3S6EXX9;Toxin_vari-	2096	2110	9.8E+07	
LPEYNQLFPEPWDNFCR	Toxin_variant_1;A0A3S6EWV3;Toxin_vari-	679	695	9.7E+07	
WYAGTHWETKPLK	Toxin_variant_1;A0A3S6EXC9	5967	5979	9.5E+07	
TEYDGKGQGIR	Toxin_variant_1;Toxin_variant_2;Toxin_vari-	5123	5133	8.8E+07	1.3E+06
GQFGMTELK	Toxin_variant_1;A0A3S6EXC9	6156	6164	8.5E+07	7.7E+07
WDKHYCVVIETQDAAQLVTQAR	Toxin_variant_1;Toxin_variant_2;Toxin_vari-	4880	4901	8.1E+07	
RTIHQGNTLFETLLVVK	Toxin_variant_1;A0A3S6EXC9	5732	5748	8.0E+07	
LNTLFAKELIGK	Toxin_variant_1;A0A3S6EXX9;Toxin_vari-	2266	2277	7.9E+07	
SVLVTAGTLTGCTMITGVK	Toxin_variant_1;A0A3S6EXC9	6009	6027	7.9E+07	
DPGYVWDNK	Toxin_variant_1;A0A3S6EWX1;Toxin_vari-	18	26	7.8E+07	
GFHSIHSTGEWTHFTPLNTLPT-	Toxin_variant_1;Toxin_variant_2;Toxin_vari-	4197	4224	7.6E+07	
NGPALGTMENGAPEFFDIVK	Toxin_variant_1;Toxin_variant_2;Toxin_vari-	3581	3600	7.0E+07	
ISNLKGISIASSADPAK	Toxin_variant_1;A0A3S6EWX1;Toxin_vari-	291	307	6.8E+07	
DGENYVLLIK	Toxin_variant_1;Toxin_variant_2;Toxin_vari-	3447	3456	6.5E+07	6.8E+06
YQADSSKSESLSVSESYR	Toxin_variant_1;A0A3S6EXX9;Toxin_vari-	2722	2739	6.3E+07	
CWPNMGHGR	Toxin_variant_1;Toxin_variant_2;Toxin_vari-	4304	4312	6.2E+07	
TTLKWDK	Toxin_variant_1;Toxin_variant_2;Toxin_vari-	4876	4882	6.2E+07	
ELSAEDRR	Toxin_variant_1;A0A3S6EXC9	5940	5947	6.0E+07	2.7E+07

VKPSLSQYHPDK	Toxin_variant_2;A0A3S6EWV9	6019	6030	5.8E+07	8.9E+06
GKTIPVDPDGAVLASINCGFTK	Toxin_variant_1;A0A3S6EWX1;Toxin_vari-	157	178	5.7E+07	
VAKADYLYSEATK	Toxin_variant_1;A0A3S6EWX1;Toxin_vari-	449	461	5.7E+07	
LREEGGNGVVTTYTYEAETQR	Toxin_variant_2;A0A3S6EWV9	5492	5512	5.6E+07	
YTEETYSRPDVNFK	Toxin_variant_1;Toxin_variant_2;Toxin_vari-	3190	3203	5.6E+07	3.3E+07
ALYLPGLELR	Toxin_variant_3;A0A2D0TC51	5732	5741	5.4E+07	
NAKNATITTSIPSEEALK	Toxin_variant_1;A0A3S6EWX1;Toxin_vari-	386	403	5.3E+07	
WKPESSLGYYR	Toxin_variant_2;A0A3S6EWV9	6037	6047	5.2E+07	1.6E+07
VTVFDNR	Toxin_variant_3;A0A2D0TC51	5214	5220	5.0E+07	
SVSVSLPMLVGPYEDVCAQLTQTSS-	Toxin_variant_1;A0A3S6EXX9;Toxin_vari-	2934	2963	4.9E+07	
GFLTQSADPR	Toxin_variant_3;A0A2D0TC51	5252	5261	4.8E+07	
VAYQGGVDEQPSLQAL-	Toxin_variant_1;Toxin_variant_2;Toxin_vari-	4780	4807	4.7E+07	
DFTNLRSTIK	Toxin_variant_1;A0A3S6EXX9;Toxin_vari-	1741	1750	4.7E+07	
LPSATVPFPTDSSAYTSYTR	Toxin_variant_3;A0A2D0TC51	5594	5613	4.6E+07	
RLIYSFGGLIGDKK	Toxin_variant_1;A0A3S6EWX1;Toxin_vari-	116	129	4.4E+07	
AADNIKGPTQLVEHSDASYDVIELT-	Toxin_variant_1;A0A3S6EWV3;Toxin_vari-	893	923	4.4E+07	
IINKEIR	Toxin_variant_1;A0A3S6EWX1;Toxin_vari-	88	94	4.4E+07	1.4E+07
IGNPTTADVKPTENIPSPIL-	Toxin_variant_1;Toxin_variant_2;Toxin_vari-	3166	3197	4.3E+07	
RLCHQVLGFHR	Toxin_variant_1;Toxin_variant_2;Toxin_vari-	4026	4036	4.2E+07	
DATGLYYYGYR	Toxin_variant_3;A0A2D0TC51	5841	5851	4.0E+07	
WLSADPAGSVDGLNLYR	Toxin_variant_3;A0A2D0TC51	5860	5876	3.9E+07	
TYTYDEASNLTQIR	Toxin_variant_3;A0A2D0TC51	5614	5627	3.9E+07	
GVPQYNEDDEFLSPSGEVMAIAL-	Toxin_variant_1;Toxin_variant_2;Toxin_vari-	3801	3832	3.8E+07	
GENGKDDLSLAVTR	Toxin_variant_2;A0A3S6EWV9	5311	5324	3.5E+07	
AIYQLNQIDGPHR	Toxin_variant_2;A0A3S6EWV9	5912	5924	3.4E+07	5.8E+06
TFQYENAPLPGR	Toxin_variant_2;A0A3S6EWV9	5325	5336	3.3E+07	
DRTEQVIVK	Toxin_variant_3;A0A2D0TC51	5473	5481	3.3E+07	
TLNLAGLCVR	Toxin_variant_3;A0A2D0TC51	5366	5375	3.3E+07	
SGYTTNITVSNR	Toxin_variant_3;A0A2D0TC51	5634	5645	3.3E+07	
AGASLEELQPEA-	Toxin_variant_1;A0A3S6EWV3;Toxin_vari-	1016	1047	3.2E+07	
KDTLTISSLK	Toxin_variant_1;A0A3S6EXC9	5896	5905	3.2E+07	
RQEITKTISLK	Toxin_variant_1;A0A3S6EXX9;Toxin_vari-	2881	2891	3.0E+07	
QDSSVKPNLSYFTALSGEVLR	Toxin_variant_1;A0A3S6EXC9	5271	5291	3.0E+07	
PIMMDNR	Toxin_variant_1;A0A3S6EXX9;Toxin_vari-	1948	1954	2.9E+07	
RLIYSFGGLIGDK	Toxin_variant_1;A0A3S6EWX1;Toxin_vari-	116	128	2.9E+07	
IEPEITVLSSASK	Toxin_variant_1;A0A3S6EWV3;Toxin_vari-	573	585	2.9E+07	
VVPENTYTYDSLYQLVSATGR	Toxin_variant_3;A0A2D0TC51	5562	5582	2.7E+07	
LVGDVNQDFPACYNCSGIISGLEN-	Toxin_variant_2;A0A3S6EWV9	6131	6159	2.7E+07	
AVLSSLTDDVDK	Toxin_variant_1;A0A3S6EXC9	5640	5651	2.6E+07	
GGQEQIIVKSLTYSAAGQK	Toxin_variant_1;A0A3S6EXC9	5466	5484	2.4E+07	
GFLAQSLDPR	Toxin_variant_2;A0A3S6EWV9	5252	5261	2.3E+07	
YSYDNLTGSSVLELDSDGK	Toxin_variant_3;A0A2D0TC51	5786	5804	2.2E+07	
LTLDYDLNNSVSTLVAVR	Toxin_variant_1;Toxin_variant_2;Toxin_vari-	4056	4073	2.1E+07	
AKGLLGGFR	Toxin_variant_1;A0A3S6EWX1;Toxin_vari-	193	201	2.1E+07	
VEAFFDAAGR	Toxin_variant_1;A0A3S6EXC9	5652	5661	2.0E+07	
ELIGKASR	Toxin_variant_1;A0A3S6EXX9;Toxin_vari-	2273	2280	1.9E+07	2.0E+06
TTGYENTVGVSFSLLTK	Toxin_variant_1;A0A3S6EXC9	6113	6129	1.9E+07	
ITPHQYDAR	Toxin_variant_3;A0A2D0TC51	5243	5251	1.8E+07	
IDAANIPALMDAGVTGINLMTYDFFT-	Toxin_variant_1;A0A3S6EWX1;Toxin_vari-	308	338	1.6E+07	
DELLFSAGYQLAPR	Toxin_variant_1;Toxin_variant_2;Toxin_vari-	4822	4835	1.5E+07	
YYRHPDTPQEIAER	Toxin_variant_1;A0A3S6EXC9	5232	5245	1.5E+07	
SFEVVSSLYR	Toxin_variant_1;A0A3S6EWV3;Toxin_vari-	1285	1294	1.5E+07	3.2E+09
VYVEQNSR	Toxin_variant_1;A0A3S6EXX9;Toxin_vari-	2873	2880	1.5E+07	
HPDAPEVTNER	Toxin_variant_3;A0A2D0TC51	5232	5242	1.4E+07	
MTESTGMILQETLNNEAVLK	Toxin_variant_2;A0A3S6EWV9	5933	5952	1.4E+07	
DPSDVYSKYSIDDAVTHLIDEK	Toxin_variant_1;A0A3S6EWX1;Toxin_vari-	348	369	1.3E+07	
PPYWNSRPLVDEPFK	Toxin_variant_1;A0A3S6EXX9;Toxin_vari-	2365	2379	1.2E+07	
LTKTEFFFQLESALNQGK	Toxin_variant_1;A0A3S6EXX9;Toxin_vari-	1836	1853	1.2E+07	
SIFDIAKVSR	Toxin_variant_1;A0A3S6EWV3;Toxin_vari-	606	615	1.1E+07	1.2E+07
AAGLLGGLRELQK	Toxin_variant_1;Toxin_variant_2;Toxin_vari-	3360	3372	1.1E+07	
LIFSFLGICGDIGNK	Toxin_variant_1;Toxin_variant_2;Toxin_vari-	3278	3292	1.1E+07	
MFPEIYVDPTLRLTK	Toxin_variant_1;A0A3S6EXX9;Toxin_vari-	1824	1838	1.1E+07	
AVLSSLTDDVDKVEAFFDAAGR	Toxin_variant_1;A0A3S6EXC9	5640	5661	1.1E+07	
NLNLAGQCVSYYDAA-	Toxin_variant_2;A0A3S6EWV9	5366	5399	9.5E+06	
DISINKIPTFEGGTTGWLAR	Toxin_variant_1;Toxin_variant_2;Toxin_vari-	3990	4009	9.4E+06	
SKNIIYGIWKEDANNNR	Toxin_variant_1;A0A3S6EXX9;Toxin_vari-	2158	2174	8.9E+06	
FEPMLNR	Toxin_variant_1;A0A3S6EXX9;Toxin_vari-	2572	2578	8.4E+06	
TDGVDAGTIFSLNDIAAR	Toxin_variant_1;A0A3S6EXC9	5292	5309	8.2E+06	
NGDTETESLQVITVGEASR	Toxin_variant_3;A0A2D0TC51	5745	5763	7.5E+06	
ETITVKLR	Toxin_variant_1;A0A3S6EWV3;Toxin_vari-	924	931	7.4E+06	
ITSLQYLPEGR	Toxin_variant_3;A0A2D0TC51	6132	6142	7.4E+06	3.6E+06
DDLSLAVTR	Toxin_variant_2;A0A3S6EWV9	5316	5324	6.8E+06	
DALVDYYLGQIVPNSK	Toxin_variant_1;A0A3S6EXX9;Toxin_vari-	1725	1740	6.5E+06	
AMKGQLLR	Toxin_variant_1;Toxin_variant_2;Toxin_vari-	4592	4599	6.1E+06	
LSLDNDALYKEVTAL-	Toxin_variant_1;A0A3S6EWV3;Toxin_vari-	740	766	5.7E+06	
PTENIPSPILVEDK	Toxin_variant_1;Toxin_variant_2;Toxin_vari-	3176	3189	5.5E+06	
AASLLGLNPPQATNVFEIDWIR	Toxin_variant_1;A0A3S6EWV3;Toxin_vari-	1638	1659	5.5E+06	
APANGFTLETLIASNSLIGSNQPFTYL-	Toxin_variant_1;Toxin_variant_2;Toxin_vari-	4749	4779	5.4E+06	
SNSPLVPQTSSSTDASSESQTNK	Toxin_variant_1;A0A3S6EWV3;Toxin_vari-	656	678	5.2E+06	4.8E+06
QKTPINFNLEEQIFVEDYQELYQR	Toxin_variant_1;A0A3S6EXX9;Toxin_vari-	2907	2930	5.1E+06	
TEQVIVK	Toxin_variant_3;A0A2D0TC51	5475	5481	5.1E+06	
QDRDKDFPPQNHK	Toxin_variant_1;A0A3S6EXC9	5927	5939	3.6E+06	
YLFNPFECEDEPALLLGK	Toxin_variant_1;A0A3S6EXX9;Toxin_vari-	2347	2364	3.5E+06	
GLSDLDDYGANLVWFYLHETANGGK	Toxin_variant_1;A0A3S6EXX9;Toxin_vari-	2071	2095	2.8E+06	
EIYLKSISEIK	Toxin_variant_1;Toxin_variant_2;Toxin_vari-	3703	3713	1.7E+06	
AVLGYLNNFEEVSNLEI-	Toxin_variant_1;A0A3S6EXX9;Toxin_vari-	1862	1892	1.3E+06	
EISIACSGVKAK	Toxin_variant_1;Toxin_variant_2;Toxin_vari-	3473	3484		2.2E+06
DLSRHGYIVK	Toxin_variant_1;A0A3S6EWV3;Toxin_vari-	883	892		3.0E+06
QPAFDDKQTQDK	Toxin_variant_1;A0A3S6EWV3;Toxin_vari-	1326	1337		3.8E+06
RADIPKLSLDNDALYK	Toxin_variant_1;A0A3S6EWV3;Toxin_vari-	734	749		4.4E+06
GQFGMTELKYEAR	Toxin_variant_1;A0A3S6EXC9	6156	6168		5.0E+06
TEAEKTLVDNSEK	Toxin_variant_1;A0A3S6EWV3;Toxin_vari-	1607	1619		6.8E+06
GRGFDLATLMQNPATYDR	Toxin_variant_1;Toxin_variant_2;Toxin_vari-	3260	3277		6.9E+06
EIQSLSNFRLER	Toxin_variant_1;A0A3S6EWV3;Toxin_vari-	1124	1135		1.3E+07
LDGGGSKEEER	Toxin_variant_1;Toxin_variant_2;Toxin_vari-	3249	3259		3.4E+07
SSISPLLAAAAK	Toxin_variant_1;A0A3S6EWV3;Toxin_vari-	561	572		4.3E+07
GENIITYQR	Toxin_variant_1;A0A3S6EWV3;Toxin_vari-	932	940		6.3E+08
AVFNFLTK	Toxin_variant_1;A0A3S6EXX9;Toxin_vari-	2403	2410		8.8E+08
EDGSQGNLSYTATR	Toxin_variant_1;Toxin_variant_2;Toxin_vari-	3204	3217		1.0E+09
AATADEINK	Toxin_variant_1;Toxin_variant_2;Toxin_vari-	3157	3165		1.1E+09
AQLADLVGAGLSDLVLIGPK	Toxin_variant_1;Toxin_variant_2;Toxin_vari-	4225	4244		

Table 4: Overview of test conditions for canonical pore state

Conditions	Prepore state	Canonical pore state	Lollipop pore state	Aggregates
3 M GdmCL (5min)	X			
3 M GdmCL (30min)	X		x	
3 M GdmCL (30min), 50 °			X	X
6 M GdmCL (30min)				X
Freeze/thaw (3 cycles)	X	x	x	
Standard pore formation protocol			X	
42 ° (30 min)	X			
50 ° (30 min)	X			X
20 mM CAPS pH 11.2, 250 mM NaCl (5 min)	X			
20 mM CAPS pH 11.2, 250 mM NaCl (30 min)	X		x	
20 mM CAPS pH 11.2, 250 mM NaCl (30 min), 42 ° (30 min)	X		x	
2% Tween-20 (5 min)	x	X	x	

10 Acknowledgement

First of all, I would like to thank my supervisor, Prof. Dr. Stefan Raunser, for providing an excellent scientific environment and allowing me to be part of it. His continuous support did not only enable me to grow scientifically but also on a personal level and I am very grateful for all the advice and knowledge he provided me with throughout the years!

Furthermore, I would like to thank Prof. Dr. Daniel Summerer for his willingness to be the second referee of my thesis. Moreover, for being part of my TAC committee and his valuable suggestions and the support throughout my studies. Many thanks also to Prof. Dr. Enrica Bordignon for her strong support as member of my TAC committee and her many inspirations.

"The most beautiful things in the world cannot be seen or touched, they are felt with the heart." – Antoine de Saint-Exupéry

I am extremely grateful for my colleagues in our institute and all the people I had the opportunity to meet throughout the years. Many thanks to the best office mates one can wish for! Peter, Wout, and Micaela did not only support me scientifically in any way possible and help me become a scientist but also helped me keep and improve my persistence and sanity. Thanks for the great time!

Additionally, I owe a big thank you to Philipp who did not only share the same, in parts exhausting but also exciting, path to PhD with me but kept me on track and always had an open ear for my problems and thoughts. Furthermore, I would like to thank all the current and past member of the toxin group for their constant support and brilliant exchange of ideas and concepts. Special thanks to Oleg, Patrick and Alex for their great supervision and assistance on the path to become a good scientist.

Furthermore, I am very grateful to our italo-American couple, Adriana and Gavin, for all the funny moments inside and outside the institute and the advice and support they have provided me with throughout the 'ages'.

Lastly, I am very grateful to the ‘girl’s office’ (Victorico, Sree, Elisa and Alicia) as well as all ‘associated members’ (Baptisto and Isabel) for the plethora of fun, food and drinks and the support (physical and mental) they have provided me with.

A big thank you to our EM facility dream team Oliver and Daniel for their excellent and immediate microscopy support at any possible time (day and night) and all the stories in between. Moreover, I am very grateful for the brilliant IT support throughout the years by Thorsten and Markus + Team. Additionally, I would also like to thank our technical assistants (Karin, Nathalie, Astrid, Marion, Sandra, Wei and Diana) for their spotless work in running the lab!

I would also like to express my tremendous gratitude to Lucia and Christa for their constant support throughout the whole of our IMPRS program and all the courses and skills they provided us with.

Last but not least, an infinite thanks to my family and friends without whom I would never have been able to get here – I will be forever grateful!

11 Table of Figures

12 Table of Figure Supplement

13 Table of tables

14 Eidesstattliche Versicherung

Eidesstattliche Versicherung (Affidavit)

Bader, Raphael
Name, Vorname
(Surname, first name)

232026
Matrikel-Nr.
(Enrolment number)

Belehrung:

Wer vorsätzlich gegen eine die Täuschung über Prüfungsleistungen betreffende Regelung einer Hochschulprüfungsordnung verstößt, handelt ordnungswidrig. Die Ordnungswidrigkeit kann mit einer Geldbuße von bis zu 50.000,00 € geahndet werden. Zuständige Verwaltungsbehörde für die Verfolgung und Ahndung von Ordnungswidrigkeiten ist der Kanzler/die Kanzlerin der Technischen Universität Dortmund. Im Falle eines mehrfachen oder sonstigen schwerwiegenden Täuschungsversuches kann der Prüfling zudem exmatrikuliert werden, § 63 Abs. 5 Hochschulgesetz NRW.

Die Abgabe einer falschen Versicherung an Eides statt ist strafbar.

Wer vorsätzlich eine falsche Versicherung an Eides statt abgibt, kann mit einer Freiheitsstrafe bis zu drei Jahren oder mit Geldstrafe bestraft werden, § 156 StGB. Die fahrlässige Abgabe einer falschen Versicherung an Eides statt kann mit einer Freiheitsstrafe bis zu einem Jahr oder Geldstrafe bestraft werden, § 161 StGB.

Die oben stehende Belehrung habe ich zur Kenntnis genommen:

Official notification:

Any person who intentionally breaches any regulation of university examination regulations relating to deception in examination performance is acting improperly. This offence can be punished with a fine of up to EUR 50,000.00. The competent administrative authority for the pursuit and prosecution of offences of this type is the chancellor of the TU Dortmund University. In the case of multiple or other serious attempts at deception, the candidate can also be unenrolled, Section 63, paragraph 5 of the Universities Act of North Rhine-Westphalia.

The submission of a false affidavit is punishable.

Any person who intentionally submits a false affidavit can be punished with a prison sentence of up to three years or a fine, Section 156 of the Criminal Code. The negligent submission of a false affidavit can be punished with a prison sentence of up to one year or a fine, Section 161 of the Criminal Code.

I have taken note of the above official notification.

Dortmund, 15.07.2025
Ort, Datum
(Place, date)

Unterschrift
(Signature)

Titel der Dissertation:
(Title of the thesis):

Structural Investigation of Tc toxin activation

Ich versichere hiermit an Eides statt, dass ich die vorliegende Dissertation mit dem Titel selbstständig und ohne unzulässige fremde Hilfe angefertigt habe. Ich habe keine anderen als die angegebenen Quellen und Hilfsmittel benutzt sowie wörtliche und sinngemäße Zitate kenntlich gemacht.
Die Arbeit hat in gegenwärtiger oder in einer anderen Fassung weder der TU Dortmund noch einer anderen Hochschule im Zusammenhang mit einer staatlichen oder akademischen Prüfung vorgelegen.

I hereby swear that I have completed the present dissertation independently and without inadmissible external support. I have not used any sources or tools other than those indicated and have identified literal and analogous quotations.

The thesis in its current version or another version has not been presented to the TU Dortmund University or another university in connection with a state or academic examination.*

*Please be aware that solely the German version of the affidavit ("Eidesstattliche Versicherung") for the PhD thesis is the official and legally binding version.

Dortmund, 15.07.2025
Ort, Datum
(Place, date)

Unterschrift
(Signature)